IMAGE RECONSTRUCTION USING PDE, VARIATIONAL AND REGULARIZATION METHODS

Thesis

Submitted in partial fulfillment of the requirements for the degree of
DOCTOR OF PHILOSOPHY

by

Jidesh P

DEPARTMENT OF MATHEMATICAL AND COMPUTATIONAL SCIENCES,
NATIONAL INSTITUTE OF TECHNOLOGY KARNATAKA,
SURATHKAL, MANGALORE -575025

JULY, 2013

DECLARATION

I hereby ***declare*** that the research Thesis entitled **IMAGE RECONSTRUCTION USING PDE, VARIATIONAL AND REGULARIZATION METHODS** which is being submitted to the ***National Institute of Technology Karnataka, Surathkal*** in partial fulfillment of the requirement for the award of the Degree of ***Doctor of Philosophy*** in **Department of Mathematical and Computational Sciences** is a ***bonafide report of the research work carried out by me***. The material contained in this research Thesis has not been submitted to any University or Institution for the award of any degree.

MA10P01, Jidesh P.
Department of Mathematical and Computational Sciences.

Place: NITK-Surathkal.
Date:

CERTIFICATE

This is to certify that the Research Thesis entitled **IMAGE RECONSTRUCTION USING PDE, VARIATIONAL AND REGULARIZATION METHODS** submitted by **Jidesh P** (Register Number: MA10P01) as the record of the research work carried out by him, is accepted as the *Research Thesis submission* in partial fulfillment of the requirements for the award of degree of **Doctor of Philosophy**.

Research Guide

Chairman-DRPC
(Signature with Date and Seal)

Acknowledgements

I wish to thank my colleague and research advisor Dr. Santhosh George, Professor, MACS Dept, for his guidance, motivation and wholehearted support. His constant support and motivation throughout the course of work paved the way to successfully carryout the research activity.

I sincerely express my gratitude to my thesis examiners Dr. P.K. Bora, Professor (Electronics & Electrical Engineering), IIT Guwahati and Dr. Mahmoud El-Sakka, Professor (Computer Science), University of Waterloo, Ontario, Canada, for their invaluable comments and suggestions on my research work.

It's my great pleasure to thank Dr. K.M Ajith and Prof. M.C. Narasimhan (the RPAC-members) for their invaluable suggestions.

I put into record my sincere gratitude to the HOD, MACS Department, for the full support during my Ph.D. work.

The help and support provided by my colleagues in the department demands a special appreciation. I feel paucity of words to express my gratitude to each and every one of them.

The research scholars and students were always helpful and extended their support whenever it was needed. It is a humble pleasure to express my gratefulness to all of them.

I wish to thank Dr. Philip (Max-Planck-Institut für Informatik, Saarbrücken) and Prof. Balasubramani (Mangalore University) for their suggestions and comments regarding my research work.

I express my sincere appreciation to all the unknown reviewers of Comp. Elec. Engg (Elsevier), Signal Image and Video Proc. (SIVP- Springer), J. Modern Optics (Taylor & Francis), Mutl. Dim. Sig. Syst (Springer), J. Chin. Inst. Eng. (JCIE- Taylor & Francis) and J. Sig. Imag. Syst. Eng. (Inderscience) for their valuable suggestion and constructive comments on my research papers.

Last not least I deeply appreciate the endurance and patience shown by my family members: son, wife, mother and father. Their support and encouragement helped me a lot during the course of my research work.

Jidesh P.

To my dear son and wife.

*"**Vision** is the art of seeing what is invisible to others"*
-J. Swift

Abstract

Image restoration and enhancement are two important requirements in the field of image processing. In this study three anisotropic non-linear diffusion filters are proposed for image restoration and enhancement and one filter for image inpainting. The orientation, type and extent of filtering are controlled by the decision mechanism based on the underlying image features. The first process is a conditionally anisotropic diffusion for deblurring and denoising images. This process is a time-dependent curvature based model and the steady state is attained at a faster rate, using the explicit time-marching scheme. The filter switches between isotropic and anisotropic behavior based on the local image features. Two other non-linear curvature based diffusion processes are devised, one for image enhancement and the other one for image inpainting. The diffusion process in these filters is driven by the Gauss curvature of the level curves of the image. Therefore, these methods are capable of preserving structures even with non-zero mean curvature values like curvy edges and corners. To be precise, the second process couples a hyperbolic shock filter together with a Gauss curvature driven diffusion term to enhance images. And the third one inpaints the intended domain based on the Gauss curvature. Finally, a fourth-order shock coupled diffusion filter is proposed for image enhancement. This is an anisotropic model that converges at a faster rate and preserves planar approximation while enhancing images. In this study a thorough theoretical and experimental analysis is carried out for each and every diffusion process introduced as a part of this thesis work. A variety of applications are presented for denoising and deblurring gray-level and color images. The required mathematical preliminaries are presented in the introduction of the thesis. We conclude the thesis highlighting some of the future enhancements that could be possibly taken forward for further research.

Keywords: Image Reconstruction; Image enhancement; Image inpainting; Variational methods; Regularization methods; PDE methods.

Contents

List of Figures

List of Tables

Nomenclature

SYMBOL	MEANING	SYMBOL	MEANING
λ	Scalar regularization Parameter	σ	Standard deviation
Ω	Image domain	Ω'	Inpainting Domain
$u(x, y)$	2-D discrete image	ϵ	Small positive value
$\|.\|$	Absolute value	$\|.\|$	Euclidean norm
L^2	L^2 functional space	Δt	Time step
∇^2	Laplacian operator	div	Divergence operator
min	Minimize the functional	∇	Gradient
u_t	$\partial u/\partial t$	u^n	Image at the n^{th} iteration
$\|.\|_{TV}$	Total Variation norm	$\|.\|_{\mathcal{L}^2}$	$\mathcal{L}^2$ norm
μ	Mean	σ^2	Variance
η	Perpendicular direction to the level-curve	ξ	Parallel direction to the level-curve
$\vec{n}$	Unit normal to the surface	$\mathbb{R}^2$	2-Dimensional real space
e^x	Exponential function	$\|\Omega\|$	Image area
Δ	A small change	h	Space step parameter
c	Coefficient of diffusion	G_σ	Gaussian convolved data with variance σ^2
κ	Contrast parameter	u_{xx}	Second derivative along x direction
u	Image function	$BV(\Omega)$	Space of bounced variation
$arctan$	Inverse tan trigonometric function	$\mathcal{K}$	Curvature of the level curve
max	Maximum value	ω	Frequency variable
$W^{1,2}(\Omega)$	Sobolev space	ϵ	Small positive value.
Δ_+	Forward difference operator	Δ_-	Backward difference operator

Abbreviations

Abbreviation	Expansion
PDE	Partial Differential Equations
MCM	Mean Curvature Motion
E-L	Euler-Lagrange
P-M	Perona Malik
TV	Total Variation
BV	Bounded Variation
MO	Marquina Osher
MCDD	Mean Curvature Driven Diffusion
GCDD	Gauss Curvature Driven Diffusion
CDD	Curvature driven Diffusion
NLM	Non-Local Means
SNR	Signal-to-Noise Ratio
PSNR	Peak SNR
CFL	Courant-Friedrichs-Lewy
RMSE	Root Mean Square Error
FFT	Fast Fourier Transform
DC	Direct current

Chapter 1

INTRODUCTION

Image processing is widely used for many applications in the areas of science and engineering in recent years. With the help of sophisticated methods, the area of image processing has created an ample impact on the society. Processing of images has become an inevitable step in many image processing applications including medical and satellite imaging.

Image denoising and enhancement/restoration are the two main image processing activities that are widely used for many applications. The need for efficient image restoration methods has grown with the massive production of digital images of all kinds, often taken in poor conditions. No matter how good cameras are, an image improvement is always desirable to extent their range of action. The deterioration of images are generally caused due to two different phenomena (Chan and Shen 2005). The first one is related to image acquisition and is mainly caused due to imaging system artifacts, the best example would be blurring. There are three major categories of blurs according to their physical background: optical, motion and atmospheric. Optical blur is also known by the name out-of-focus blur and is due to the inappropriate deviation of an imaging plane from the focus of an optical lens. Motion blur is due to rapid motions of either target objects or imaging devices during image capturing phase. Atmospheric blur is due to the scattering or optical turbulence of photonic media (due to the pressure variations in the atmosphere) through which light rays travel. The influence of the atmosphere on satellite imaging is a well known example, refer Bertero and Boccacci (1998) and Hansen et at. (2006) for further details on blurring. This phenomena is deterministic. The second one is due to the noise added to images/signals (generally during data transmission) and this is rather stochastic. The

knowledge regarding noise is limited to the probability distribution. Having said, that the noise is random, if one analyzes properly, it can be easily observed that the noise can also be data dependent. However, in most of the imaging modalities, noise can be modeled as random and independent of data. Further, in many practical scenarios, noise is observed to follow a Gaussian distribution with mean zero and variance σ^2 (Gaussian White Noise [1]).

Image denoising and restoration aim at recovering the original image from the degraded one. In many practical applications this problem is not well-posed in the sense of Hadamard (1953). Hence, the solution is not trivial. Many methods are suggested over the last few years for finding an appropriate solution (approximate solution) to this aforementioned image denoising and restoration problem. It ranges from spatial/frequency domain filtering techniques (like spatial averaging, Fourier domain filtering etc.), to most modern and sophisticated techniques like PDE/Variational methods. The recent solutions emerge in three different directions: PDE/variational /regularization, wavelets and stochastic approaches, we refer to Chan and Shen (2005) for details. This thesis focuses on the PDE, variational and regularization methods, for the image denoising and reconstruction, with the assumption that the device artifact is limited to an out-of-focus blur (linear and space invariant) and the noise is an additive data independent one. Furthermore, noise is assumed to be Gaussian distributed. The idea behind these methods is to represent an image as a $\mathbb{R}^2$ (2 dimensional real space) function defined on a domain of image Ω. This function usually satisfies a time dependent PDE that characterizes the problem under consideration. The solution of the differential equation gives the processed image at the scale t.

This chapter is organized in five sections. Section 1.1 discusses a general image degradation model and its mathematical formulation. Section 1.2 describes image denoising and enhancement using various PDE based methods. In the same section we introduce the mathematical preliminaries for variational and diffusion methods and their solutions. In Section 1.3 variational restoration methods are introduced. Section 1.4 highlights various quality measures used in this thesis to quantify the reconstruction performance of various filters under consideration. In Section 1.5, a brief outline of the contribution and the organization of this thesis is given.

[1] A stochastic signal $n(t)$ with mean zero is called a white noise if its power spectral density is a constant over all the spectra.

1.1 AN IMAGE DEGRADATION MODEL

An image restoration system can be abstractly formulated by an input output system:

$$u_0 = Ku + n. \tag{1.1}$$

The image u_0 denotes a degraded image acquired by the system, which could be degraded during acquisition, transmission or storage processes. Here u and u_0 belong to a Normed Linear Space (NLS). Here $K : \mathbb{R}^2 \to \mathbb{R}^2$ is a linear bounded operator (compact) defined on a two dimensional (2D) image real space. Throughout the thesis n denotes the noise (unless denoted otherwise), as already mentioned earlier the noise is assumed to be random and follows a Gaussian distribution with mean zero and variance σ^2. In most practical situations K is a blurring operator, which is typically a Fredholm first kind integral operator, and is assumed to be known a-priori. This operator is generally written as:

$$(Ku)(x, y) = \int_\Omega k(x, x', y, y')u(x', y')dx'dy', (x, y) \in \Omega, \tag{1.2}$$

where $k(x, x', y, y') = k(x-x', y-y')$ is the blurring kernel (shift invariance is assumed for the kernel k) and is defined as:

$$k(x, y) = \frac{1}{4\pi\sigma^2} e^{-(x^2+y^2)/2\sigma^2}, \tag{1.3}$$

where σ is the spread of the Gaussian kernel, $\Omega \subseteq \mathbb{R}^2$ is the area of support of the image and it is assumed to be compact. Note that we have used the notation $\int_\Omega(.)$ in place of $\int_x \int_y(.)$ and the notations $\mathrm{d}\Omega$ and $dxdy$ are used interchangeably throughout the thesis. Since shift invariance is imposed on k in (1.2), it becomes a Point Spread Function (PSF). Therefore, Ku can be written as $k * u$, where "*" is a linear convolution operation.

Analyzing the equation (1.1) one can arrive at three different problems.
Problem 1: $K = I$, where I is an identity operator, the problem becomes a denoising problem and takes the form:

$$u_0 = u + n. \tag{1.4}$$

Problem 2: $n = 0$ and $K \neq I$, the problem takes the form of a de-blurring problem

and can be modeled as:

$$u_0 = Ku. \tag{1.5}$$

Problem 3: $K \neq I$ and $n \neq 0$. In this case the problem is a deblurring and denoising problem.

Image reconstruction is an inverse problem, where one has to restore the actual image from the observed blurred and noisy one. One trivial way to solve this problem is to find the inverse of the operator K, but in many practical situations the matrix associated with the operator may be ill-conditioned (Having large condition number [2]). Therefore, the problem is ill-posed (see Definition 1) in nature. The ill-posed problems are generally handled using the regularization techniques. This chapter briefly discusses some of the PDE and variational regularization techniques to solve these problems and detailed explanations are provided in rest of the chapters of this thesis.

Definition 1. (Well-posedness/Ill-posedness) *When a minimization problem or a PDE admits a unique solution that depends continuously on the data, we say that the minimization problem or the PDE is well posed in the sense of Hadamard. If existence, uniqueness, or continuity fails, we say that the minimization problem or the PDE is ill posed (Hadamard 1953).*

1.2 IMAGE DENOISING AND ENHANCEMENT USING PDE

There has been a considerable interest in the field of Partial Differential Equations (PDE) based image reconstruction, in the last few decades (Aubert and Vese 1997, Kornprobst et al. 1997, Perona and Malik 1990, Weickert 1999, You and Kaveh 2000). The Majority of models proposed in the literature include a prior knowledge into the scale space evolution, which leads to an image enhancement, denoising, while preserving some of the semantically important information like edges, lines and finer details present in the images. These methods are widely used in the area of computer vision and image processing. A detailed survey of these methods can be found in Romeny and Bart (1994) and Weickert (1997). Spatial filters have been used for

[2] Condition number =maximum eigenvalue of the K/ minimum eigenvalue of K.

a long time as the traditional method for removing noise from images and signals. However, these filters tend to smooth data along with noise. In the last two decades, several improved PDE based techniques have been proposed for removing noise more effectively, while preserving the edges in the images. One of the main motivations for using PDEs is that, the theory behind the concept is well established. PDE methods have several advantages over the conventional image processing techniques. In PDE methods, substantial theoretical formulations are available with reference to well-posedness, such that stable and unique solution can be obtained. PDE based methods allow a re-interpretation of several classical methods under a novel unifying framework, more details can be found in Aubert and Kornprobst (2006). Furthermore, the PDE based approaches fall mainly into three categories: (i) diffusion based (ii) variational based (iii) contour-based. A brief introduction to these three methods are provided in this chapter and the details are presented in succeeding chapters.

1.2.1 Mathematical preliminaries

Well defined theories can be found in *calculus of variations*, to find a function that minimizes the functional. The basic minimization problem, then, is to determine a suitable function $y = u(x) \in C^1[a, b]$ that minimizes the objective *Lagrange* functional:

$$E(u) = \int_a^b f(x, u, u')dx. \tag{1.6}$$

For $u(x)$ to be the function that minimizes the energy functional in (1.6), it must satisfy the associated Euler-Lagrange(E-L) equation:

$$\partial f/\partial u - \frac{d}{dx}\left(\frac{\partial f}{\partial u'}\right) = 0, \tag{1.7}$$

subject to the selected boundary conditions. A detailed explanation and derivation of Euler-Lagrange equation is given in Appendix A-1. Any solution to the Euler-Lagrange equation subject to the assumed boundary conditions forms a critical point for the functional (cf. Gelfand and Fomin (1963) and Giaquinta and Hildebrandt (1996)) and hence is a potential candidate for the desired minimizing function. And, in many cases, the Euler-Lagrange equation suffices to characterize the minimizer without further ado.

Proposition 1. (E-L Equation) *A minimizer of the energy functional* (1.6) *necessarily satisfies the so-called Euler-Lagrange equation in* (1.7).
The uniqueness and existence of a minimizer for the functional is given in the following theorem and the corollary.

Definition 2. (Convex Functions) *f is a convex function if its domain is a convex set and if for any two points x and y in this domain, the graph of f lies below the straight line connecting $(x, f(x))$ to $(y, f(y))$ in the space $\mathbb{R}^{n+1}$. That is, we have: $f(\alpha x + (1-\alpha)y) \leq \alpha f(x) + (1-\alpha)f(y)$, for all $\alpha \in [0, 1]$.*

Theorem 1. *(Minimizer) When the functional f is convex (see Definition 2), any local minimizer x^* is a global minimizer of f. If in addition f is differentiable, then any stationary point x^* is a global minimizer.*

Proof. Let x_1^* and x_2^* be the local and global minima for f and let $x_1^* \neq x_2^*$. Since the functional is convex, then for any $\lambda \in (0, 1)$ we can write:

$$f(\lambda x_1^* + (1-\lambda)x_2^*) \leq \lambda f(x_1^*) + (1-\lambda)f(x_2^*)$$

(follows from the definition of convexity). Since $f(x_1^*)$ is a minimum of the functional we can write:

$$f(x_1^*) \leq f(\lambda x_1^* + (1-\lambda)x_2^*) \leq \lambda f(x_1^*) + (1-\lambda)f(x_2^*)$$

$$\implies f(x_1^*) \leq f(x_2^*).$$

Similarly we can show that:

$$f(x_2^*) \leq f(x_1^*). \tag{1.8}$$

From the two inequalities above, we have:

$$f(x_2^*) = f(x_1^*). \tag{1.9}$$

Assuming the differentiability and convexity for the functional f and applying Rolle's theorem, we have $x_2^* = x_1^*$. This contradicts our assumption that $x_2^* \neq x_1^*$. Therefore local and global minima are the same. The second part of the theorem follows from the differentiability and convexity of the functional. Hence the proof. □

Corollary 1. (Uniqueness) *If the flux function* [3] $\phi(.)$ *associated with the functional* $E(u) = \int_\Omega f(.)$ *is monotonically increasing then the functional is convex. In addition, if the functional is convex, then a unique minimum exists by Theorem 1 and the stationary point is described by the steady state solution of the associated Euler-Lagrange equation (note that the functional is assumed to be continuous and differentiable). The stationary point will be the global minimum of the functional.*

Proposition 2. ($\mathcal{L}^2$ stability) *If a classical solution* u *of higher order nonlinear diffusion with a non-negative diffusivity function* c *exists, which is continuously differentiable in the time variable* t *and* $2p$ *times continuously differentiable in the space variable, then the PDE is stable if* $\mathcal{L}^2$ *-norm of* $u(., t)$ *is monotonically decreasing with* $t \geq 0$. *Similarly the notion of stability (*l^2*- stability) can be defined for discrete schemes as well. Here* l^2 *denotes the space of all square summable* [4] *discrete sequences.*

In many classical solutions, the image is assumed to be a measurable function in the space of measurable functions defined in terms of Lebesgue measure(L^p space). A L^p image is defined below. Especially in some of the denoising models the image is assumed to be in L^2 space with normal Euclidean norm or $\mathcal{L}^2$ norm.

1.2.1.1 Ill-posedness and Regularization

In many image processing applications we come across inverse problems which are ill-posed in the sense of Hadamard, deblurring and denoising are good examples. Due to this ill-posed nature of the problem an inverse may not exist or if it exists, then it does not continuously depend on the data. In such scenarios the obtained solution is highly sensitive to perturbations. Hence the role of a regularization is well justified in such situations. In principle regularization imposes stability on an ill-posed problem in a manner that yields accurate approximate solutions, often by incorporating prior information, like smoothness of the function.

1.2.1.2 L^p Images

For any $p \in [0, \infty]$, the Lebesgue L^p function space is defined as:

$$L^p(\Omega) = \{u : \int_\Omega \|u(x)\|^p dx < \infty\}. \tag{1.10}$$

[3] Flux function is the gradient of the potential function $f(.)$ i.e. $\nabla f(.)$.

[4] $\sum_{i=0}^{i=N} (x_i)^2 < \infty$ for any discrete sequence (x_i).

And the images belong to Banach space under the norm (Adams and Fournier 2003, Chan and Shen 2005):

$$\|u\|_p = \left[\int_\Omega \|u\|^p dx\right]^{1/p}.$$

In many of the practical image processing and computer vision applications, it is assumed that the image belongs to a space of bounded variation (BV-Space). The property of BV-space allows discontinuities in the input image function, which comes in handy for many image processing applications, where images consist of many edges and finer details. These features contribute towards the discontinuities in the input image function. We define the concept of bounded variation images in the following section.

1.2.1.3 Bounded Variation Images

Let $\Omega \subseteq \mathbb{R}^2$ denotes a bounded open domain and $u = u(x, y) \in L^1(\Omega)$. In many image processing applications we assume Ω to be a Lipschitz domain. If u is smooth then Total Variation ($TV(u)$) is defined as $TV(u) = \int_\Omega \|\nabla u\| dxdy$, where $\nabla u = (u_x, u_y)$ (here u_x denotes $\frac{\partial u}{\partial x}$). A function u with $TV(u) < \infty$ is said to have a Bounded Variation (BV) (Ambrosio et al. 2000, Aubert and Kornprobst 2006, Chan and Shen 2005). The BV space is denoted as $BV(\Omega)$, which is all the functions in $L^1(\Omega)$ with BV. BV space is Banach under the natural norm $\|u\|_{BV} = \|u\|_{\mathcal{L}^1} + TV(u)$.

As evident from the details mentioned above, BV space allows discontinuities, thereby preserving the edges and finer details. However, the noise features contribute to high gradient oscillations (frequent discontinuities) in the input functions. So, while preserving the discontinuities the BV space ensures that the high oscillatory components are kept out by assuring the variations to be bounded.

1.2.1.4 Gradient descent method

Many methods are suggested in the last few decades to solve the minimization problem associated with the Euler-Lagrange equation, see Chan and Mulet (1999) and Chan and Chiu (1998) for details. One of the prominent methods widely used for solving these types of problems is the Gradient Descent method (Thomas 1995). To find the solution of a minimization problem, iterative algorithms can be used. These algorithms start with a given initial guess x^0 and generate a sequence of iterates $\{x^k\}_{k=0}^{\infty}$ that hopefully will converge to the solution x^*. Here it is assumed that the

initial guess is the observed degraded image and the solution is the final processed image. Which algorithm to use, depends on the problem, but all good algorithms should have the following properties:

- Robustness means that the solution is insensitive to the inputs in the algorithm. The algorithm must perform well on a wide variety of problems and for all choices of initial variables. Stability is also necessary. A stable algorithm gives nearly the right answer to nearly the right question.

- Efficiency is important, especially for large problems. If the algorithm requires too much computer time or storage, it may be impossible to solve the problem.

- One can confirm that an algorithm is accurate if the relative error between the mathematical problem $f(x)$ and the computed solution $g(x)$ is small. The relative error is defined as:
$$\frac{\|g(x) - f(x)\|}{\|f(x)\|}. \tag{1.11}$$

These goals may be at the expense of each others. An efficient algorithm not necessarily be the most accurate one. The method of steepest descent can be used for calculating a local maximum or minimum of a real-valued function $f(x)$. If $f(x)$ is continuous and differentiable in a neighborhood of a point x^0, $f(x)$ increases rapidly from the point x^0 in the direction of $\nabla f(x^0)$ and decreases rapidly in the direction of $-\nabla f(x^0)$. To find a minimum one can start at a point x^0 and take a small step in the direction of $-\nabla f(x^0)$ to a new point x^1. This can be done several times by the algorithm, that is:
$$x^{n+1} = x^n - \Delta t \nabla f(x^n), \quad n = 0, 1, 2, ..., \tag{1.12}$$
where $x^0 \in \mathbb{R}^2$ is an initial guess, $\Delta t > 0$ is the step size and $\nabla f(x) \in \mathbb{R}^2$ is the gradient of the function f at x. In case of convex functions, when Δt is small, the process converges to the desired solution. If Δt is small enough, x^n gets closer to the minimum as n increases. At a minimum x^*, the gradient $\nabla f(x^*)$ equals zero and the iterative algorithm has converged. If one follows the direction of the steepest descent from the initial guess x^0 in Figure 1.1, this will lead us much closer to the minimum. Gradient descents for various step sizes Δt are shown in Figure 1.2.

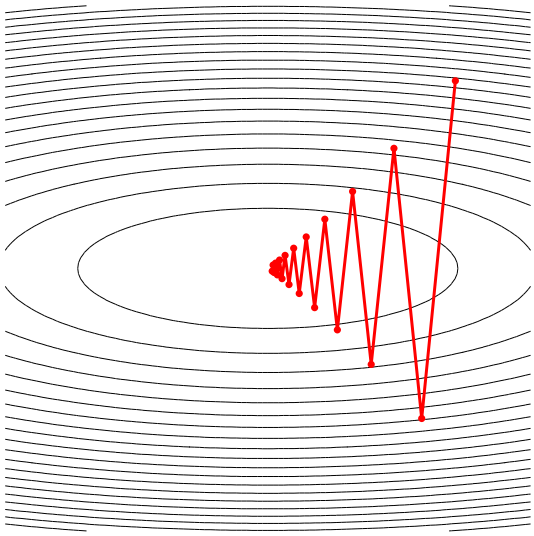

Figure 1.1: The gradient descent for a 2D function $f(x) = \frac{1}{2}\left(x_1^2 + \eta x_2^2\right)$, with $\eta = 10$ and $\Delta t = 0.18$, initial solution $x_0 = [0.5, 0.5]$.

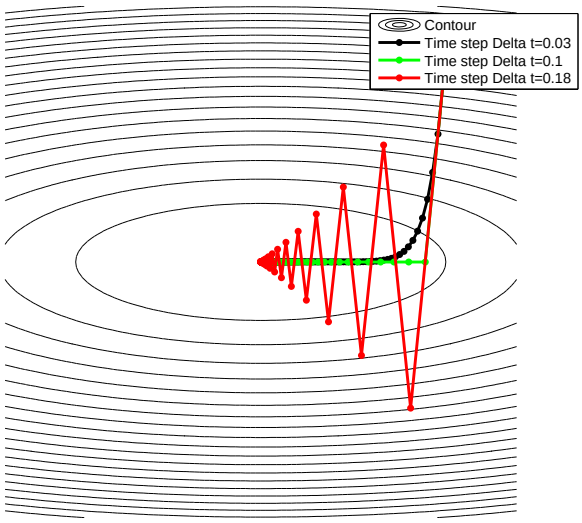

Figure 1.2: The gradient descent for a 2D function $f(x) = \frac{1}{2}\left(x_1^2 + \eta x_2^2\right)$, with $\eta = 10$ and different step size $\Delta t = 0.03$, $\Delta t = 0.1$ and $\Delta t = 0.18$, respectively. Initial solution $x_0 = [0.5, 0.5]$.

1.2.1.5 Finite Difference Methods

There are many approaches that are used for discretizing a partial differential equation. Among the most important ones, one can mention finite differences, finite elements, and spectral methods, refer Thomas (1995) for details. Finite difference methods are widely adopted in image processing, hence we restrict our discussion to finite difference

method, which is used throughout this thesis for discretizing the PDEs. The reason for adopting this method is well explained by the structure of digital images, which are a set of uniformly distributed pixels. Here a well-posed parabolic PDE (linear heat equation) is considered for explaining the concept, we refer to Aubert and Kornprobst (2006) for further details. The same scheme is adopted for all the parabolic PDEs (non-linear) discussed in this thesis. For hyperbolic PDEs we have adopted the *upwind scheme* proposed by Osher and Sethian. A brief explanation of the *upwind scheme* can be found in the next section and refer to Osher and Sethian (1988) for the details. Let us consider a parabolic 1D heat equation (the same idea can be extended in 2D cases as well):

$$\partial u/\partial t = \nu \frac{\partial^2 u}{\partial x^2}, \tag{1.13}$$

where $\nu > 0$ is a constant, with the initial condition $u(x, 0) = u_0$. Let u be the exact solution and v be an approximate one. One can write (1.13) in the form:

$$\partial u/\partial t - \nu \frac{\partial^2 u}{\partial x^2} = 0. \tag{1.14}$$

Remark 1. *One can realize that the discretized equation replaces the original equation by a new one, and that an exact solution of the discretized problem will lead to an approximate solution of the original PDE. An obvious error will be introduced due to the approximation.*

To solve PDE in (1.14) numerically, the spatial domain needs to be discretized using the grid points over the domain. Uniformly separated grids are used with the spacing Δx and Δt over the spatial and temporal domains, respectively. The solution is, to find a discrete function v at the point $(n\Delta t, i\Delta x)$ which is an approximation of (1.14).

With the help of Taylor's series expansion one can write the discretization of (1.14):

$$\frac{\partial u(n\Delta t, i\Delta x)}{\partial t} - \nu \frac{\partial^2 u(n\Delta t, i\Delta x)}{\partial x^2} = \frac{u_i^{n+1} - u_i^n}{\Delta t} - \nu \frac{u_{i+1}^n - 2u_i^n + u_{i-1}^n}{\Delta x^2} + O(\Delta t) + O(\Delta x^2). \tag{1.15}$$

Here $O(.)$ denotes the order[5]. Therefore, a considerable approximation to (1.15) is written as:

$$\frac{v_i^{n+1} - v_n^n}{\Delta t} - \nu \frac{v_{i+1}^n - 2v_i^n + v_{i-1}^n}{\Delta x^2} = 0, \tag{1.16}$$

where v is an approximation to u. The expression in (1.16) can also be written as:

$$v_i^{n+1} = (1 - 2r)v_i^n + r\left(v_{i+1}^n + v_{i-1}^n\right), \tag{1.17}$$

where $r = v\Delta t/\Delta x^2$. The scheme described in (1.17) is the explicit Euler scheme.[6] This scheme provides an approximate solution to the parabolic PDE described in (1.13), we refer to Aubert and Kornprobst (2006) for the details. The explicit scheme is used throughout the thesis, there are implicit and semi implicit schemes that can be used as well in image processing, see Thomas (1995).

Definition 3. (Notion of Convergence) *The scheme* (1.16) *approximating the PDE in* (1.13) *is convergent scheme at time t, if* $(n+1)\Delta t \to t$ *then,* $\|u^{n+1} - v^{n+1}\|_* \to 0$, *as* $\Delta t \to 0$ *and* $\Delta x \to 0$. *Here '*' denotes the corresponding norm.*
The discrete explicit schemes are l^2-stable [7], similar to $\mathcal{L}^2$-stability for continuous functionals in Proposition 2.

For handling the hyperbolic equations we use the upwind scheme proposed by Osher and Sethian (1988). Upwind schemes use an adaptive or solution-sensitive finite difference scheme to numerically simulate more properly, the direction of propagation of information in a flow field. The upwind schemes attempt to discretize hyperbolic partial differential equations by using differencing based on the direction determined by the sign of the characteristic speeds. Consider a hyperbolic wave equation of the form:

$$\partial u/\partial t = -a\partial u/\partial x. \tag{1.18}$$

It describes a wave propagating in the x-direction with a velocity a. The preceding equation is also a mathematical model for one-dimensional linear advection. Consider a typical grid point i in the domain. In a one-dimensional domain, there are only two directions associated with point i - left and right. If a is positive the left side is called *upwind* side and right side is the *downwind* side. Similarly, if a is negative the left

[5]Note that $g(s) = O(\phi(s))$ for some $s \in S$, if there exists a constant such that $\|g(s)\| \leq C\|\phi(s)\|$ for all $s \in S$. We say that $g(s)$ is of order $\phi(s)$ (Aubert and Kornprobst 2006).

[6]The values at time $(n+1)\Delta t$ are obtained only from the values at time $n\Delta t$.

[7]In case of discrete sequences.

side is called *downwind* side and right side is the *upwind* side. The first order upwind scheme is given by:

$$\begin{array}{ll} \frac{u_i^{n+1}-u_i^n}{\Delta t} + a(u_i^n - u_i^{n-1}) = 0 & \text{if } a > 0 \\ \frac{u_i^{n+1}-u_i^n}{\Delta t} + a(u_{i+1}^n - u_i^n) = 0 & \text{if } a < 0. \end{array} \tag{1.19}$$

Let

$$a^+ = max(a, 0), \quad a^- = min(a, 0)$$

and

$$u_x^+ = \frac{u_{i+1}^n - u_i^n}{\Delta x}, \quad u_x^- = \frac{u_i^n - u_{i-1}^n}{\Delta x},$$

then the explicit Euler equation can be written as:

$$u_i^{n+1} = u_i^n - \Delta t \left(a^+ u_x^- + a^- u_x^+\right). \tag{1.20}$$

The upwind scheme in (1.20) is stable if it satisfies the Courant-Friedrichs-Lewy (CFL) condition (which relates the time step Δt with the space step Δx) [8]:

$$\mathcal{C} = \left|\frac{a\Delta t}{\Delta x}\right| \leq 1. \tag{1.21}$$

1.2.2 Diffusion methods

Linear diffusion or heat equation is a trivial and widely used diffusion method in the literature, see Witkin (1983) and Iijima (1962). The PDE associated with the heat equation is parabolic. A linear heat equation is formulated as:

$$\frac{\partial u}{\partial t} = div(c.\nabla u). \tag{1.22}$$

Here c denotes the coefficient of diffusion and div is the divergence operator. The equation (1.22) is a parabolic equation and taking $c = 1$ will result in a linear heat equation:

$$\frac{\partial u}{\partial t} = \nabla^2 u = u_{xx} + u_{yy}\ , t \geq 0, \ \ (x, y) \in R^2, \tag{1.23}$$

[8] The time step Δt for all the PDEs defined in this thesis are evaluated based on this condition.

with the initial condition $u(x, y, 0) = u_0(x, y)$. Here u_{xx} and u_{yy} denotes the second-order derivatives along the directions x and y, respectively. Furthermore, one can see that $u_{xx} + u_{yy} = u_{\eta\eta} + u_{\xi\xi}$ (therefore, throughout the thesis these two notations are used interchangeably), where η and ξ are the directions along and across the gradient directions. The fundamental solution to heat equation is given by:

$$u(x, y, t) = (G_{\sqrt{2t}} * u_0)(x, y), \tag{1.24}$$

where $G_\sigma(x, y)$ denotes the two-dimensional Gaussian kernel:

$$G_\sigma(x, y) = \frac{1}{2\pi\sigma^2} \exp \frac{-|x^2 + y^2|}{2\sigma^2}. \tag{1.25}$$

The formula (1.24) gives the correspondence between the time t and the scale parameter σ of the Gaussian kernel. Hence, the explicit solution for heat equation is equivalent to a convolution of the data (image) with a Gaussian kernel. The convolution by a Gaussian is equivalent to a low-pass filtering, that inhibits high frequencies (oscillations in the space domain). Thus, it effectively removes noise, at the same time it also causes blurring of edges. Moreover, this solution is well defined in L^2 space with $\mathcal{L}^2$ norm. The L^2 space (with $\mathcal{L}^2$ norm) does not allow discontinuities in the solution. Therefore, the sharp edges and textures are highly affected by the diffusion flow. Figure 1.4 C shows the result of filtered output using the linear diffusion method. The image is denoised by penalizing the edges.

The aforementioned defect of linear diffusion was a serious concern for the image processing community for many years, till the introduction of a non-linear diffusion method. Since then, many non-linear diffusion methods of different orders were introduced by various researchers (Perona and Malik 1990, Rudin et al. 1992, Weickert 1999, You and Kaveh 2000, Lysaker et al. 2003). For a spatial 1-Dimensional filtering in the interval $(a, b) \subset \mathbb{R}^2$, any general nonlinear diffusion of order $2p$ is governed by the PDE:

$$\partial u/\partial t = (-1)^{p+1} \partial_x^p \left(c(\partial_x^p u) \partial_x^p u \right), \tag{1.26}$$

with the corresponding boundary conditions given as:

$$\partial_x^k \left(c(\partial_x^p u) \partial_x^p u \right)(x) = 0, \tag{1.27}$$

for $k \in 0, ..., p-1$ and $x \in \{a, b\}$. There are p constraints at each boundary pixel

as a generalization of homogeneous boundary condition. Here we remark that $\partial_x^p u$ denotes $\frac{\partial^p u}{\partial x^p}$.

Setting $p = 1$ in a 2-Dimensional scenario one can obtain the classical Perona-Malik filter (Perona and Malik 1990), read as:

$$\partial u/\partial t = div\left(c(\|\nabla u\|^2)\nabla u\right), \tag{1.28}$$

where

$$c = \frac{1}{1 + \|\nabla u\|^2/\kappa^2}. \tag{1.29}$$

(Here κ is a contrast parameter, which determines the nature of diffusion), with the homogeneous boundary condition:

$$\frac{\partial u}{\partial \vec{n}} = 0, \tag{1.30}$$

where $\vec{n}$ is the unit outward normal, and the initial condition:

$$u(x, y, 0) = u_0(x, y), \tag{1.31}$$

where u_0 is the initial image. Here $\|.\|$ denotes the absolute value of the function or the Euclidean norm. Throughout this thesis the boundary condition in (1.30) and the initial condition in (1.31) are assumed for all the PDEs, unless stated otherwise. The filter in (1.28) is a second-order non-linear filter which diffuses in the image regions with varying magnitudes. Here the diffusion coefficient c (as defined in (1.29)) is a function of the absolute gradient. Therefore, the diffusion happens at a higher rate in those regions where the gradient magnitude is low (homogeneous regions) and the extent of diffusion is negligible in the high gradient regions (or on the edges and finer details). This way, the non-linear diffusion preserves the edges and finer details while removing the noise features.

1.2.2.1 Properties of non-linear second-order diffusion

Denoising

The Perona-Malik filter (discussed above) applies an inhomogeneous diffusion that reduces the diffusivity at those locations which have a greater likelihood of being edges. However, the diffusion flux $j = -c(\|\nabla u\|)\nabla u$ is always parallel to the gradi-

ent direction since the diffusivity $c(\|\nabla u\|)$ is a scalar. Therefore, the Perona-Malik filter is not purely anisotropic[9] as the title of the paper suggests (Perona and Malik 1990). The second-order curvature-based methods like Total Variation (TV) denoising (Rudin et al. 1992) and Mean Curvature based method (Marquiana and Osher 2000) were introduced in the literature to address this issue. These curvature-based methods are anisotropic, so they diffuse along and across the edges, at varying magnitudes. The diffusion magnitude along the edges is much more compared to the magnitude across them (this can even be zero).

Enhancement

The energy functional associated with Perona-Malik filter in (1.28) is:

$$E(u) = \int_{\Omega} f(\|\nabla u\|)dxdy = \int_{\Omega} \frac{\kappa^2}{2} ln(k^2 + \|\nabla u\|^2)dxdy. \tag{1.32}$$

The flux function $\phi(\nabla u)$ is taken as the gradient of the potential function $f(u)$ in (1.32), ie.:

$$\phi(\nabla u) = \nabla(f(\|\nabla u\|)). \tag{1.33}$$

Let $s = \nabla u$, then $\phi(s) = \nabla f(\|s\|)$, $\nabla f(\|s\|) = c(\|s\|)s$, where $c(\|s\|) = \frac{1}{1+\|s\|^2/\kappa^2}$. The gradient descent solution for (1.32) can be written as:

$$u_t = div(c(\|\nabla u\|)\nabla u), \tag{1.34}$$

where $u_t = \frac{\partial u}{\partial t}$. For understanding easily, let us write the above equation in one-dimensional case. $u_t = \partial_x(\phi(\partial_x u)) = \phi'(\partial_x u)\partial_{xx} u$ (we remark that $\partial_x u = \partial u/\partial x$ and $\partial_{xx} u = \partial^2 u/\partial x^2$ are the first and second partial derivatives of u along x). Note that $\phi'(s)$ (the first derivative of ϕ) satisfies: $\phi'(s) \geq 0$ for $s \leq \kappa$ and $\phi'(s) < 0$ for $s > \kappa$. Hence, one can observe that this model is forward parabolic when $s \leq \kappa$ and inverse parabolic otherwise. When it is forward parabolic, the flux function $\phi(\|\nabla u\|)$ is monotonically increasing (see Figure 1.3), hence the associated energy functional in (1.32) is convex (see Appendix A-4 for detailed derivation and the proof), therefore, it has a unique minimum, so that, the gradient descent procedure can find it. On the other hand when $s \geq \kappa$ the flux function becomes non-monotonic (happens when the PDE is inverse parabolic) and the associated functional becomes non-convex and the solution becomes non-unique. When the flux function is monotonically increasing,

[9]In anisotropic diffusion the magnitude of diffusion depends on the direction of the gradient field.

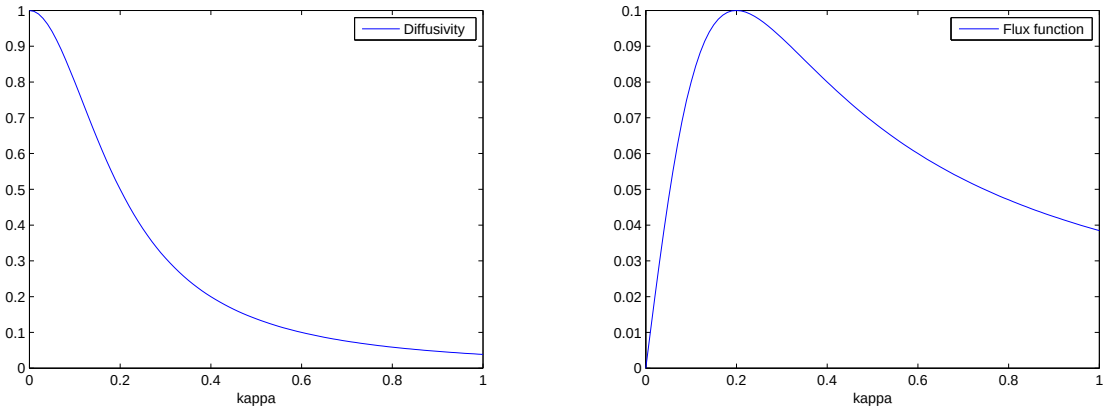

A B

Figure 1.3: (A) The diffusivity function $c(s^2)$; (B) the flux function $\phi(s)$.

then the diffusion cannot cause an enhancement to the edges, in other words, inverse diffusion will never take place. The inverse diffusion will result in enhancement or sharpening of the image features, see Figure 1.5. Therefore, there is a built-in shock[10] in the filter given in (1.28), which will enhance the edges in a non-linear way. Note that this shock is due to the negative diffusion under the conditions explained above. In general, for non-monotone flux function $\phi(\nabla u)$, there is no mathematical theory that guarantees for well-posedness. It is further shown in Hollig (1983) that, some of the diffusion processes with non-monotone flux functions, can have infinite number of solutions because the associated functional will become non-convex. There are many improved filters suggested by researchers to address this issue, see Weickert (1997), Catte et al. (1992) and Alvarez et al. (1992) for details. Figure 1.4 D shows the result of non-linear Perona-Malik filtering process. The image is denoised while preserving the edge features.

Piece-wise linear approximation

All the non-linear second-order diffusion filters are capable of denoising the images, while preserving the details. However, the second-order non-linear diffusion methods are devised in such a way that they diffuse in the homogeneous regions at a faster rate as compared to the non-homogeneous ones. All the second-order non-linear diffusion methods approximate the observed image with piece-wise linear images. The PDE evolution eventually results in forming piece-wise patches during the early stages of evolution and finally these patches combine to form a piece-wise image. This piece-

[10]Shock enhances the image edges and finer details.

wise image is the only minimum of the energy functional in (1.32), associated with the second-order PDE. Similarly during the inverse diffusion, any piece-wise constant image is a global minimum of the energy functional in (1.32), therefore, the blocks will appear in the early stages of evolution and they remain without any change during the course of evolution. The above mentioned discrepancy causes a visually unpleasant output image and this discrepancy is widely known by the name *staircase* effect. Figures 1.5 and 1.4 show the output of filtered images using second-order methods, the *staircase* effect is evident from the result. A sample Matlab code for implementing the second-order non-linear diffusion filter (Perona-Malik), using explicit finite central difference method with gradient descent procedure is provided in Appendix A-2. Similar coding scheme is followed for the parabolic non-linear PDEs discussed in this thesis. Therefore, for the brevity we don't provide the implementation for all the methods discussed in the thesis.

From the properties of the second-order filter defined above, it is evident that the filter approximates homogeneous regions with piece-wise constant functions, which eventually leads to the formation of piece-wise smooth patches. These patches causes visual discrepancy as mentioned already. Furthermore, the enhancement property of the second-order parabolic filter is governed by the unstable diffusion process causing the solution to be non-unique. The *staircase* effect is addressed by reformulating the diffusion to be of higher order (generally fourth-order PDEs serves the purpose very well). We describe a brief history of the fourth-order filter in the next section and a detailed description is provided in Chapter 5 of this thesis. The theoretical instability of the second-order non-linear parabolic PDE (during the negative diffusion) is handled effectively using stable hyperbolic PDEs. Therefore, these hyperbolic filters are extensively used for image enhancement. A detailed analysis on various stable non-linear second-order restoration filters is done in Chapter 3 of this thesis.

1.2.3 Higher-order diffusion methods

When $p = 2$ in (1.26), we obtain a fourth-order diffusion filter. The fourth-order diffusion filters are employed recently for image denoising, we refer to You and Kaveh (2000), Lysaker et al. (2003) and Chan et al. (2010) for details. One of the main motivations for using fourth-order filter is, fourth-order diffusion damps oscillations faster as compared to the second-order ones. Therefore they denoise the images rapidly. Moreover, fourth-order diffusion approximates observed images with piece-wise planar

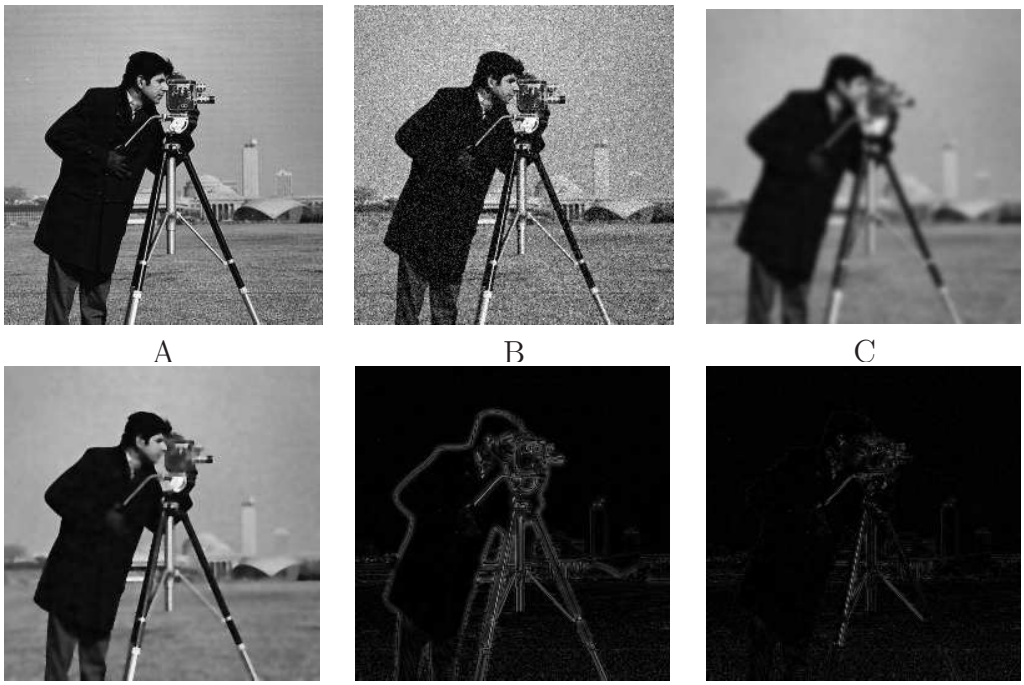

Figure 1.4: Results of linear and non-linear diffusion: (A) Original Image; (B) Noisy Image; (C) Filtered by linear heat equation; (D) Result of non-linear diffusion equation (Perona-Malik); (E) The residual image for linear diffusion; (F) The residual image for Perona-Malik filter.

images providing a better natural appearance to the processed image. The fourth-order diffusion method proposed by You and Kaveh (You and Kaveh 2000) considers the energy functional:

$$E = \int_{\Omega} f(\nabla^2 u) dx dy, \tag{1.35}$$

where $f(.)$ is an increasing function of Laplacian of the image ($\nabla^2 u$). The functional is convex and hence a unique minimum exists due to Theorem 1 and Corollary 1, (see Appendix A-3 for details and proof). Minimizing the energy functional is equivalent to smoothing the image. Deriving the PDE for the functional in (1.35) using the Euler Lagrange equation results in the evolution PDE stated as:

$$\frac{\partial u}{\partial t} = -\nabla^2 \left(c \left(\|\nabla^2 u\| \right) \nabla^2 u \right), \tag{1.36}$$

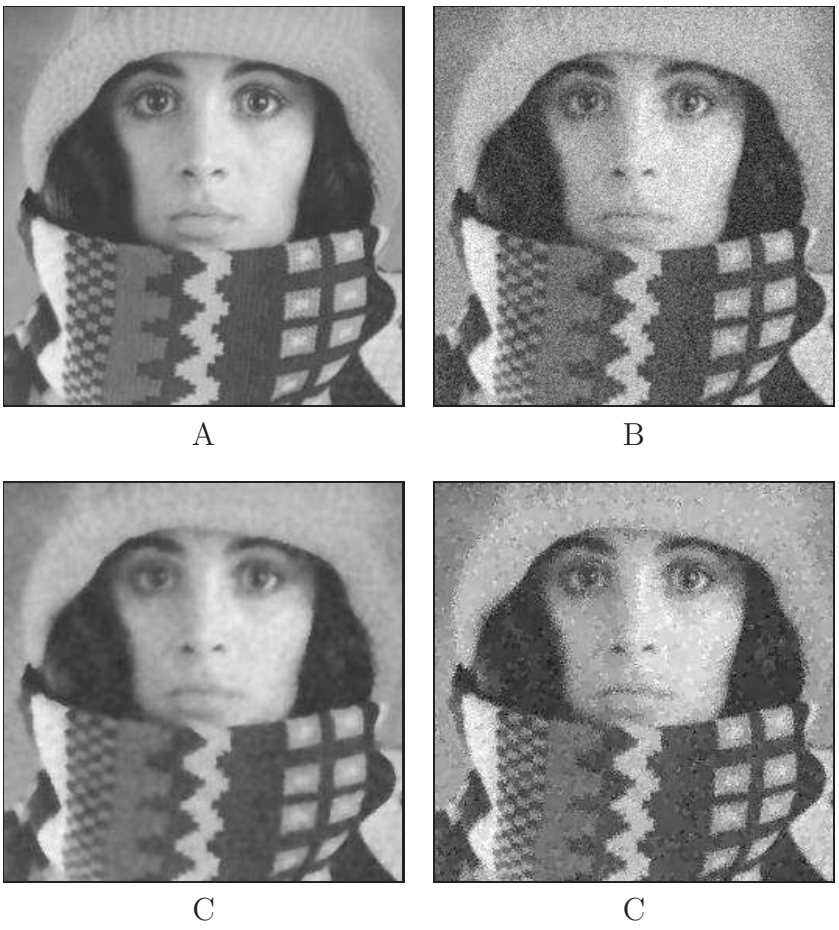

Figure 1.5: Results of non-linear forward and backward diffusions: (A) Original Image; (B) Noisy Image; (C) Filtered by Perona-Malik forward diffusion; (D) Filtered by Perona-Malik backward diffusion.

where $\|.\|$ is the Euclidean norm. The diffusion coefficient $c(.)$ is a non-increasing function of the absolute *Laplacian* of the image function defined as:

$$c(\|\nabla^2 u\|) = \frac{1}{1 + \left(\frac{\|\nabla^2 u\|}{\kappa}\right)^2}, \tag{1.37}$$

here κ is the contrast parameter.

Another model in this flavor was proposed by Lysaker et al. (2003). This model is formulated as a regularization model with specific boundary conditions. Taking $p = 2$ in (1.26) and total variation (TV) diffusivity as considered in Lysaker et al. (2003),

the evolution PDE can be formulated as:

$$u_t = -\left(\frac{u_{xx}}{|u_{xx}|}\right)_{xx} - \left(\frac{u_{yy}}{|u_{yy}|}\right)_{yy} - \lambda(u - u_0), \tag{1.38}$$

with the boundary condition:

$$\left(\frac{u_{xx}}{|u_{xx}|}\right) v_1 + \left(\frac{u_{xx}}{|u_{xx}|}\right) v_2 = 0 \tag{1.39}$$

and

$$\left(\frac{u_{xx}}{|u_{xx}|}\right)_x v_1 + \left(\frac{u_{xx}}{|u_{xx}|}\right)_y v_2 = 0 \;\; on \; \partial\Omega, \tag{1.40}$$

where $v = (v_1, v_2)$ is vector normal to $\partial\Omega$ and the regularization parameter λ is updated as:

$$\lambda = \frac{1}{\sigma^2} \int_\Omega \left(\frac{u_{xx}}{|u_{xx}|}(u - u_0)_{xx} - \frac{u_{yy}}{|u_{yy}|}(u - u_0)_{yy} \right) d\Omega. \tag{1.41}$$

1.2.3.1 Properties of fourth-order diffusion filters

Planar Approximation

All the fourth-order models approximate the observed images with piece-wise planar images. These filters try to minimize the Laplacian of the pixel at its neighborhood. The Laplacian of the pixel is zero in its planar neighborhood. The planar approximation helps in preserving the natural appearance of the image by reducing the *staircase-effect* unlike the second-order counterparts.

Isotropic property

The filter proposed in You and Kaveh (2000) is isotropic. When Laplacian is used as an edge descriptor as done in (1.36) and (1.38), results in an equi-magnitude diffusion in all directions. This property is not so desirable for images with considerable amount of edges and finer details. The planar approximation reduces the *staircase-effect* as evident from the Figure 1.6 and the enlarged portions of the second-order and fourth-order diffusion results in Figure 1.7. The isotropic nature of the filter is also quite noticeable in the filtered output images in Figure 1.6. Due to isotropic property of the PDE, the filtered output is apparently smooth or blurred. Many methods have been proposed in the recent literature to address these shortcomings of the fourth-order filter. The details are discussed in Chapter 5.

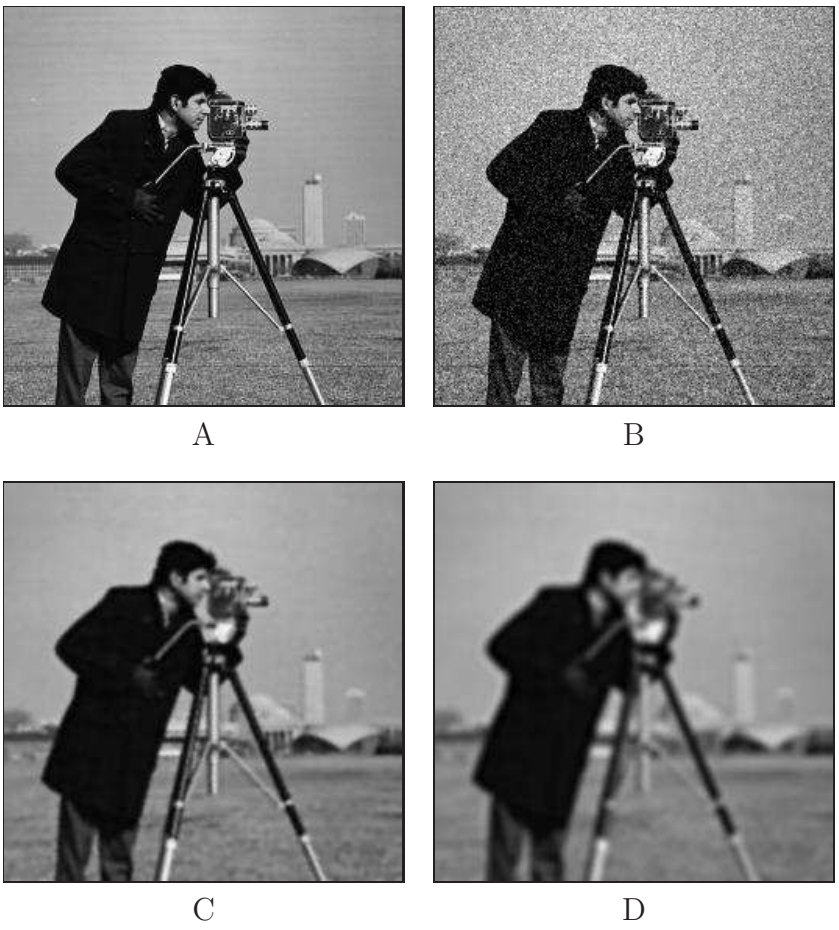

A B C D

Figure 1.6: Results of fourth-order diffusion filters: (A) Original Image; (B) Noisy input image; (C) Result of You-Kaveh method; (D) Result of Tai's Method.

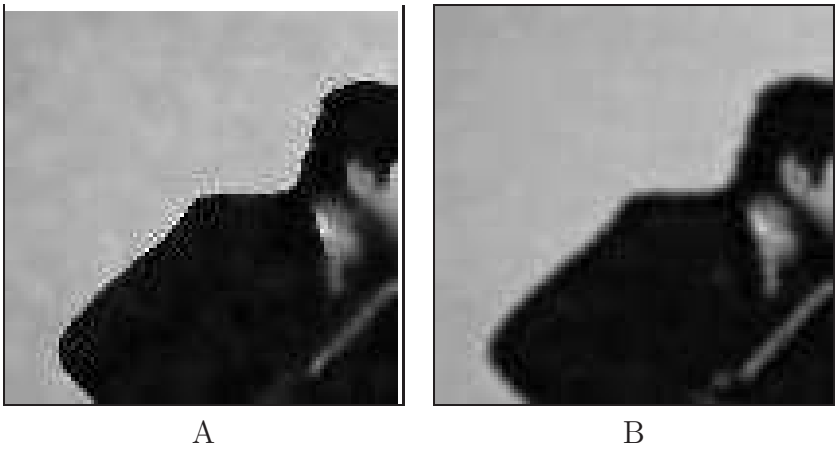

A B

Figure 1.7: A: Enlarged portion of second-order filtered image (Perona-Malik); (B) Enlarged portion of fourth-order filtered image (Lysaker et al. Lysaker et al. (2003)).

1.3 VARIATIONAL METHODS FOR RESTORATION

Variational methods seek to minimize an energy functional. Therefore, the problem is to minimize the energy functional:

$$\underset{u}{argmin} F(u), \tag{1.42}$$

where $F(u)$ is the energy functional to be minimized over the image function u. Let $F'(u)$ denotes the Euler-Lagrange derivative of the functional $F(u)$. The necessary condition for $F'(u)$ to be the minimizer for $F(u)$ is; $F'(u) = 0$, by solving the steady state equation $\frac{\partial u}{\partial t} = 0$, one can obtain the desired solution.

The main objective of energy minimization formulation is to estimate u (the original image) from the statistics of noise and a-priori knowledge of the image features, like smoothness of the image and existence of edges. Let us assume a functional $J(u)$, which measures the quality of the image u i.e., smaller value of $J(u)$ represents a better image. One can see that, under the above assumption, the problem can be solved as a constraint minimization problem:

$$\min_u J(u); \qquad \text{subject to } \|u - u_0\|^2_{\mathcal{L}^2} = |\Omega|\sigma^2. \tag{1.43}$$

Here $\|u - u_0\|^2_{\mathcal{L}^2} = \int_\Omega (u - u_0)^2 dx \approx E(\int_\Omega n^2 dx) = |\Omega|\sigma^2$, (details are presented in Appendix A-3) where $E(x)$ stands for the expectation of the random variable x. An unconstrained formulation of the above minimization equation can be written as:

$$F(u) = \int_\Omega J(u) dxdy + \frac{\lambda}{2} \int_\Omega (u - u_0)^2 dxdy, \tag{1.44}$$

where $J(u)$ stands for the functional to be minimized and λ is a Lagrange multiplier commonly known as regularization parameter, other symbols are in usual sense. Incorporating the notion of blurring kernel (as a general scenario in case of image restoration) the reconstruction models can be reformulated as:

$$\min \int_\Omega J(u)\, dxdy; \qquad \text{subject to } \frac{1}{2}\left(\int_\Omega (k * u - u_0)^2 dxdy - |\Omega|\sigma^2\right) = 0, \tag{1.45}$$

where k is the blurring kernel as described in (1.3). The unconstrained formulation can be written as a Lagrange functional:

$$F(u) = \int_{\Omega} J(u)\, dxdy + \frac{\lambda}{2}\left(\int_{\Omega}(k * u - u_0)^2 dxdy\right), \tag{1.46}$$

λ fetches the same meaning as in (1.44). The details of the above formulation is analyzed in many previous works (Wei and Xu 2009, Marquiana and Osher 2000).

Well-posedness of regularization functionals

We had already defined the notion of well-posedness in Definition 1. For the equation to be well-posed it must satisfy existence, uniqueness and continuity. Consider an image domain Ω which is a bounded Lipschitz domain in $\mathbb{R}^2$. In addition let us assume the following conditions

1. The ideal image $u \in BV(\Omega)$
2. The blurry and noisy observation $u_0 \in L^2(\Omega)$
3. The linear operator $K : L^1(\Omega) \to L^2(\Omega)$ is bounded injective and satisfies the DC condition i.e $K(1) = 1$.

The conditions in (1) and (2) above are necessary to make the formulation meaningful and condition (3) is for proving uniqueness, refer Chan and Shen (2005) for details.

Theorem 2. *(Existence and uniqueness) Under the three conditions defined above the optimal deblurred estimation of* $u^* = min_{\,u} J(u)$ *in the model* (1.45) *exists and is unique.*

Proof. Please refer Theorem 5.2 in Chan and Shen (2005) □

Many promising energy functionals were proposed and analyzed in the literature for $J(u)$ in (1.44). Some of the widely used functionals are $\|\nabla u\|^2_{\mathcal{L}^2}$, which is the $\mathcal{L}^2$ norm of the squared gradient function, this functional was introduced in Tikhonov and Arsenin (1977), $\|\nabla u\|_{TV}$, which is the TV norm of the gradient function, see Rudin et al. (1992) for details and $\|\nabla^2 u\|_{\mathcal{L}^2}$, which is the $\mathcal{L}^2$ norm of the Laplacian of the image (cf. You and Kaveh (2000) and Lysaker et al. (2003)). Each of these functionals were proposed to address various issues and limitations of the previous ones, in the order of their appearance. For instance the TV norm preserves the edges well but results in piece-wise linear approximation of the image, on the other

hand the L^2 functionals (with $\mathcal{L}^2$ norms) perform a planar approximation whereas they smooth-out the high gradient points in the image. Therefore, the choice of the functional is the demand of the situation and should be appropriately chosen based on the application under consideration.

Here we show the numerical implementations and stability of the scheme for a generalized TV based model. Consider the functional to be minimized:

$$F(u) = \int_\Omega |\nabla u|^p \, dxdy + \frac{\lambda}{2}\left(\int_\Omega (u-u_0)^2 dxdy\right), \tag{1.47}$$

where $p \geq 1$ (scalar positive variable). The E-L equation for (1.47) can be written as:

$$u_t = \nabla.\left(|\nabla u|^{p-2}\nabla u\right) - \lambda(u-u_0). \tag{1.48}$$

Note that when $p = 1$ the above models becomes TV-denoising model (Rudin et al. 1992). The numerical implementation using the explicit Euler scheme is:

$$u^{n+1} = u^n + \Delta t\left(\Delta_-^x\left(\frac{\Delta_+^x u^n}{((\Delta_x^+ u^n)^2 + (\Delta_y^+ u^n)^2)^{\frac{2-p}{2}}}\right) + \Delta_-^y\left(\frac{\Delta_+^y u^n}{((\Delta_x^+ u^n)^2 + (\Delta_y^+ u^n)^2)^{\frac{2-p}{2}}}\right)\right) - \lambda(u^n - u_0), \tag{1.49}$$

where Δ_+^x and Δ_+^y denotes the forward and backward difference operators, respectively.

Stability of the numerical scheme

We recall from Proposition 2, the notion of stability for discrete sequences.

Lemma 1. *Consider the discrete scheme in* (1.48)*, subject to the initial data* $u_0 \in l^2$*, then:*

$$\|u(t)\|_{l^p} \leq \|u_0\|_{l^p}, \tag{1.50}$$

where l^p *denotes the space of p-summable sequences and* $\|.\|_{l^p}$ *represents the* l^p *norm*[11] *(Song 2003).*

Proof. We have:

$$\frac{\partial u(t)}{\partial t} = \Delta_-^x D1 + \Delta_-^y D2, \tag{1.51}$$

[11] $\|x_i\|_{l^p} = \left(\sum_{i=0}^{i=N} |x_i|^p\right)^{1/p}$.

where $D1$ and $D2$ are defined as:

$$D1 = \frac{\Delta_+^x u}{((\Delta_+^x u)^2 + (\Delta_+^y u)^2)^{\frac{2-p}{2}}}$$

and

$$D2 = \frac{\Delta_+^y u}{((\Delta_+^x u)^2 + (\Delta_+^y u)^2)^{\frac{2-p}{2}}}.$$

Then

$$\begin{aligned}
\frac{\partial}{\partial t}\sum |u|^p &= p\sum |u|^{p-1}\frac{\partial u}{\partial t} \\
&= p\sum |u|^{p-1}.(\Delta_-^x D1 + \Delta_-^y D2) \\
&= -p\sum \left(D1.\Delta_+^x |u|^{p-1} + D2.\Delta_+^y |u|^{p-1}\right) \\
&= -p(p-1)\sum D1|u|^{p-2}\Delta_+^x u + D2|u|^{p-2}\Delta_+^y u \\
&= -p(p-1)\sum |u|^{p-2}|\nabla u|^p \\
&\leq 0.
\end{aligned}$$

Therefore, l^p norm is non-increasing. Hence, it is l^p stable. □

From the above lemma and Proposition 2 one can infer that the discrete system is stable. The stability aspect is true for all the values of $p \geq 1$ in (1.48). More details of variational schemes are discussed in Chapter 2.

1.3.1 Curvature-based denoising methods

Typical noise-removal schemes driven by curvatures have the form:

$$\partial u/\partial t = F(\mathcal{K})\|\nabla u\|, \tag{1.52}$$

where u is the intensity function and $F(\mathcal{K})$ denotes the speed of the function based on the curvature $\mathcal{K}$ of the level curve. The level-set method introduced by Osher and Sethian (1988) is used as a tool for tracking the evolution of iso-intensity contours.

An anisotropic method is introduced in Alvarez et al. (1992) and Marquiana and Osher (2000), to direct the diffusion in the desired direction, with proper magnitude. If ξ indicates the direction perpendicular to ∇u ($\xi = \frac{1}{\|\nabla u\|}(-u_y, u_x)$), that is, parallel to

the image discontinuities (edges), driving the diffusion of image function u, only in this direction gives:

$$\frac{\partial u}{\partial t} = \mathcal{K}\|\nabla u\| = u_{\xi\xi}. \tag{1.53}$$

The equation (1.53) can be obtained directly from (1.52) by substituting $F(\mathcal{K}) = \mathcal{K}$ (The curvature). The equation in (1.53) is commonly known by the name Mean Curvature Motion (MCM). The level-curves of u in (1.53) are evolving at a speed equal to the mean curvature. Using the central difference scheme, one can write the curvature of the level curve $\mathcal{K}$ as (refer Appendix A-5 for derivations):

$$\mathcal{K} = \frac{u_{xx}u_y^2 - 2u_x u_y u_{xy} + u_{yy}u_x^2}{\|\nabla u\|^3}. \tag{1.54}$$

Therefore, the MCM is formulated as (refer Appendix A-5 for derivations):

$$\frac{\partial u}{\partial t} = \mathcal{K}\|\nabla u\| = \frac{u_{xx}u_y^2 - 2u_x u_y u_{xy} + u_{yy}u_x^2}{\|\nabla u\|^2}. \tag{1.55}$$

Image denoising algorithms based on MCM exploit the fact that curves moving under their mean curvature smooth out and disappear. Very small contours, corresponding to the noise, will disappear quickly. MCM evolves each of the level lines of the image in the gradient direction with a velocity equal to their mean curvature value. However, the continued application of MCM results in blurring and deformation of edges (usually the curved edges appear more curvy) since an image other than a flat one always has some mean curvature value, see Figure 1.8 for the result of MCM based diffusion.

1.3.1.1 Curvature driven diffusion for denoising

Curvature driven diffusion controls the speed of diffusion process based on the curvature at any point. The commonly used curvatures are the curvature of the level curve and mean curvature of the surface. The mean curvature is the mean of principal curvatures which is defined as:

$$H = \frac{1}{2}\left(\mathcal{K}_1 + \mathcal{K}_2\right), \tag{1.56}$$

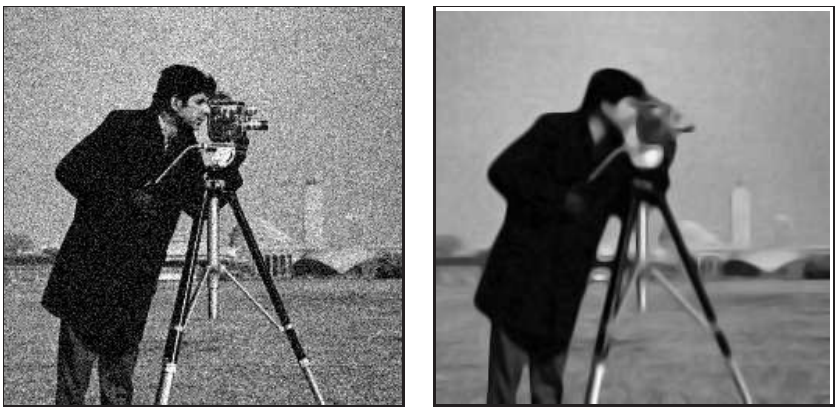

A B

Figure 1.8: Results of MCM filter: (A) Noisy input image; (B) Result of MCM.

where $\mathcal{K}_1$ and $\mathcal{K}_2$ are the *maximal* and *minimal* curvatures respectively (principal curvatures) of a given point p on a surface S. The mean curvature value tends to zero when all the principal curvature values tend to zero. So the diffusion process driven by mean curvature may slash-out features with non-zero mean-curvature values. In practice one can notice that, many of the natural images contain meaningful features with non-zero mean curvature values, curvy edges and corners are some of the examples. Another commonly used curvature is Gauss curvature which is defined as the product of principle curvatures:

$$GC = \mathcal{K}_1 \times \mathcal{K}_2, \tag{1.57}$$

here GC stands for the Gauss-curvature. Unlike mean curvature the Gauss curvature does not affect the features with non-zero mean curvature. Since, Gauss-curvature being the product of curvatures it becomes zero even if any one of the principal curvatures is zero. Therefore, Gauss curvature tries to remove isolated points or noise, mean while it leaves other features untouched. A detailed explanation of curvature driven diffusion process in given in Chapter 3.

1.4 QUALITY MEASURES

The reconstruction is quantified using various statistical measures. We consider the following measures for comparing and quantifying the reconstruction capabilities of different methods under consideration. Though, the perspective results are evident

from the figures shown in favor of different methods, proper quantification is necessary to comment on the performance of various filters. We will be using these measure in subsequent chapters, for quantifying various methods considered in the literature and the ones proposed as a part of this thesis.

1.4.1 Signal-to-noise Ratio (SNR)

The Signal-to-Noise Ratio (SNR) is a commonly used measure to quantify the denoising capability of a filter (Russ 2007, Gonzalez and Woods 2001). The SNR is defined as:

$$SNR = 10 \ \ log_{10}\left(\sigma_f^2/\sigma_n^2\right), \tag{1.58}$$

where σ_f^2 is the variance of the noise free image and σ_n^2 is the variance of the noise. A larger SNR value indicates a better image-denoising capacity.

1.4.2 Pratt's Figure of Merit (FOM)

The efficiency of any enhancement method is measured in terms of its capability to retain the edges while removing the noise. The edge preservation capability of various enhancement methods are compared using Pratt's Figure Of Merit(FOM) (Pratt 1977) defined as:

$$FOM = \frac{1}{max\{\hat{N}, N_{ideal}\}} \ \ \sum_{i=1}^{\hat{N}} \frac{1}{1 + d_i^2 \alpha}, \tag{1.59}$$

where $\hat{N}$ and N_{ideal} are the number of detected and ideal edge pixels, respectively, d_i is the Euclidean distance between the i^{th} detected edge pixel and the nearest ideal edge pixel, and α is a constant typically set to 1/9. FOM ranges between 0 and 1, with unity for ideal edge detection. We apply Canny edge detector (Canny 1986) for locating the edges. The standard deviation of the Gaussian kernel in the Canny detector is chosen as $\sigma = 0.1$.

1.4.3 Structural SIMilarity Index (SSIM)

The structure similarity (SSIM) index is used to compare the luminance, contrast and structure of two different images (Wang and Bovik 2004). The motivation to use this approach is to find a more direct way to compare the structures of the reference and the distorted images. This new framework for the design of image quality measures was

proposed, based on the assumption that the human visual system is highly adapted to extract structural information from the viewing field, the SSIM is formulated as:

$$SSIM(x,y) = \frac{(2\mu_x\mu_y + C1) \times (2\sigma_{xy} + C2)}{(\mu_x^2 + \mu_y^2 + C1)(\sigma_x^2 + \sigma_y^2 + C2)}, \tag{1.60}$$

where x and y denote the content of local windows in original and reconstructed images respectively, σ_{xy} is the covariance of x and y, σ_x^2 and σ_y^2 denotes the variance of x and y respectively and $C_1 = (k_1 L)^2, C_2 = (k_2 L)^2$ where L is the dynamic range of pixels values ([0-255] for 8 bit gray scale image), $k_1 = 0.01$ and $k_2 = 0.03$ are constants. The measure is applied for non-overlapping windows in both the images (original and reconstructed). In this thesis work we measure mean-SSIM (MSSIM) which is an index to evaluate the overall image quality. It is defined as:

$$MSSIM(X,Y) = \frac{1}{M}\sum_{j=1}^{M} SSIM(x_j, y_j), \tag{1.61}$$

where X and Y are the original and reconstructed images respectively; x_j and y_j denote the content of the j^{th} local window in reference and distorted images respectively and M is the number of local windows in the image.

1.4.4 Contrast-to-Noise Ratio (CNR)

One of the widely used quality measures for measuring the contrast enhancement capability of the filter in hand is, Contrast-to-Noise Ratio (CNR) (Geissler et al. 2007). CNR measures the contrast enhancing capacity of the filter. Contrast to noise ratio is the relationship of signal intensity differences between two regions, scaled to image noise. Improving CNR increases perception of the distinct differences between two areas of interest. CNR can be evaluated for two regions of interest (say the object and the background) using the equation:

$$CNR = \frac{\mu_o - \mu_b}{\sqrt{\sigma_b^2 + \sigma_o^2}}, \tag{1.62}$$

where μ_o, μ_b are the mean of object and background pixels and σ_o^2, σ_b^2 are the variances of object and background pixels, respectively. The CNR value indicates the change in contrast of two different regions. As the noise in the regions reduces, the contrast

between the regions increases and therefore CNR also increases. Similarly the CNR increases with increase in the contrast between regions. Therefore, CNR is a summary of SNR and contrast.

1.4.5 Peak Signal to Noise Ratio (PSNR)

The mean square error (MSE) is an effective statistical measuring standard to quantify the performance of a reconstruction method under consideration. MSE gives a clear understanding of how far the actual images are, from the reconstructed ones. So does the PSNR. MSE and PSNR are formulated as:

$$MSE = \frac{1}{n \times m} \sum_{i=0}^{m-1} \sum_{j=0}^{n-1} [u(i,j) - u_0(i,j)]^2 , \tag{1.63}$$

and PSNR is defined in terms of MSE as:

$$PSNR = 10log_{10} \left(MAX_u^2 / MSE \right) , \tag{1.64}$$

where $n \times m$ is the image size and MAX_u is the maximum gray-value of the image (generally taken as 255 in case of gray-level/RGB images). The unit is measured in decibel (dB). The value PSNR indicates the quality of reconstruction or extent of noise removing capability of the filter under consideration. The higher value of PSNR signifies a better reconstruction capacity of the filter in hand. As the amount of noise decreases in an image the PSNR value increases.

1.5 ORGANIZATION AND CONTRIBUTION OF THE THESIS

In this thesis we try to address shortcomings of some of the Variational and PDE based methods proposed in the literature for image denoising, restoration and inpainting.

In the first place, the second-order diffusion filters approximate the observed image with piece-wise linear images when they evolve with respect to time. This type of approximation causes visual discrepancies in the filtered output image. Secondly these filters takes large number of iterations to converge to the desirable solution even when the time step is chosen appropriately. Moreover, some of the second-order diffusion

filters proposed in the previous works use a variation of mean curvature to drive the diffusion process (or diffuses based on the mean curvature). This causes the filter to slash-out some of the features having non-zero mean curvature values, like curved edges, corners etc., during the evolution process. In this thesis we design methods (filters) to address the defects of these filters in an effective way. The rest of the chapters in this thesis are organized as follows.

A regularized time dependent second-order anisotropic switching filter is devised in Chapter 2. This filter catalyzes the diffusion process by relaxing the condition for the stability and diffuses anisotropically only in the areas with high frequency information and diffuses like a Laplacian isotropic filter in the smooth or homogeneous areas. The filter behaves very well with the natural images.

In Chapter 3 we introduce an enhancement filter based on the Gauss curvature. The diffusion process in this filter is driven by Gauss curvature value at each pixel and a coupled stable hyperbolic shock filter enhances the image edges (while diffusing out the noise). The filter preserves and enhances the features even with non-zero mean curvature values. However, the noise features are removed effectively.

A third-order Gauss curvature driven image inpainting filter is proposed in Chapter 4. This PDE reconstructs images from their degraded observations and inpaints the desired domain. Since Gauss curvature drives the whole evolution process, the image features with non-zero mean curvature values are preserved while the image is being reconstructed (from blurred and noisy observations) or inpainted. In the non-inpainting domain the filter gets transformed to a normal TV image restoration.

In Chapter 5 we propose a fourth-order anisotropic denoising and deblurring filter which can address some of the issues with the commonly used fourth-order filters like You-Kaveh filter (You and Kaveh 2000), Tai filter (Lysaker et al. 2003) and Hajiaboli filter (Hajiaboli 2010). The proposed filter will diffuse anisotropically by preserving the planar approximation and ramp edges in the images while enhancing the high-frequency components present in the images.

We conclude this thesis in Chapter 6 throwing highlights on possible future works and describing the pros and cones of the methods proposed and contributed as a part of this thesis work. All the methods proposed are numerically verified and results are compared and analyzed in each chapters for the respective methods.

Chapter 2

VARIATIONAL METHODS FOR IMAGE RESTORATION

2.1 INTRODUCTION

Partial Differential Equations (PDE's) and Variational Methods are widely used for image denoising and deblurring (refer Kornprobst et al. (1997), Rudin et al. (1992), Chan et al. (2001), Lysaker et al. (2003) and You and Kaveh (2000) for details). In PDE based methods, the image gets evolved with respect to time. The evolution eventually results in simplification or enhancement of the image features. The variational methods seeks to minimize the corresponding energy functional and regularizes the diffusive and reactive (fidelity) terms in the functional, using a regularization parameter (Rudin et al. 1992). Regularized solutions were provided for some of the PDE based image simplification and enhancement methods as well (Lysaker et al. 2003, Weickert 1997, Catte et al. 1992). Peter et al. (2010) proposed a regularization method based on the Non-Local Means (NLM) (Buades et al. 2005) filter. In this work the authors combine the NLM filter with a deblurring term to reconstruct the images. PDE and variational methods are quite well known for handling the ill-posed problems like deblurring and denoising, because the uniqueness and the stability of the solution can be derived effectively.

We recall from Chapter 1, the commonly used functionals for regularization are Tikhonov and TV. However, Tikhonov based functional uses $\mathcal{L}^2$ norm, which penalizes much on the image edges. In other-words, $\mathcal{L}^2$ norms do not encourage discontinuities in the solution. Therefore, Tikhonov regularization method is not widely used in

image processing. TV based approaches use a TV norm, which allows discontinuities in the solution, thus helps in retaining the edges in the image while denoising them. Nonetheless, the evolution of the non-linear PDE associated with the TV regularization functional converges slowly and the convergence heavily depends on the time step parameter. This drawback of TV was addressed to a considerable extent in Marquiana and Osher (2000).

Besides the slow convergence, another major shortcoming of TV based regularization methods (being second order diffusion methods) is the *staircase* effect. The TV based techniques (like other second order diffusion methods) approximate the homogeneous areas in the image with constant intensity patches that causes a visual discrepancy called *staircase* effect. Many methods were proposed subsequently in the literature to address the *staircase* effect. Majority of these methods rely on the energy functionals with higher-order evolution PDE (You and Kaveh 2000, Lysaker et al. 2003). However, the higher-order PDEs when used in the evolution equations, may result in an over-smoothed resultant image (with blurred edges). Another improved method was proposed by Wei and Xu (2009) and Blomgren et al. (1997), in these works, the authors proposed a regularization functional, which is a convex combination of TV and $\mathcal{L}^2$ norms, together with a parameter to select the contribution of each of these norms. This method could address the issue due to the *staircase* effect to a considerable limit, by providing a better approximation of the homogeneous areas in the images. Nevertheless, this method also has a slow convergence rate and the stability of the solution depends highly on the time step parameter of the evolution PDE. Another noticeable issue with TV based and Tikhonov based methods is that even though the energy functional is convex, the Euler-Lagrange equations associated with the energy functional is non-linear and are generally ill-conditioned.

Many implicit and semi-implicit iterative solutions were proposed in the literature for solving this non-linear PDE, refer Chan and Mulet (1999) and Vogel and Oman (1996) for details. The implicit solution proposed by (Chan and Mulet 1999) uses a primal-dual quadratic method and the linear semi-implicit method proposed by Vogel and Oman (1996), uses a fixed-point iteration method. These methods provide a faster convergence at the cost of high computational complexity. Moreover, in implicit methods one has to solve a system of linear equations in each iterations to find the desired solution. Therefore, in case of restoration problems (when the problem is ill-posed) the computational cost is moderately high (Vogel and Oman 1996).

The overheads due to the slow convergence of the TV based methods were addressed by Marquiana and Osher (2000). In Marquiana and Osher (2000), the authors proposed a model based on the level-set motion and established that the steady state can be reached quickly by the explicit time marching scheme. In this model the diffusion term is Mean Curvature Motion (MCM). We recall from Chapter 1 that, MCM is a purely anisotropic diffusion method, in which the level-lines move with a speed proportional to their mean curvature in the direction normal to the level-curves. Hence, the diffusion takes place along the direction of the level-lines, not across it. This property of the filter is desirable in the regions of the images dominated by edges, finer details and textures; whereas, it is rather a liability in the smooth or homogeneous areas. In the homogeneous areas the anisotropic diffusion pretends to form constant intensity patches resulting in the *staircase* effect (You and Kaveh 2000).

All these facts (mentioned above) motivate one to propose a time dependent curvature based image reconstruction method, whose steady state is attained quickly by explicit time marching method. The filter proposed in this chapter denoises anisotropically in the areas dominated by the edges and isotropically on the homogeneous areas. The switching of this filter between anisotropic and isotropic behaviors is based on the local image gradient features. The isotropic diffusion on the homogeneous areas approximates the filter to a "Laplacian" filter. One can easily see that the energy functional associated with the "Laplacian" is induced by a $\mathcal{L}^2$ norm. In other-words, for the energy functional with $\mathcal{L}^2$ norm, the Euler-Lagrange equation consists of a "Laplacian" operator. As we have already mentioned in Chapter 1, though the $\mathcal{L}^2$ norm penalizes more on the image edges, but rarely leads to the formation of constant patches, that results in a *staircase* effect. However, the areas in the image dominated by the edges and finer details (like textures), the diffusion process gets transformed to an anisotropic one and does not diffuse at-all in the direction of the gradient; making the edges intact even after many iterations. The experimental results provided show the capability of the method to reduce *staircase* effect while deblurring and denoising the images.

The rest of this chapter is organized in three sections. Section 2.2 explains the background of regularization methods for image reconstruction. The proposed model and the numerical implementations are described in Section 2.3. Section 2.4 gives a detailed explanation and inferences regarding the results and the experiments conducted.

2.2 REGULARIZATION APPROACHES FOR IMAGE ENHANCEMENT

A mathematical formulation for image degradation model was provided in Chapter 1 equation (1.1). We recall the model:

$$Ku + n = u_0,$$

all the symbols have same meaning as in (1.1). Further assuming the operator K as translational invariant, linear and bounded, (1.1) can be reformulated as a convolution operation with k as the PSF defined in (1.3). Now, the reconstruction problem is to determine the original image u from the observed blurred and noisy image u_0. As pointed out in Chapter 1, this problem belongs to an ill-posed one in the sense of Hadamard (1953). Therefore, the usual way to solve this problem is to employ some regularization approaches.

2.2.1 Regularization methods

Fourier transform based regularization filters (FFT-REG-Filter) were used earlier, for deblurring and denoising the images (Bertero and Boccacci 1998), and can be read as:

$$\hat{u}(\omega) = \frac{\hat{u_0}(\omega)\hat{k}(\omega)}{\|\hat{k}(\omega)\|^2 + \lambda}, \tag{2.1}$$

where $\hat{x}$ denotes the Fourier transform of the function x, λ is a positive regularization parameter, $\|.\|$ denotes the usual Euclidean norm and ω denotes a frequency variable. The solution is obtained in the frequency domain. The other symbols in (2.1) are as in (1.1) (refer Appendix A-3 for details on derivation of (2.1)). Here one can see that, the solution is defined in the space that allows discontinuities. Hence the image gets deblurred, but hardly denoised. Therefore, the obvious alternative is to use the Sobolev regularization filter (SOB-REG-Filter) (Bertero and Boccacci 1998), which is defined in a space that does not allow the discontinuities in the function. The Sobolev filter can be written as:

$$\hat{u}(\omega) = \frac{\hat{u_0}(\omega)\hat{k}(\omega)}{\|\hat{k}(\omega)\|^2 + \lambda S(\omega)}, \tag{2.2}$$

here the notations have the same meaning as in (2.1), the term $S(\omega) = \|\omega\|^2$ is the Fourier transform of the "Laplacian" of the image function u. This filter denoises the image well but penalizes more on the edge features. Therefore, the filters in (2.1) and (2.2) do not provide satisfactory reconstruction results (refer Appendix A-3 for detailed derivation of (2.2)).

A statistical regularization filter named Weiner filter (Wiener Norbert 1949) is a popular image restoration filter. An optimal Weiner filter in Fourier domain is given as:

$$W(\omega) = \frac{K(\omega)^* S_{uu}}{|K(\omega)|^2 S_{uu} + S_{nn}} = \frac{K(\omega)^*}{|K(\omega)^2| + r_\omega}, \tag{2.3}$$

where K^* is the adjoint of the matrix K (associated with the operator). S_{uu} and S_{nn} are the variances of data and noise, respectively and ω is a frequency variable. The noise variance S_{nn} can be assumed to be σ^2. Since the signal variance S_{uu} is bounded, the regularizer r_ω is bounded well above zero. The filter is assumed to produce an optimal result under the following conditions.

1. The operator K is shift invariant and the PSF is known in advance.

2. Both noise and image have to be wide-sense homogeneous and wide-sense stationary[1], and the statistical properties of S_{nn} and S_{uu} are known in advance.

An improved version of Weiner filter is proposed in Hillery and Chin (1991) and Lee (1980). However, the Weiner filter is a least square error minimization filter which performs a linear estimation of the image, refer Appendix A-3 for derivation of Weiner filter. Furthermore, one can identify that the least square approximations are well defined in a space that does not allow discontinuities in the solution, therefore the filtered images appears considerably smoothened (this fact is visible in the results provided in the later section, in favour of this method). Moreover, Weiner filter requires the variances of the noise free signal and the noise for its computation, which may not be available in all practical scenarios.

All the above regularization methods are non-iterative in nature and when they are applied to the non-linear deblurring problem they don't perform well. To solve

[1]The signal is wide-sense stationary if ,$\forall k, m$

- $E[u_k] = E[u_0]$
- $R_x(k, m) = R_x(m - k)$,

where $R_x(k)$ is the even auto-correlation function, u_k is the image and u_0 is the initial image.

such non-linear problems iterative regularization approaches are quite often employed. We discuss some iterative regularization methods in the following paragraphs.

Tikhonov regularization or *penalized least squares* is a widely used iterative regularization approach (Tikhonov and Arsenin 1977). This method uses the regularization functional: $J(u) = \|\nabla u\|^2_{\mathcal{L}^2}$. Thus with the help of (1.43), the restoration problem can be stated as:

$$\min_u \int_\Omega \|\nabla u\|^2_{\mathcal{L}^2}\, dxdy; \qquad \text{subject to } \frac{1}{2}\|k * u - u_0\|^2_{\mathcal{L}^2} - |\Omega|\sigma^2 = 0. \tag{2.4}$$

The "Lagrangian" of (2.4) is:

$$\int_\Omega \|\nabla u\|^2_{\mathcal{L}^2}\, dxdy + \frac{\lambda}{2}\left(\int_\Omega (k * u - u_0)^2 dxdy - |\Omega|\sigma^2\right). \tag{2.5}$$

The minimization problem can be read as:

$$J(u) = \frac{\lambda}{2}\left(\int_\Omega (k * u - u_0)^2 dxdy - |\Omega|\sigma^2\right) + \int_\Omega \|\nabla u\|^2_{\mathcal{L}^2} dxdy, \tag{2.6}$$

where λ is the regularization parameter (Lagrange multiplier) and ∇u is the gradient of the image function u. The first term in (2.6) is a reactive or fidelity term and the second one is a diffusion [2] (refer to Appendix A-3 for derivation of the fidelity term). Both the terms in (2.6) are well defined in the space :

$$W^{1,2}(\Omega) = \{u \in L^2(\Omega); \nabla u \in L^2(\Omega)^2\}. \tag{2.7}$$

The problem $inf\{J(u), u \in W^{1,2}\}$ admits a unique solution characterized by the following Euler-Lagrange (E-L) equation:

$$\lambda k * (k * u - u_0) - \nabla^2 u = 0, \tag{2.8}$$

where $\nabla^2 u$ denotes the "Laplacian" of u. Now the gradient descent equation is:

$$\frac{\partial u}{\partial t} = \nabla^2 u - k * (k * u - u_0). \tag{2.9}$$

[2]The diffusion term does the denoising and fidelity term ensures a minimum deviation of solution image from the actual one.

This PDE is a Boundary Value problem with Neumann boundary condition (1.30) and the initial condition (1.31). The parameter λ is updated in each iteration of the process using the following expression:

$$\lambda(t) = \frac{\int_\Omega k * (k * u - u_0)\,(u_{xx} + u_{yy})\,dxdy}{\int_\Omega (k * (k * u - u_0))^2 dxdy}. \tag{2.10}$$

This provides a dynamic procedure for restoration. As $t \to \infty$, the steady state solution gives the restored image. Since, the "Laplacian" operator is isotropic in nature (as we have already discussed in Chapter 1), the process will diffuse in all directions with equal magnitude, which eventually results in a smoothed output image. Therefore, Tikhonov based regularization is not well suited for images with sharp discontinuities (edges or finer-details). Furthermore, as already discussed in Chapter 1, the $\mathcal{L}^p$ norm with $p = 2$ removes the noise but penalizes more on the gradients corresponding to the edges. Another observation made is; as p decrease from 2 to 1, the edge preserving capacity of the filter gradually increases, with the maximum value when $p = 1$.

Another improved regularization method was proposed in Rudin et al. (1992) (ROF-Model). This method uses a Total Variational (TV) functional in place of $J(u)$, i.e.,

$$J(u) = TV(u) = \int_\Omega \|\nabla u\|\, dxdy = \int_\Omega \sqrt{u_x^2 + u_y^2}\, dxdy. \tag{2.11}$$

Among all the norms, only the TV norm allows discontinuities in the solution and therefore, with the help of TV norm, one can recover images without losing majority of edge features present in them. The ROF model can be written in energy minimization form as:

$$\min_u \int_\Omega \|\nabla u\|_{TV}\, dxdy \tag{2.12}$$
$$\text{subject to } \left(\frac{1}{2}\|k * u - u_0\|_{\mathcal{L}^2}^2 - |\Omega|\sigma^2\right) = 0.$$

The "Lagrangian" of (2.12) is written as:

$$\int_\Omega \|\nabla u\|_{TV}\, dxdy + \frac{\lambda}{2}\left(\int_\Omega (k * u - u_0)^2 dxdy - |\Omega|\sigma^2\right). \tag{2.13}$$

The energy functional for ROF model can be read as:

$$J(u) = \frac{\lambda}{2}\left(\int_{\Omega}(k*u-u_0)^2dxdy - |\Omega|\sigma^2\right) + \int_{\Omega}\|\nabla u\|_{TV}dxdy. \tag{2.14}$$

Here $\|.\|_{TV}$ is the TV norm associated with the image function u. The Euler-Lagrange equation associated with this energy functional can be written as:

$$\lambda k*(k*u-u_0) - \nabla.\left(\frac{\nabla u}{\|\nabla u\|}\right) = 0. \tag{2.15}$$

The gradient descent equation is:

$$\frac{\partial u}{\partial t} = \nabla.\left(\frac{\nabla u}{\|\nabla u\|}\right) - \lambda k*(k*u-u_0) \tag{2.16}$$

At steady state the PDE defined in (2.16) can be written as:

$$-\lambda k*(k*u-u_0) + \nabla.\left(\frac{\nabla u}{\|\nabla u\|}\right) = 0. \tag{2.17}$$

One can easily find that (2.17) is degenerating when $1/\nabla u \to 0$. Hence, it is common to perturb the initial value of the TV norm with a small positive quantity β. With the perturbation defined above the TV norm is modified as:

$$\int_{\Omega}\sqrt{\|\nabla u\|^2+\beta}dxdy, \tag{2.18}$$

where β is a small positive parameter. Hereafter we denote this perturbed TV norm by: $\int_{\Omega}\|\nabla u\|_{\beta}\,dxdy$. The parameter λ is updated using the equation:

$$\lambda(t) = \frac{\int_{\Omega}k*(k*u-u_0)\left(\frac{\partial}{\partial x}\frac{u_x}{\sqrt{u_x^2+u_y^2}} + \frac{\partial}{\partial y}\frac{u_y}{\sqrt{u_x^2+u_y^2}}\right)dxdy}{\int_{\Omega}(k*(k*u-u_0))^2dxdy}. \tag{2.19}$$

The above expression for λ is obtained by multiplying (2.15) with $k*u-u_0$ and integrating over the image domain. We recall that, as $t\to\infty$, the steady state solution approaches the original image. The natural choice of the space in which the

terms in (2.14) are well defined is:

$$V = \{u \in L^2(\Omega); \nabla u \in L^1(\Omega)^2\}. \tag{2.20}$$

Many methods were suggested in the literature to solve the Euler-Lagrange equation in (2.17), see Chan and Mulet (1999) and Chan and Mullet (1996). All these methods belong to the time-dependent approximation of the ill-conditioned E-L equation in (2.17). Both the approaches in Chan and Mulet (1999) and Chan and Mullet (1996) are inefficient, because the steady state is reached in a very small time step, when the explicit scheme is used. The following formulation is due to Rudin et al. (1992).

$$\frac{u_t^{n+1} - u_t^n}{\Delta t} = -\lambda k * (k * u_t^n - u_0) + \nabla. \left(\frac{\nabla u^n}{\|\nabla u^n\|_\beta} \right), \tag{2.21}$$

with the initial condition (1.31) and the boundary condition (1.30). As t increases we obtain the restored versions of the input image. The evolution equation in (2.21) converges very slowly. The diffusion term in (2.21) is parabolic and is singular for smaller values of $\|\nabla u\|$. Hence, it would be beneficial to put a restriction on the time step parameter in order to ensure the stability in the evolution process. This is described by CFL condition defined in (1.21)

In Marquiana and Osher (2000) (MO-based model), the authors relax this CFL condition, in order to avoid the difficulties due to the time step constraints. The method in Marquiana and Osher (2000) is a time-dependent model that accelerates the movement of level-curves of u and regularizes the diffusion term in a non-linear way. In the work Marquiana and Osher (2000), the authors propose to multiply the steady state E-L equation in (2.17) with the magnitude of the gradient, the model can be read as:

$$0 = -\|\nabla u\| \lambda \; k * (k * u - u_0) + \|\nabla u\| \nabla. \left(\frac{\nabla u}{\|\nabla u\|_\beta} \right), \tag{2.22}$$

with the boundary condition in (1.30) and the initial condition in (1.31). One can easily observe in (2.22) that, the diffusion term is purely a Mean Curvature Motion (MCM) (Marquiana and Osher 2000). In MCM the level curves move towards the zeros of $k * u - u_0$, with a speed proportional to their mean curvatures. Therefore, the noise gets diffused at a faster rate and the steady-state is attained quickly. The areas where $k * u - u_0$ is zero or in the homogeneous areas, only the anisotropic diffusion

(induced by MCM) will be active (the effect of fidelity term will be zero), whereas, at the non-zero points of $k * u - u_0$, the fidelity term will have a contribution regularized by the magnitude of the gradient. This would eventually retain and sharpen the edges while denoising the images. Analytically it can be shown that this solution procedure approaches the same steady state as in (2.17), whenever u has non-zero gradient. The scalar (gradient) multiplication of (2.17) at steady state, does not affect the expression to evaluate λ. Therefore, the same expression in (2.19) can be used for evaluating and updating λ, in each iteration.

The anisotropic nature of MCM forces the filter to diffuse only in the direction tangent to the level curve, because MCM has a component only along the tangent and the component normal to the curve is zero. This property of MCM is highly desirable in the areas of the image dominated by the high frequency components (or edges and finer details). However, in the constant intensity areas MCM will results in forming constant intensity patches causing the *staircase* effect.

2.3 SWITCHING ANISOTROPIC ENHANCEMENT MODEL (SAEM)

After due consideration of the facts discussed above, we propose to couple the fidelity term in (2.22) with a diffusion term, which behaves like MCM in the areas of the image dominated by edges and finer details and like a "Laplacain" filter in the homogeneous intensity areas. The proposed model results in enhancement of edges, while removing the noise in an anisotropic manner. The proposed method can be mathematically formulated as:

$$u_t = -\lambda \|\nabla u\| k * (k * u - u_0) + c\left(\phi_\tau(\|\nabla u\|_\sigma) u_{\eta\eta} + u_{\xi\xi}\right), \tag{2.23}$$

where ξ is the direction along the level-curve and η is the direction along the gradient. The function $\phi_\tau : \mathbb{R} \to \{0, 1\}$ is defined as: $\phi_\tau(x) = 1$ if $x < \tau$, zero otherwise. Here $\|\nabla u\|_\sigma$ is the gradient magnitude of the Gaussian convolved version of the image (with the standard deviation σ). One can easily observe from (2.23) that, in constant intensity areas the function $\phi(.)$ will return a value one and the diffusion term will transform to an ordinary "Laplacian" filter $\nabla^2 u$, which is isotropic. Therefore, the diffusion term is: $u_{\xi\xi} + u_{\eta\eta}$. Note that, the term $u_{\xi\xi}$ in (2.23) denotes MCM. In the

regions dominated by edges and finer details, the function $\phi_\tau(x)$ returns a value zero, this transforms the filter to a MCM($u_{\xi\xi}$). As already mentioned, the MCM filter is a anisotropic filter that approaches the steady state at a faster rate.

The parameter τ in the function $\phi_\tau(.)$ is a gradient threshold parameter. This parameter provides necessary inputs to the filter to switch between isotropic and anisotropic behavior. When the value of τ is kept very low (near to zero), the filter switches to a "Laplacian" filter, only in the constant intensity areas. Whereas, when the value of τ is quite high, then some of the edge features having the gradient magnitude value less than τ will get smoothed out. As, the smooth regions always need not be constant intensity regions, the switching of the filter may not give impressive results, if the value of τ is kept very low. Therefore, one should give due care while selecting the value of τ for obtaining proper results.

The scalar regularization parameter λ controls the smoothing and fidelity characteristics of the filter. When λ is very small, then the noise features remains not much affected by the diffusion flow. But when λ is quite large then denoising happens to a considerable extend and the stability and fidelity of the filter will be largely affected. Since, the restored version of the image changes in each iteration of the evolution process, the parameter λ also needs to be updated in each iteration based on the restored version of the image. Therefore, λ is evaluated and updated in each iteration using (2.19). The evaluated value $\lambda(t)$ denotes the scalar regularization parameter at the t^{th} iteration. The parameter c determines the magnitude of diffusion. The magnitude of diffusion increases with increase in the value of c. An analysis of the effect of each parameter on the filtered results is done in Section 2.4.2.

The anisotropic diffusion term in (2.23) will not result in approximating the homogeneous regions with constant patches, which eventually results in the *staircase* effect. Since, the filter does not have any component in the direction of the gradient (in the high gradient regions in the image), the high frequency components like the edges and the finer details are not severely affected by the diffusion flow. The proposed filter can still relax on the CFL condition as in (2.22). This filter speeds-up the level curves of the image function u and regularizes the parabolic diffusion term in a non-linear way. The initial condition (1.31) and the boundary condition (1.30) are assumed for this PDE as well.

2.3.1 Numerical implementations

The gradient descent scheme is used for solving the PDE in (2.23), see Section (1.2.1.4) for details on the scheme. Explicit Euler schemes are followed for discretizing the PDE in (2.23), the details were provided in Section (1.2.1.5). Since the fidelity term (the second term) in (2.23) is hyperbolic, the usual central difference scheme may not help in getting a proper result. This scheme will be highly unstable and may not converge. So we use the *upwind* scheme proposed in Osher and Sethian (1988) for solving the diffusion term (which has an hyperbolic term) in (2.23). The scale space parameter h is assumed to be 1 and Δt is the time step. Using the *upwind* for solving $\|\nabla u\|$ in (2.23) will result in the following expressions.

$$\|\nabla u\| = \sqrt{D_x^2 + D_y^2}, \tag{2.24}$$

where $D_x = minmod(u_x^+(x,y), u_x^-(x,y))$, $D_y = minmod(u_y^+(x,y), u_y^-(x,y))$ and the *minmod* operator is defined as:

$$minmod(x,y) = \begin{cases} min(\|x\|, \|y\|) & \text{if } xy > 0, \\ 0 & \text{Otherwise.} \end{cases}$$

The first order forward, backward and central difference operators are as follows:

$$u_x^+(x,y) = u(x+1,y) - u(x,y),\ u_x^-(x,y) = u(x,y) - u(x-1,y), \tag{2.25}$$
$$u_x(x,y) = (u_x^+ + u_x^-)/2,\ u_y^+(x,y) = u(x,y+1) - u(x,y),$$
$$u_y^-(x,y) = u(x,y) - u(x,y-1),\ u_y(x,y) = (u_y^+ + u_y^-)/2. \tag{2.26}$$

Using the explicit Euler equation with finite central difference scheme for rest of the terms in differential equation in (2.23) will yield the following finite differences:

$$u_{\eta\eta} = \frac{u_{xx}|u_x|^2 + 2u_{xy}u_xu_y + u_{yy}|u_y|^2}{1 + |u_x|^2 + |u_y|^2}, \tag{2.27}$$

and $u_{\xi\xi}$ is discretized as :

$$\frac{u_{xx}|u_y|^2 - 2u_{xy}u_xu_y + u_{yy}|u_x|^2}{1 + |u_x|^2 + |u_y|^2}. \tag{2.28}$$

where

$$\begin{aligned} u_{xx} &= u(x+1,y) - 2u(x,y) + u(x-1,y), \\ u_{yy} &= u(x,y+1) - 2u(x,y) + u(x,y-1), \\ u_{xy} &= (u_x(x+1,y) - u_y(x,y-1))/2. \end{aligned} \tag{2.29}$$

With the help of above discretizations, we can discretize the PDE in (2.23):

$$\begin{aligned} u^{n+1} = u^n - \Delta t \times (\lambda \|\nabla u^n\| k * (k * u^n - u_0) \\ + c(\phi_t(\|\nabla u^n\|_\sigma) u_{\eta\eta} + u_{\xi\xi})). \end{aligned} \tag{2.30}$$

2.3.2 The stopping rule

A number of stopping rules were proposed for determining the optimal number of iteration to get the desired results. Many of them rely on the normalized mean square error in the subsequent iterations or absolute error in each iterations etc., see Rudin et al. (1992), Lysaker et al. (2003) and Lee and Seo (2005). Here we propose to use the Normalized Relative Root Mean Square Error (NRRMSE) in each iteration to put a hold on the iteration process. The NRRMSE is a measure to indicate the Root Mean Square Error in each iteration for a particular method. The NRRMSE keeps on decreasing in each iteration during the diffusion process as the filtered image approaches the original one. NRRMSE is defines as:

$$NRRMSE = |RMSE_i - RMSE_{i+1}|/RMSE_{i+1}, \tag{2.31}$$

where $RMSE_i$ denotes the Root Mean Square Error in the i^{th} iteration. RMSE for a $M \times N$ image is defined as:

$$RMSE_i = \left(\frac{1}{N \times M} \sum_{i=1}^{N} \sum_{j=1}^{M} (u_o^i(i,j) - u(i,j))^2 \right)^{1/2}, \tag{2.32}$$

where u_o^i is the observed image at i^{th} iteration and u is the actual image. When the noise gets smoothed out the reconstructed image gets closer to the original one. The NRRMSE keeps on decreasing with each iteration and becomes less than a threshold t after a finite number of iterations. The infimum of the values of n, for which the

NRRMSE becomes less than the threshold t is taken as the optimal iteration number. The reconstruction will be optimal when the iteration number is fixed this way. The graph in Figure 2.1 shows the optimal iteration number for different methods existing in the literature and for the method proposed in this chapter (SAEM). In Figure 2.1(A) we plot the NRRMSE of different methods along with the SAEM, for different iteration numbers. In Figure 2.1(A) the variation of NRRSE against the number of iterations is not clearly visible for MO-based and the SAEM method, so we plot these two methods separately in Figure 2.1(B). The images shown in Figures 2.2, 2.3, 2.5, 2.6,2.7 and 2.8 are taken after the corresponding optimal number of iterations for each method. The threshold for calculating iteration number based on the NRRMSE in (2.31) is chosen as 0.4×10^{-4} and the value of parameter σ in (2.23) is chosen to be 4.

2.3.3 Algorithm to implement the method

The algorithm in Algorithm 1 gives a clear understanding of the method proposed in Section 2.3.

Algorithm 1 Switching anisotropic filter.

$u_0 \leftarrow$ Image corrupted by noise and blur.
$\lambda \leftarrow$ Scalar positive value calculated based on (2.19).
Evaluate $u_{\eta\eta}$ by (2.27) and $u_{\xi\xi}$ by (2.28) and $\|\nabla u\|$ by (2.24).
$\epsilon \leftarrow$ small scalar positive value
Take a very small time step Δt, that satisfy the CFL condition defined in (1.21).
$NRRMSE_i \leftarrow 0$
Evaluate $NRRMSE_{i+1}$ using (2.31) for the initial noisy image u_0.
while $|NRRMSE_{i+1} - NRRMSE_i| \geq \epsilon$ **do**. ▷ Iterate till the NRRMSE of successive iterations is less than ϵ
    $NRRMSE_i \leftarrow NRRMSE_{i+1}$. ▷ Assign the current NRRMSE value to the previous one.
    Evaluate for u^{n+1} using (2.30).
    $NRRMSE_{i+1} \leftarrow$ The NRRMSE calculated for the newly computed image u_t^{n+1}, and update λ based on (2.19).
end while

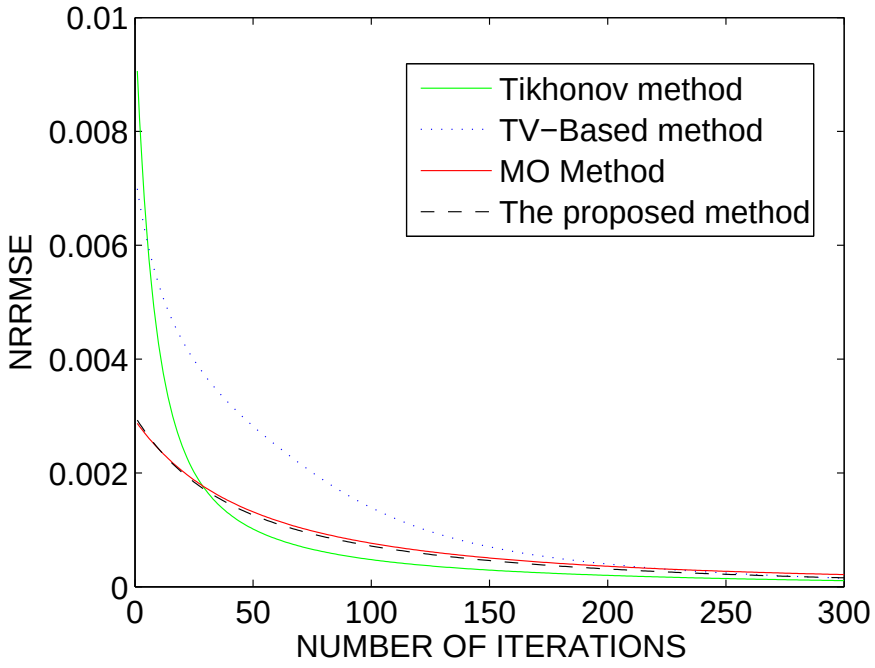

A

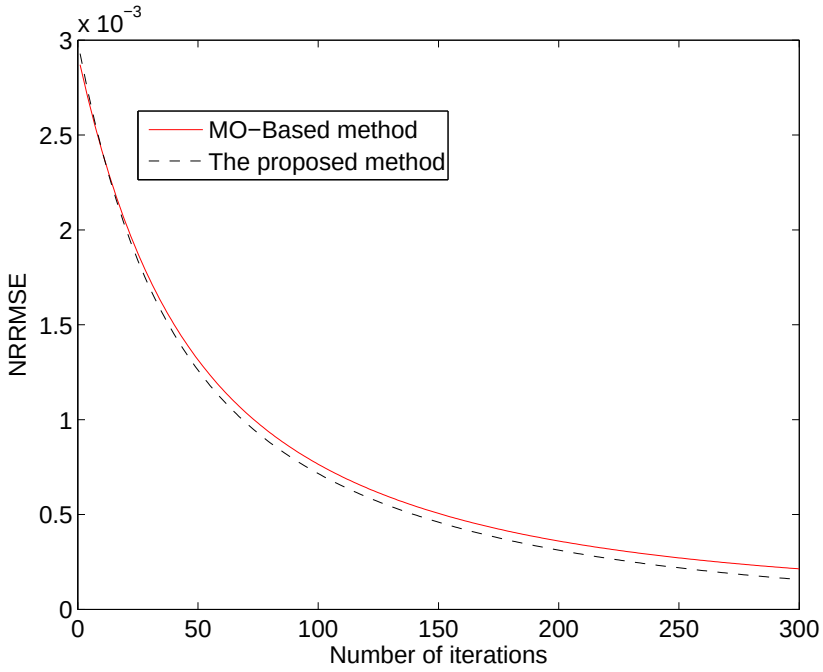

B

Figure 2.1: (A) NRRMSE plotted for different methods for the image "phantom"; (B) NRRMSE plotted for MO-Based and the SAEM against the number of iterations.

2.4 RESULTS AND DISCUSSIONS

We have used standard test images "Lena", "phantom" ,"mri", "hibiscus", "woman" and "boat" to test the performance of various methods existing in the literature and the one proposed in this chapter (SAEM). The images "Lena", "phantom", "mri", "hibiscus", "boat" and "woman" belong to different classes; "Lena" and "woman" are partially textured image with homogeneous intensity regions, "phantom" is a constant intensity image with different constant intensity regions, "mri" and "boat" are partially textured image with abundant gray-level variations and "hibiscus" is a vector valued(color) image. These six test images are chosen to demonstrate the capability of the methods under comparison to handle different kinds of images. Note that, the test images are degraded using a blurring kernel with mean zero and standard deviation σ=4 and a Gaussian white noise (independent of the data), resulting in a noisy image with Signal-to-Noise Ratio (SNR) of 10dB. The regularization parameter λ is fixed as 0.1 for non-iterative methods like FFT-REG and SOB-REG, whereas for iterative regularization methods this parameter is evaluated dynamically (in each iterations) using (2.19). Furthermore, all the test images are normalized in the range [0-1] in all the experiments. We use three qualitative measures Contrast-to-Noise Ratio (CNR) (Gonzalez and Woods 2001), Pratt's Figure of Merit (FOM) (Pratt 1977) and Mean Structural SIMilarity (MSSIM) index (Wang and Bovik 2004) to measure the quality of the filtered images, quantitatively. The time step parameter Δt is evaluated as:$\frac{1}{1+\lambda/\epsilon}$. The parameter ϵ is used to regularize the gradient (to avoid blowing up of the values at the zero gradient areas), the parameter is fixed as 0.04 and the value of parameter c in (2.23) is kept as 1 in all our experiments. However, we have shown the effect of all these parameters on the filtered output by varying their values.

In each experiment, the performance of the SAEM is compared to that of other filters like: FFT regularization filter (FFT-REG) (Bertero and Boccacci 1998), Sobolev regularization filter (SOB-REG) (Bertero and Boccacci 1998), optimal Weiner filter, Tikhonov regularization method (Tikhonov and Arsenin 1977), TV-Regularization model (Rudin et al. 1992) and the model proposed by Marquiana and Osher (MO) (Marquiana and Osher 2000). The performance of each method is quantified perceptually (in figures) and quantitatively (in Tables and Graphs). Here we remark that, since this chapter mainly focuses on iterative regularization methods, the results of non-iterative methods are not explicitly shown under all experimental set-ups. How-

ever, we observe that the performance of the non-iterative methods considered here are considerably inferior to the iterative ones. The results are demonstrated, compared and analyzed in the subsequent sections.

2.4.1 Quality metrics

The statistical measures like CNR, FOM and MSSIM are employed here to measure the quality of reconstruction of various methods under consideration. In general these measures highlight the contrast enhancing and edge and structure preserving capabilities of the filters under consideration. The details of CNR, FOM and SSIM are already discussed in Sections 1.4.4, 1.4.2 and 1.4.3 of Chapter 1, respectively.

2.4.2 Analysis and discussions

Figures 2.2 and 2.3 are the output images after applying different filters in the literature and the one proposed in this chapter on the test images "Lena" and "phantom", respectively. The fact that the SAEM (image in Figures 2.2 I and 2.3 I) well preserves the edges and finer details (while denoising the image), is quite evident from these images. A textured portion from the image "Lena" (after applying various filtering methods) is enlarged and shown in Figure 2.4 for better visibility. From these enlarged portions, we observe that, the capability of the SAEM to retain the finer details and edges is better in comparison to the other methods, whose output is shown in the same figure. We present the response of the SAEM along with the other relevant methods in the literature, when applied to the textured medical image "mri" and the color image "hibiscus" in Figures 2.5 and 2.6, respectively. From these two output images we can arrive at the conclusion that the SAEM can handle textured and color images, the same way it handles the other aforementioned images. Furthermore, the results for partially textured images "woman" and "boat" are provided in Figures 2.7 and 2.8, respectively.

A one dimensional row profile from the image "'Lena" is shown in Figures 2.9 and 2.10. The 200^{th} row is captured from the original, noisy and filtered images. This profile gives a clear understanding of the filtering process. We have plotted three row profiles in each graph in Figures 2.9 and 2.10. The profiles in each graph correspond to the original image shown in red continuous line, the blurred and noisy image is shown as dotted black line and the filtered output shown as an intermediate

dotted blue line. Each graph shown in the figure highlights the output of a specific filtering method used. From these graphs, we infer that the filtering methods like Tikhonov and Sobolev smooths-out the high frequency components corresponding to the edges and finer details. The Tikhonov and Sobolev filters are defined on a space, which does not allow discontinuities in the solutions, and hence the filtered images appear smooth/blurred. However, the noise features are removed effectively by these filters. The other filters, viz. TV, MO and SAEM are defined on a space which allows discontinuities in the solution. Therefore, these filters retain the edges while denoising the images. Among the methods that allow discontinuities in the solution space, the SAEM well preserves the edges and finer details due to the switching behavior of the filter based on the underlying local gradient features. The demonstration in Figure 2.10 C substantiates the above fact.

For analyzing the quantitative measures like CNR, FOM and SSIM, we have used the test image "phantom". The response of the methods, for other test images are similar to that of the image "phantom". Therefore, the resultant images (filtered output images) are not shown explicitly for other test images. Similarly the qualitative measures (discussed above) are tabulated and shown in tables for the test images "Lena", "phantom", "mri" and "hibiscus" at a specific SNR value. The other test images ("boat" and "woman") are found to follow similar characteristics as far as these measures are concerned. In the same manner, the graph showing the variation of the qualitative measures (CNR, FOM and SSIM), for different noise levels (of input images) are demonstrated only for the image "phantom". The result for other test images follow the same pattern as that of the image "phantom".

The CNR for various methods are tabulated in Table 2.1. From the table it is quite evident that the SAEM enhances the contrast better compared to the other existing methods. The CNR is calculated for the images after applying the desired filter till the stopping rule (given in Section 2.3.2) is satisfied. We measured the CNR for the region R1 (in the foreground) taking R2 in the background as shown in Figure 2.11 (A). Similarly the CNR is measured for the region R3 taking R2 in the background. The graph in Figure 2.11 (B) shows the variation of CNR for different methods at different noise variances (for the input image "phantom"). From this graph one can easily make out that the SAEM improves the CNR at various levels of noise variances.

Pratt's FOM measures the edge preserving capability of methods. As mentioned

Table 2.1: The CNR of various methods compared with the SAEM. The SNR of the noisy image: 10 dB.

Images	Noisy	TV	Tikhonov	MO	SAEM
Lena	13.5	12.05	13.6	14.1	16.07
phantom	20.8	33.6	30.7	40.48	66.48
mri	22.1	34.3	29.7	38.9	67.4
hibiscus	20.1	33.8	30.7	41.9	69.4

earlier, Canny edge detector (Canny 1986) is used to localize the edges in the original and reconstructed images, respectively. The parameter (variance) of Canny edge detector is chosen to be 0.1 for our experiments. Table 2.2 shows the numerical results of Pratt's FOM on the filtered images (and the noisy image); which are filtered using various methods in the literature and the SAEM. The values in Table 2.2 are in support of the claim that, the SAEM preserves and enhances the edges as compared to the other methods in the literature. We plot the variation of FOM measured under different noise levels (for the input image), for various methods described in the literature and the SAEM in Figure 2.12. The graph is quite self explanatory, regarding the performance of the SAEM. Further, the result of Canny edge detector on the filtered outputs are shown in Figure 2.13. The output image after applying Canny edge detector on the image filtered with the SAEM, is shown in Figure 2.13 I. In this image, one can observe that the edges are preserved and the noise features are removed well, in comparison to the other filters.

Table 2.2: The FOM of various methods compared with the SAEM . For the images corrupted by SNR 10dB.

Images	Noisy	TV	Tikhonov	MO	SAEM
Lena	0.503	0.410	0.530	0.492	0.582
phantom	0.516	0.449	0.421	0.5254	0.740
mri	0.546	0.519	0.441	0.614	0.751
hibiscus	0.513	0.499	0.411	0.554	0.810

The MSSIM shows the structure preserving capability of the method in hand. The structural similarity index is a key measure to identify the structure preserving capability of the methods. The SSIM values are tabulated in Table 2.3 for different input images filtered with various methods in the literature and the SAEM. It is obvious

from this table, that the SAEM can well preserve the structural details as compared to other methods in the literature. We plot the variation of MSSIM measured under different noise levels for various methods described in the literature and the SAEM in Figure 2.14. This provides a better analysis on the performance of the SAEM.

Table 2.3: The MMSIM of various methods compared with the SAEM. The SNR of the noisy image: 10 dB.

Images	Noisy	TV	Tikhonov	MO	SAEM
Lena	0.669	0.588	0.658	0.652	0.685
phantom	0.656	0.751	0.647	0.698	0.919
mri	0.666	0.821	0.747	0.798	0.891
hibiscus	0.716	0.751	0.672	0.718	0.909

The effect of various parameters in the SAEM in (2.23) on the filtered images are shown in Figure 2.15. We have used three different parameters to control the magnitude of diffusion and regularize the filter. The parameter λ is evaluated adaptively as discussed earlier. The other two parameters c and τ are fixed based on the experimental values. The effect of these parameters on the filtered output is shown in Figure 2.15. The Figure 2.15 A, shows the original image and Figures 2.15 B-D show the outputs for various values of the gradient threshold parameter τ. It is evident from these figures that, the increase in value of τ causes a better smoothing in the homogeneous image areas. The value of τ decides the switching threshold for the filter. If it is quite high then, for the gradient values less than the threshold value, the filter will act as a "Laplacian" and smooths out those gradients. We show the result of the filter for three different threshold values ($\tau = 5, 15$ and 25). The effect of parameter c on the filtered output is shown in Figures 2.15 E-G. The magnitude of diffusion is directly proportional to the value of c. The filtered outputs for three different c values (for $c = 0.2, 0.9$ and 1.5) are shown in Figures 2.15 E-G. The figure with $c = 0.2$ is not denoised properly. Whereas, the output for $c = 1.5$ shows a better denoised image.

From the results demonstrated in terms of visual and quantitative measures, it can be easily verified that the proposed method (SEAM) restores various images with different features at a better way as compared to other relevant methods in the state-of-the-art image restoration.

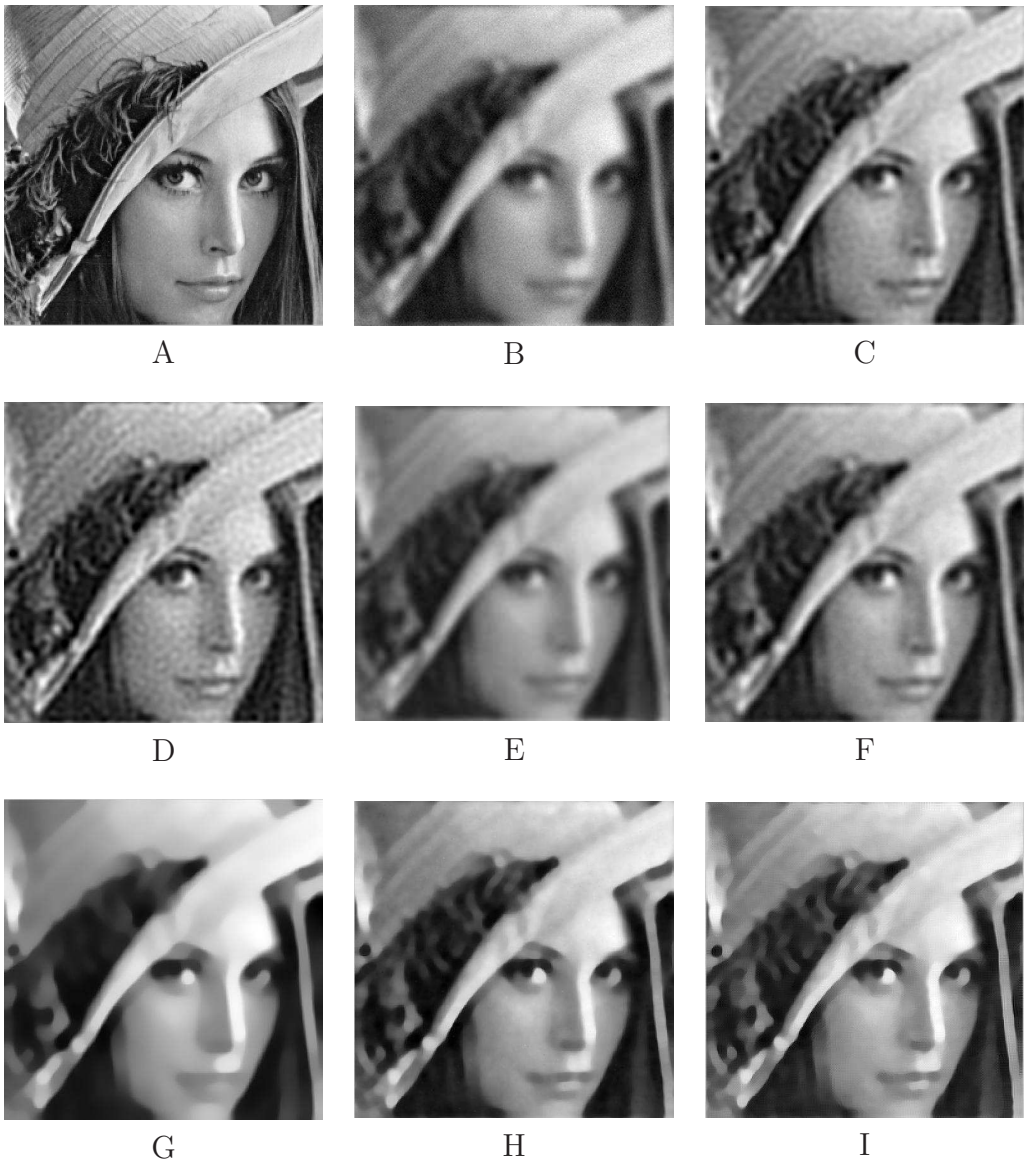

Figure 2.2: Results of various filters applied on the image "Lena":(A) Original image; (B) Blur and noisy image (out of focus blur generated using Gaussian kernel, SNR of noisy image is 10dB); (C) After applying FFT-REG Filter; (D) After applying SOB-REG-Filter; (E) Result of Weiner filter; (F) After applying Tikhonov method; (G) Result of Applying TV Model; (H) Result of MO-Model; (I) Result of the SAEM.

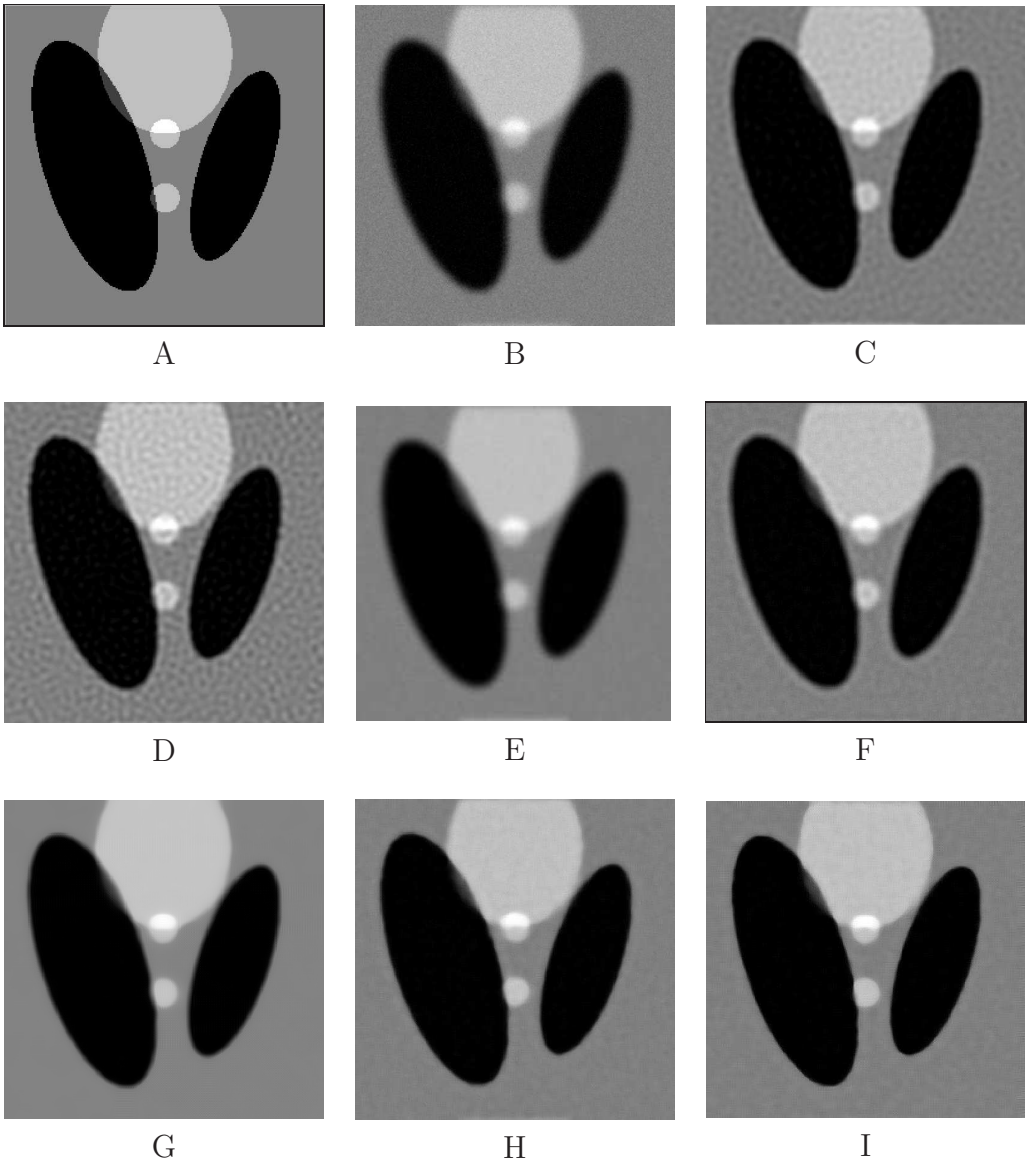

Figure 2.3: Results of various filters applied on the image "phantom":(A) Original image; (B) Blur and noisy image (out of focus blur is generated using Gaussian kernel, SNR of noisy image is 10 dB); (C) After applying FFT-REG Filter; (D) After applying SOB-REG Filter; (E) Result of Weiner filter (F) After applying Tikhonov method; (G) Result of Applying TV Model; (H) Result of MO-Model; (I) Result of the SAEM.

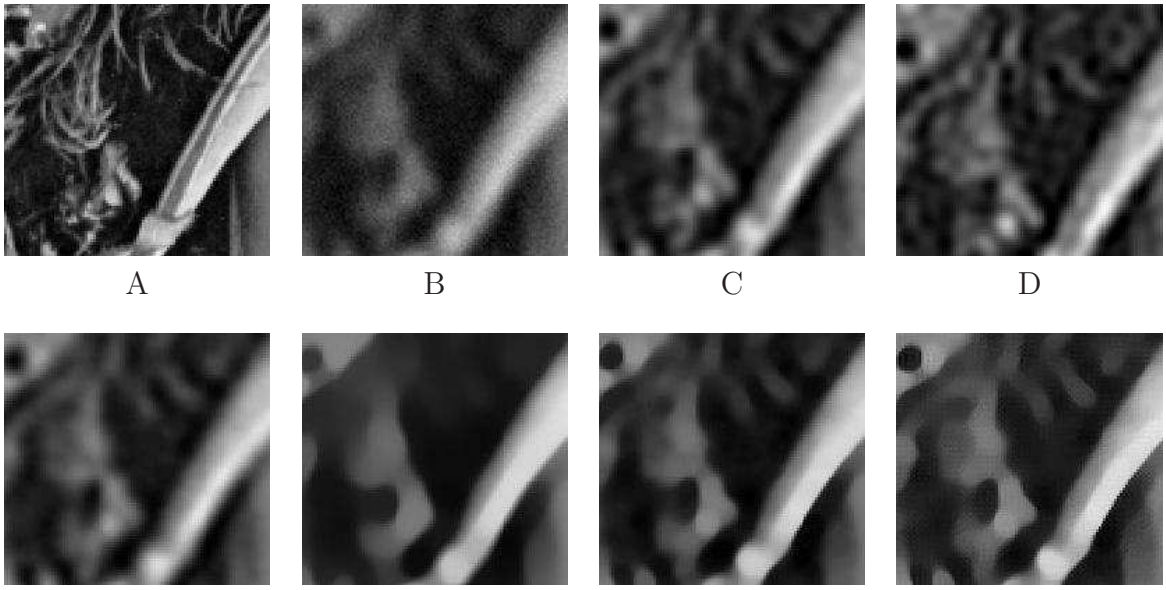

Figure 2.4: A textured portion of the image "Lena" enlarged (for original and filtered images):(A) Original image; (B) Blur and noisy image (out of focus blur generated using Gaussian kernel, SNR of noisy image is 10dB); (C) After applying FFT-REG Filter; (D) After applying SOB-REG-Filter; (E)After applying Tikhonov method; (F) Result of Applying TV Model; (G) Result of MO-Model; (H) Result of the SAEM.

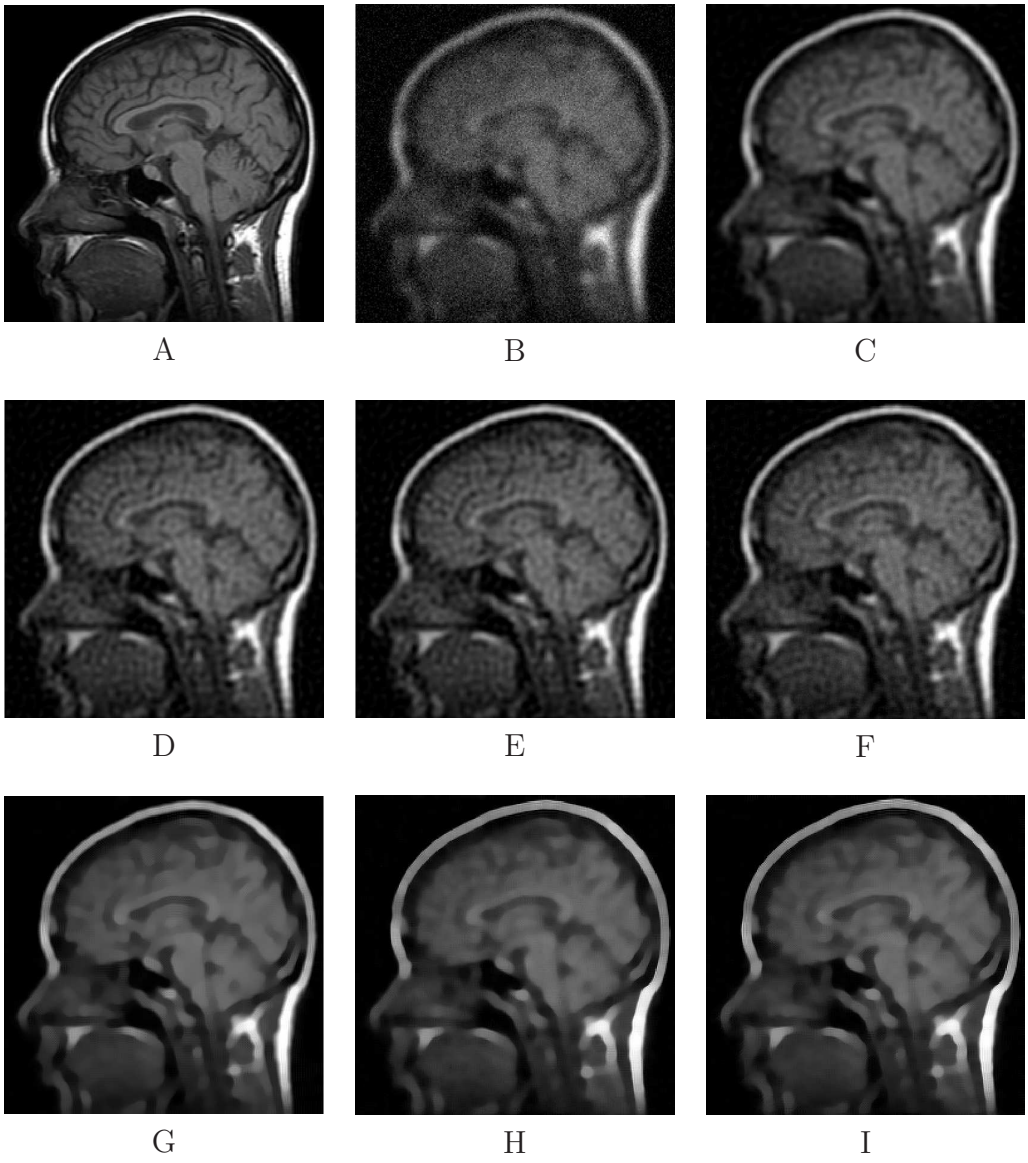

Figure 2.5: Results of various filters applied on the image "mri":(A) Original image; (B) Blur and noisy image (out of focus blur is generated using Gaussian kernel, SNR of noisy image is 10 dB); (C) After applying FFT-REG Filter; (D) After applying SOB-REG Filter; (E) Result of Weiner filter (F) After applying Tikhonov method; (G) Result of Applying TV Model; (H) Result of MO-Model; (I) Result of the SAEM.

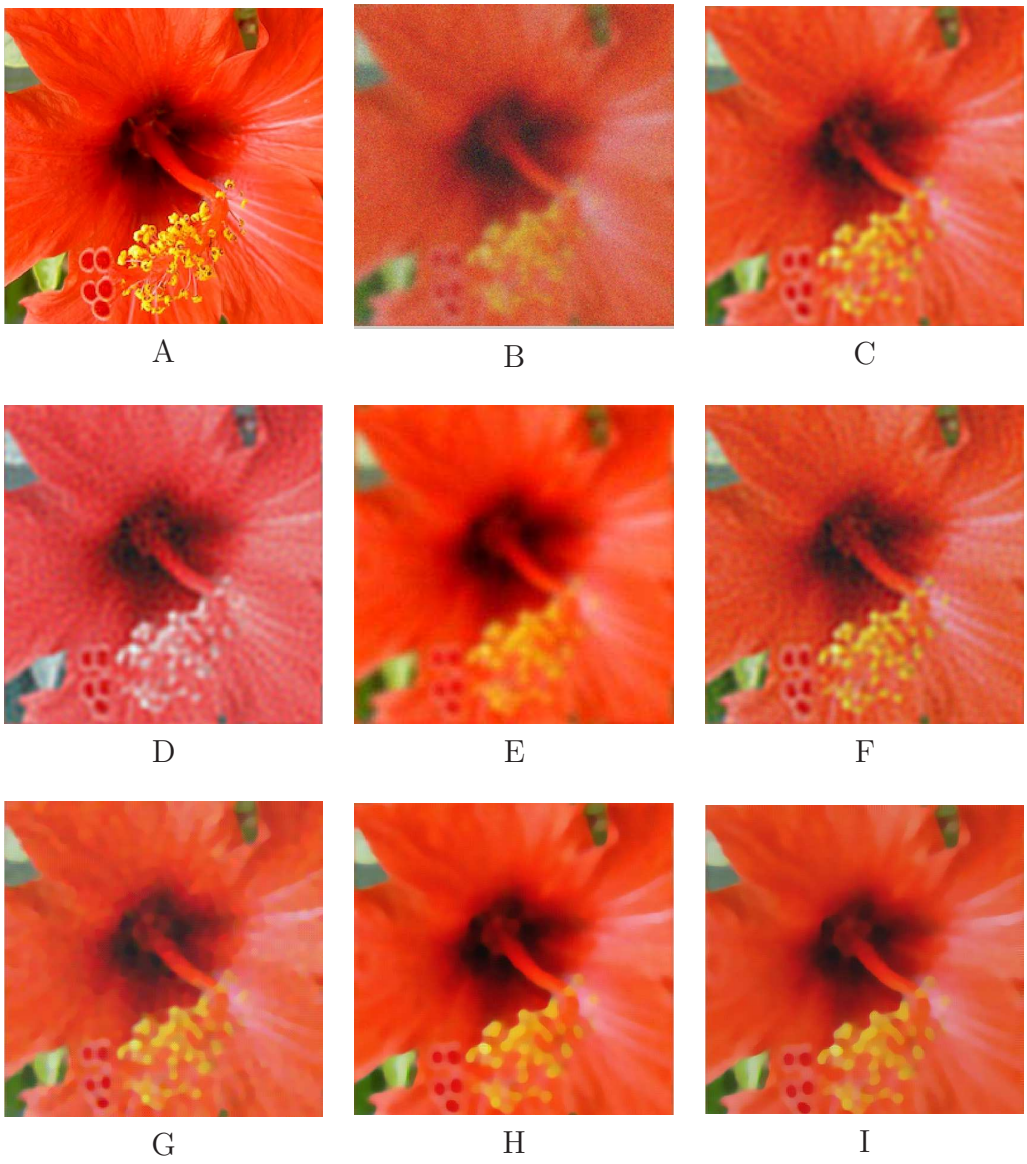

Figure 2.6: Results of various filters applied on the image "hibiscus":(A) Original image; (B) Blur and noisy image (out of focus blur is generated using Gaussian kernel, SNR of noisy image is 10 dB); (C) After applying FFT-REG Filter; (D) After applying SOB-REG Filter; (E) Results of Weiner filter (F) After applying Tikhonov method; (G) Result of Applying TV Model; (H) Result of MO-Model; (I) Result of the SAEM.

Figure 2.7: Results of various filters applied on the image "woman":(A) Original image; (B) Blur and noisy image (out of focus blur generated using Gaussian kernel, SNR of noisy image is 10dB); (C) After applying FFT-REG Filter; (D) After applying SOB-REG-Filter; (E) Result of Weiner filter; (F) After applying Tikhonov method; (G) Result of Applying TV Model; (H) Result of MO-Model; (I) Result of the SAEM.

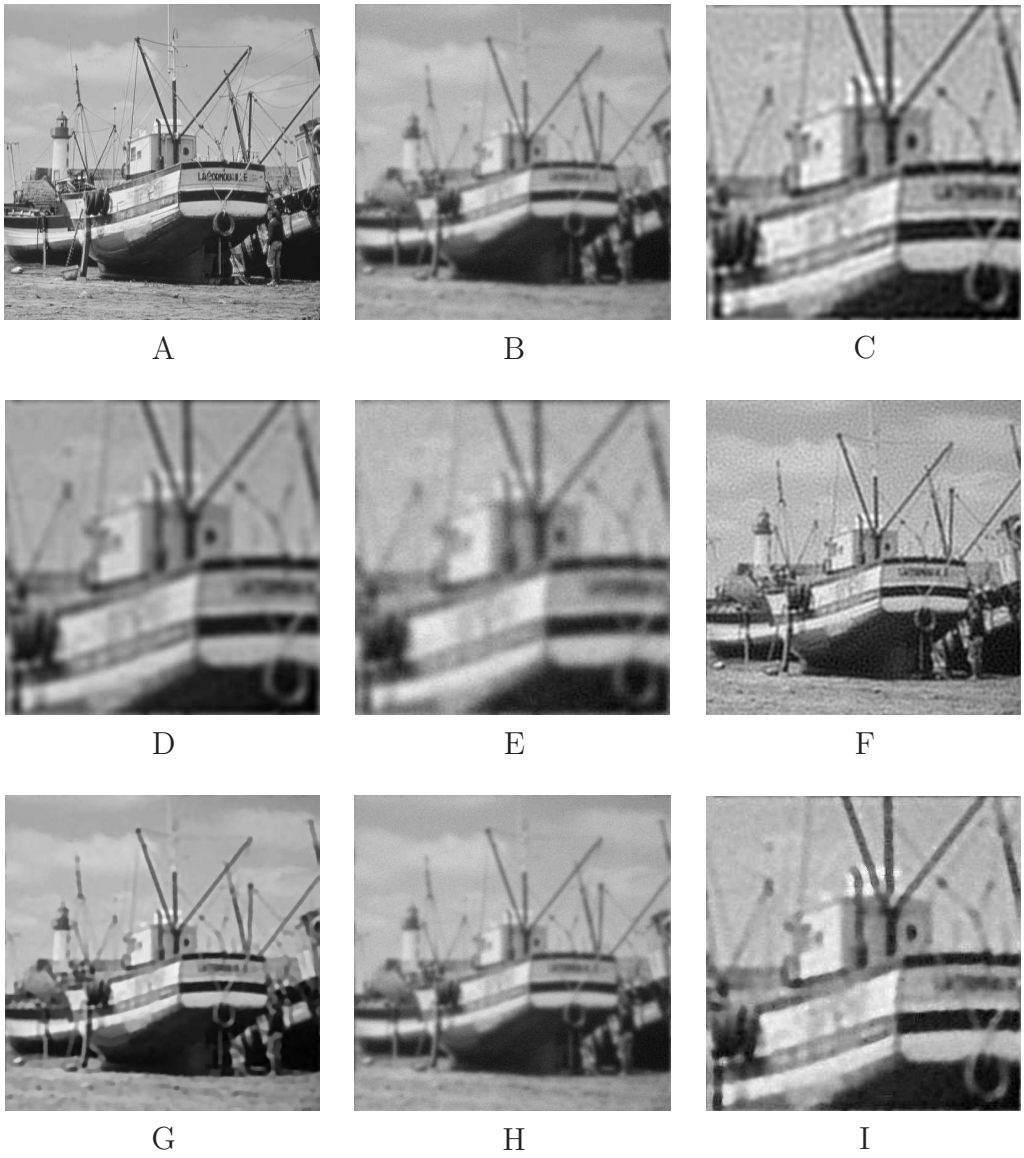

Figure 2.8: Results of various filters applied on the image "boat":(A) Original image; (B) Blur and noisy image (out of focus blur generated using Gaussian kernel, SNR of noisy image is 10dB); (C) After applying FFT-REG Filter; (D) After applying SOB-REG-Filter; (E) Result of Weiner filter; (F) After applying Tikhonov method; (G) Result of Applying TV Model; (H) Result of MO-Model; (I) Result of the SAEM.

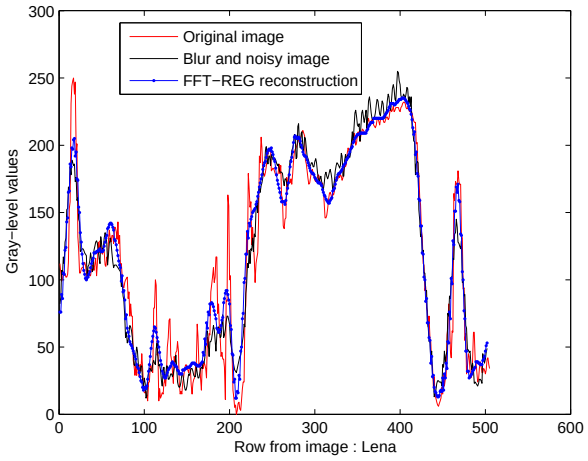

A

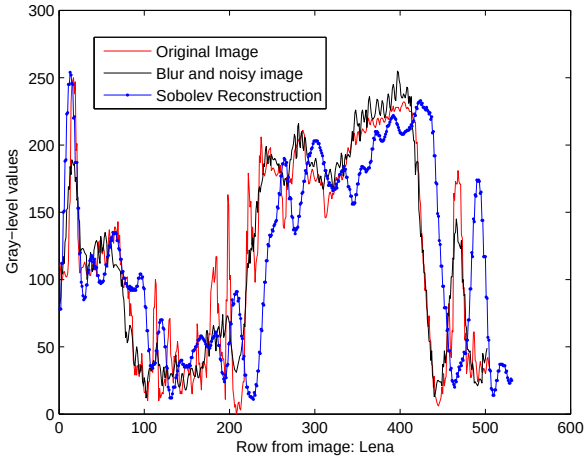

B

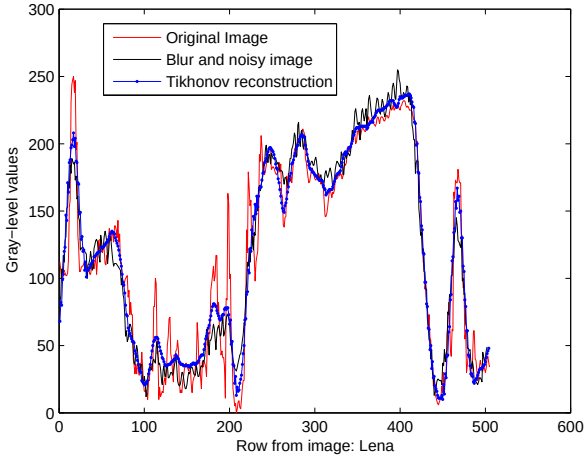

C

Figure 2.9: 1D profile of original, noisy and reconstructed images (after applying): (A) FFT-REG Filter; (B) SOB-REG-Filter (C) Tikhonov Filter

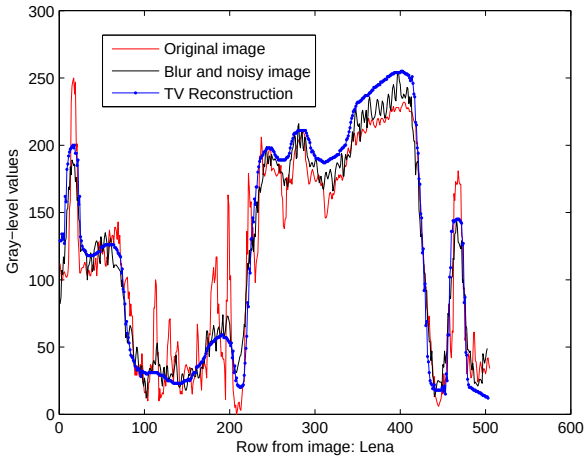

A

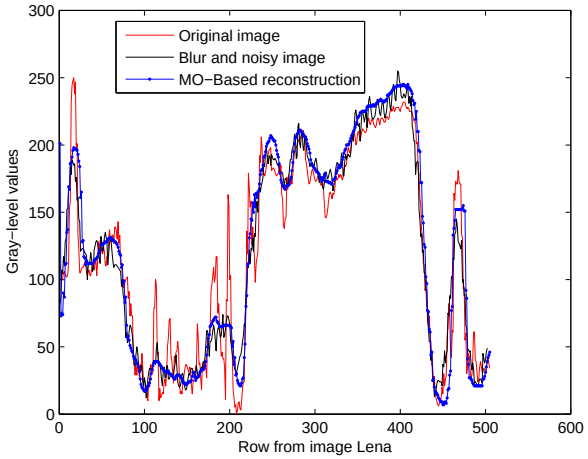

B

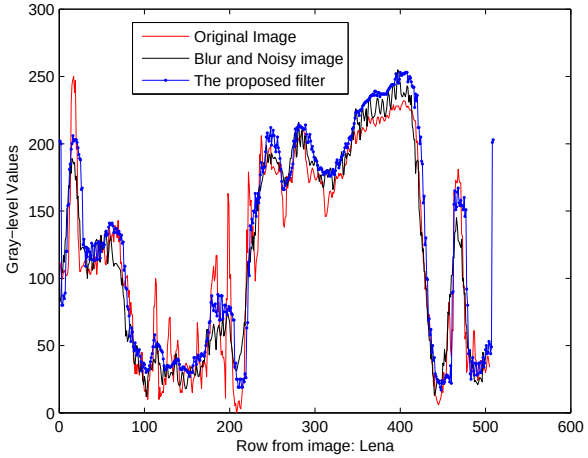

C

Figure 2.10: 1D profile of original (Image "Lena" row:200), noisy and reconstructed images after applying : (A) TV Filter; (B) MO-Filter (C) The proposed filter.

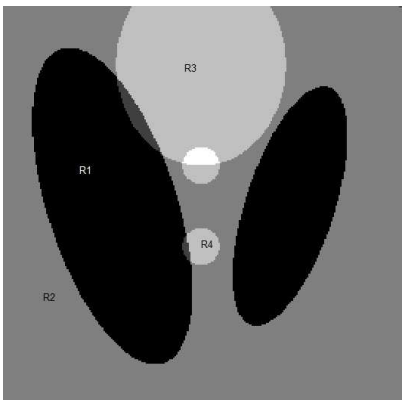

A

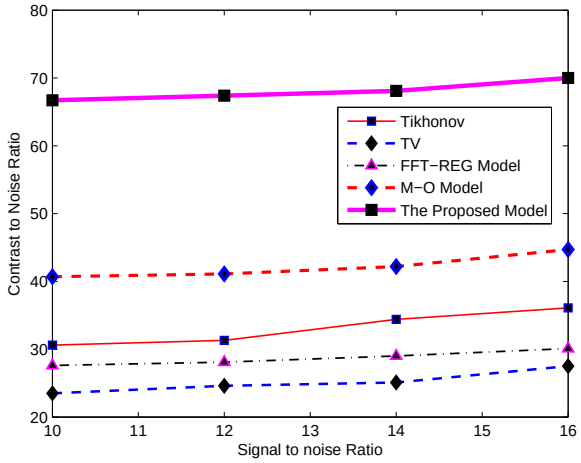

B

Figure 2.11: (A) The regions selected for conducting CNR testing (B) CNR plotted against the SNR for the image "phantom".

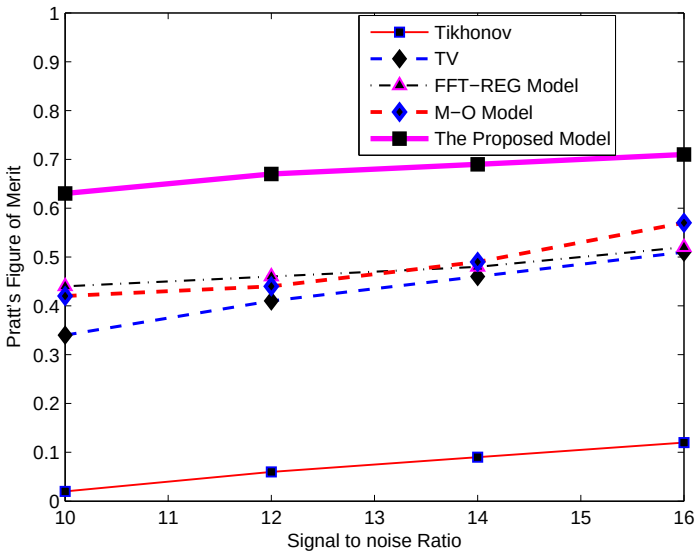

Figure 2.12: Pratt's FOM plotted against SNR for the image "phantom".

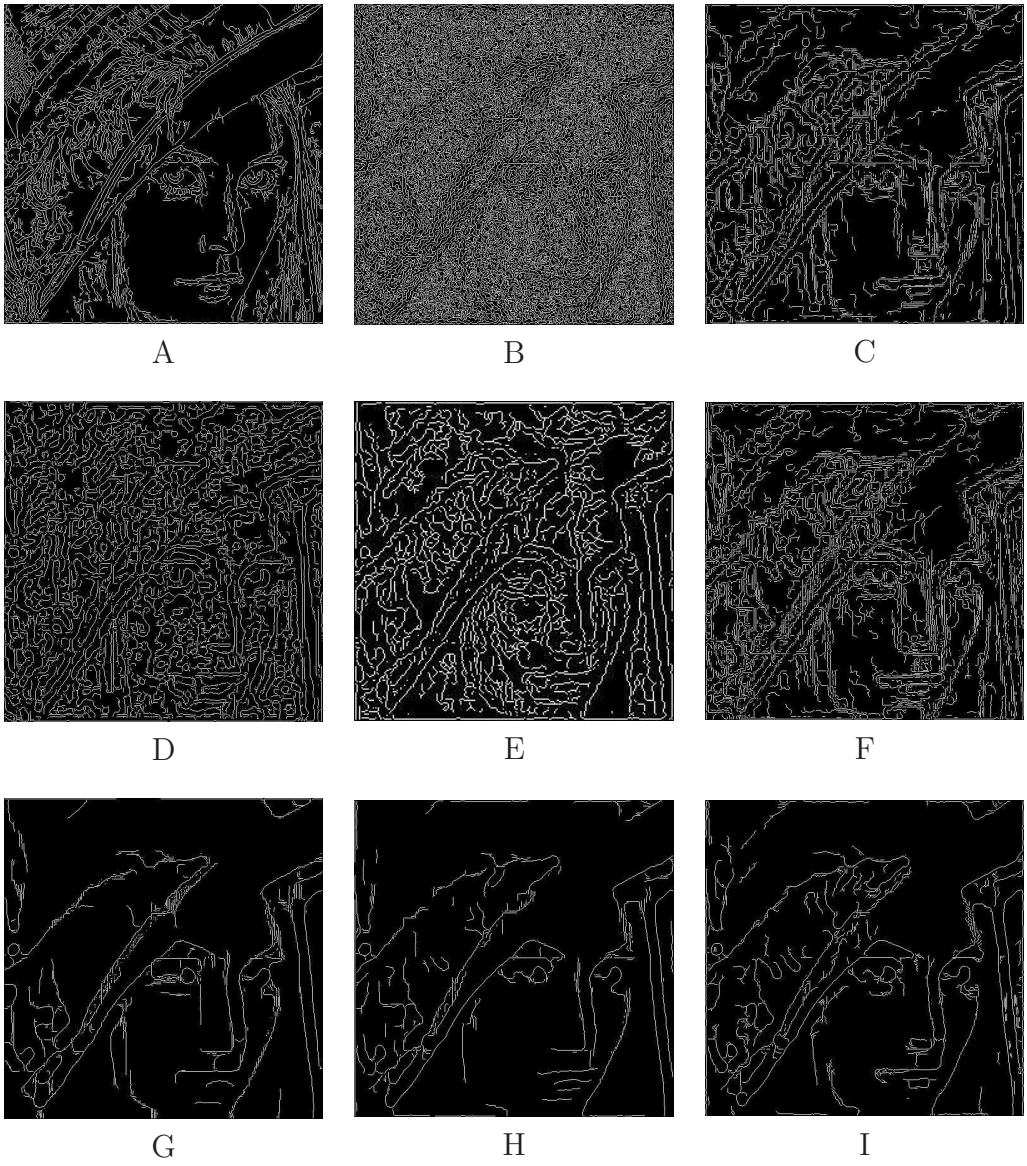

Figure 2.13: The result of CANNY edge detector applied on the image "Lena" (filtered using different methods):(A) Original image; (B) Blur and noisy image (out of focus blur generated using Gaussian kernel, SNR of noisy image is 10dB); (C) After applying FFT-REG Filter; (D) After applying SOB-REG-Filter; (E) Result of Weiner filter; (F) After applying Tikhonov method; (G) Result of Applying TV Model; (H) Result of MO-Model; (I) Result of the SAEM.

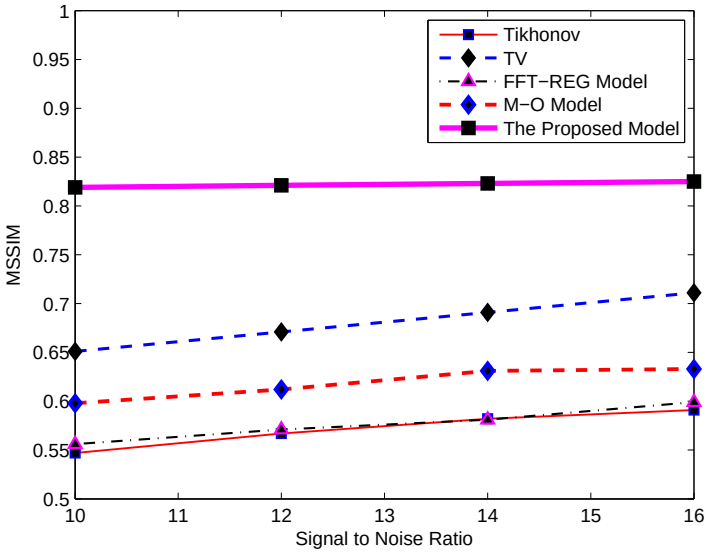

Figure 2.14: MSSIM plotted against SNR for the image "phantom".

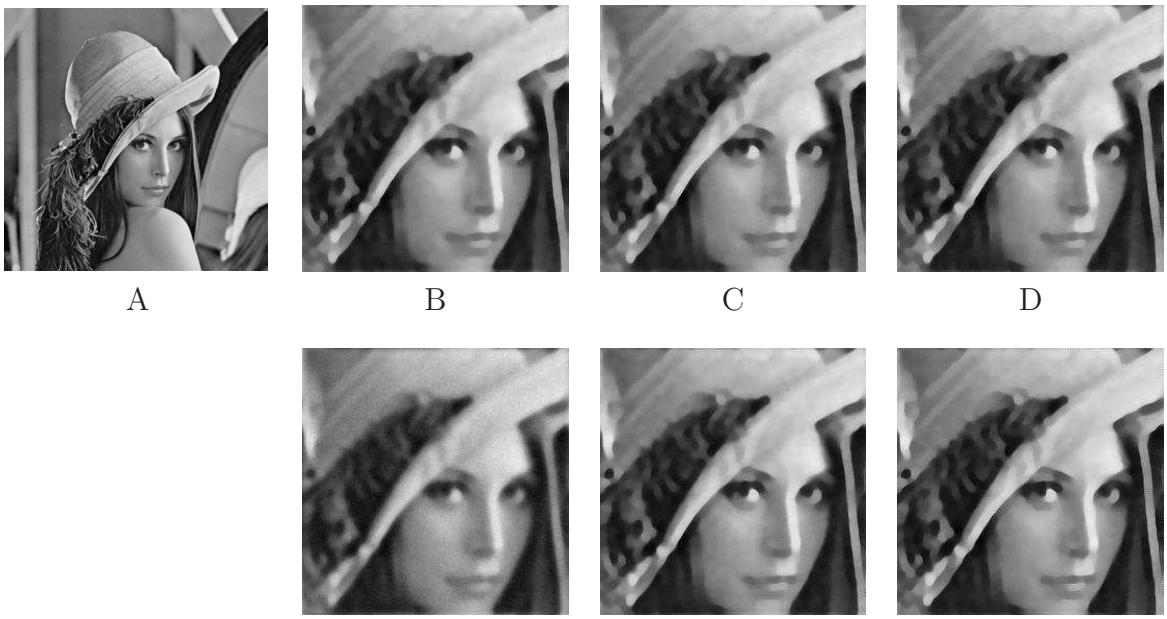

Figure 2.15: SAEM applied on image "Lena" with various values for the parameters: (A) The original uncorrupted image; (B, C and D) shows the output images for three different values for the threshold parameter $\tau = 5$, $\tau = 15$, $\tau = 25$, respectively; (E, F and G) shows the output images for three different values for the parameter $c = 0.2$, $c = 0.9$, $c = 1.5$, respectively.

Chapter 3

CURVATURE DRIVEN IMAGE ENHANCEMENT

3.1 INTRODUCTION

Image enhancement demands a special attention in the day-today imaging activities. Due to the overwhelming demand for the processing of images captured under poor conditions, image enhancement remains as an unavoidable pre-processing step. In Chapter 1, we had introduced the denoising and enhancing capabilities of the non-linear second-order diffusion filters, which are parabolic PDE's. The enhancing capability as a consequence of backward diffusion (in Perona-Malik filter) makes it less preferable due to the unstable nature of the process in many practical situations. This unstable process (the backward diffusion) leads to a non-unique solution (Hollig 1983) and thereby directing to an undesired result.

In many practical applications the images are degraded by the devise artifacts, which causes blur (out-of-focus or motion) in the captured images. In such cases, the enhancement of the edges and the other finer details would be necessary to justify a proper image reconstruction. A general mathematical image degradation model was discussed in (1.1). Assuming the linearity and shift-invariance of the operator in (1.1), this operator can be considered as a convolution operator, which is generally a blurring operator causing an out-of focus blur in the degraded image. Hence, the image enhancement or reconstruction aims at recovering the original image from the observed one, assuming the operator to be linear and noise as independent of data. In this model the imaging system artifacts are assumed to cause an out-of-focus-blur

in the sensed image. Therefore, deblurring becomes a trivial process. The deblurring can be observed as an inverse operation of convolution (which causes the blurring), consequently the deblurring process becomes a deconvolution operation.

Shock filters were introduced in the literature to enhance the image edges and other detailed features without causing any theoretical instabilities (Osher and Rudin 1990). These filters can be approximated to deconvolution filters, which can restore the images from the blurred ones. These filters belong to a class of hyperbolic PDEs, which never results an inverse diffusion. Merely using shock filters may not serve the purpose of image enhancement due to the fact that, in most of the practical imaging applications, the images are corrupted by noise as well. Hence, these filters enhance the noise along with the edges, where they tend to give a shock. Another notable achievement in this direction was the introduction of shock filters coupled with diffusion, see Alvarez and Mazorra (1994) and Gilboa et al. (2002). These filters can denoise images, while preserving and enhancing some of the semantically important image features. But most shock filters that couple a diffusion term (which are proposed in the literature), use one of the variations of Mean Curvature Motion (MCM) (Marquiana and Osher 2000) as the diffusion term. MCM based diffusion eventually results in smoothening of the features with non-zero mean curvature values.

All these facts motivate in proposing an enhancing filter with a curvature driven diffusion term, which can reconstruct the images from the blurred and noisy ones. Among the curvature driven techniques, Gauss curvature driven technique is more suitable due to its capability to preserve structures with non-zero mean curvature values. Therefore, in this chapter we propose to use a shock filter coupled with a Gauss curvature driven diffusion term to enhance the images. The noise will always have a non-zero Gauss curvature value, hence it gets removed in the evolution process effectively. Moreover, some structures with low gradient magnitudes, that are not well preserved by other curvature-based diffusion processes are preserved by the Gauss curvature flow and enhanced by shock component in the proposed filter. The filter is also equipped with a time dependent function in the shock term, which controls the extent of shock and diffusion during various stages of the evolution process. The details are provided in the following sections. The experimental results are provided in section 3.4 and compared with the most relevant state-of-the-art image enhancement methods.

Rest of the chapter is organized in three sections. Section 3.2 explains the history of

curvature driven diffusion methods, its mathematical formulations and the advantages of using them for denoising. In section 3.3 the details of the proposed curvature driven enhancement and its numerical implementations are highlighted. The results and discussions of the curvature driven enhancement methods are done in section 3.4.

3.2 CURVATURE DRIVEN DIFFUSION METHODS AND SHOCK FILTERS

The non-stable nature of the backward-diffusion process in Perona and Malik (1990) makes it not much suited for image enhancement. There are many alternative solutions suggested by researchers to address the setbacks of Perona-Malik filter, see Weickert (1997), Catte et al. (1992) and Alvarez et al. (1992) for details. Curvature based and curvature-driven methods were also fine-tuned to address the above mentioned drawback.

3.2.1 Curvature driven methods

Use of geometric properties of the image, incorporated in PDEs for noise removal has captured the attention of researchers recently, details can be found in Lee and Seo (2005) and Chan et al. (2002). Most commonly used geometric features are curvature of the level curve and mean curvature of the surface. Note that, here image is considered as a two-dimensional plane in the three-dimensional space. In all these schemes, that use the local geometric features for noise removal, noise is considered to have high mean curvature and are effectively removed by the mean curvature flow. However, many important image features having non zero local mean curvatures also get removed. Use of curvature terms as a conductance function for driving the diffusion was first proposed for image inpainting by Chan et al. (2002). The same can be extended to the denoising process as well. A curvature driven min/max flow method was also introduced for image denoising, refer Malladi et al. (1996) for details. But the mean curvature flow does not fit to be a good driving function in many practical situations, where the images have curvy edges, corners etc. For these features, the mean curvature value is non-zero. Since, the speed of diffusion is controlled by the magnitude of mean curvature value, the diffusion adversely affects these features.

Gauss curvature was introduced to image denoising by Lee and Seo (2005), for

addressing the drawbacks (that are already mentioned above) of the mean curvature driven diffusion method. Gauss curvature being the product of principal curvatures, we recall from Chapter 1 that, Gauss curvature is zero at a point, where any of the principal curvatures is zero. Whereas the mean curvature is the mean of the principal curvatures, which becomes zero when all of the principal curvatures are zero. So, the Gauss curvature can be used as a conductance term in the diffusion process for preserving curvy edges, corners and other features with non-zero mean curvature, we refer to Lee and Seo (2005) for details. Since the Gauss curvature function is a non-decreasing monotone function, the evolution will never result in a backward diffusion, which is ill-posed in nature. Hence, using the curvature driven diffusion term in place of the coefficient of diffusion, the flux function will be monotonic in behavior and the solution will be unique, therefore, the problem will be well-posed. From the above facts one can easily infer that, the curvature driven diffusion will never enhance the image features because of the monotonic nature of the flux function. As mentioned earlier in this chapter, many of the images that are being commonly processed, demands an enhancement in addition to the denoising. In such scenarios curvature-driven diffusion alone may not serve the purpose of a credible image enhancement. Therefore, hyperbolic filters are introduced in the literature to enhance the images in a more stable manner. Such stable enhancing filters are elaborated in the following section.

3.2.2 Shock filters

Shock filters are used widely for image enhancement because these filters are stable in nature (Osher and Rudin 1990). The following properties of the filter makes it a good choice for image enhancement.

1. The shocks are developed at the inflection points (second derivatives) while the local extrema remain unchanged in each evolution.

2. No new local extrema is introduced as a part of evolution and the steady state solution will have discontinuities at the inflection points.

These properties approximate this filter to a deconvolution filter, which can deblur the images, refer Gilboa et al. (2002) for details.

The idea of shock filter is based on hyperbolic equations theory. For 1D signals or 2D images, $\phi(u, \nabla u, \nabla^2 u) = \zeta u_x$, where ζ is a constant, u_x denotes the first derivative

of u along the direction x, ∇u and $\nabla^2 u$ denote the gradient and "Laplacian" of the image u, respectively. For any general image processing problem, ϕ denotes the function that represents the rate of change of the image function $\frac{du}{dt}$. Hence, the solution for the equation $\frac{du}{dt} = \phi(u, \nabla u, \nabla^2 u)$ under the boundary condition in (1.30) and the initial condition in (1.31) is $u(x,t) = u_0(x + at)$, where a is the speed of translation of the solution. The idea behind the shock filter is to make the speed of translation depend on the image structure u_{xx} in case of 1D signals and $u_{\eta\eta}$ in case of 2D images. Here $\eta = \nabla u / \|\nabla u\|$ denotes the direction along the gradient ∇u. Now, replacing the speed of translation a with $-sign(u_{\eta\eta})$, for 2D images we obtain the expression of the "classical" shock filter in Rudin et al. (1992):

$$u_t = -sign(u_{\eta\eta})\|\nabla u\|, \tag{3.1}$$

where u_t stands for $\frac{\partial u}{\partial t}$, $\|.\|$ denotes the Euclidean norm and $sign$ function is defined as:

$$sign(x) = \begin{cases} -1 & \text{if } x < 0 \\ 0 & \text{if } x = 0 \\ +1 & \text{if } x > 0 \end{cases} . \tag{3.2}$$

All the $sign$ functions used throughout this thesis are as defined above. One of the major drawbacks of the classical shock filter is its inefficiency to distinguish the inflection points caused due to the noise from that due to the edges. Eventually the classical shock filter in (3.1) enhances the noise along with the edges.

3.2.2.1 Shock coupled diffusion filters

Many improvements were suggested for "classical" shock filter in (3.1), we refer to Alvarez and Mazorra (1994), Brockett and Maragos (1992) and Coulon and Arridge (2000) for details. The *Laplacian of Gaussian* (LOG) as a shock term is one of such improvements; but the smoothing capacity of the filter is tightly coupled with the spread of the Gaussian kernel σ. This filter tends to ignore the noise features smaller than σ and if σ is large, then the filter will smooth-out many of the inflection points that belong to the images along with the noise. This defect was addressed adequately by Alvarez and Mazorra (1994). They proposed to use a curvature based diffusion along with the shock term to suppress the noise enhancing property of the "classical" shock filter in (3.1). The evolution equation for the filter considered in

Alvarez and Mazorra (1994) is:

$$u_t = -sign(G_\sigma * u_{\eta\eta})\|\nabla u\| + \lambda u_{\xi\xi}, \tag{3.3}$$

here λ denotes the control parameter, which is a positive scalar value that controls the magnitude of diffusion, $G_\sigma * u$ denotes the Gaussian (with standard deviation σ) convolved version of the image u, η is the direction along the gradient and ξ is the direction perpendicular to the gradient. This anisotropic filter acts like, a "shock" filter in the direction of gradient and a diffusion filter in the direction perpendicular to the gradient. The term $u_t = u_{\xi\xi}$ denotes Mean Curvature Motion (MCM). Borrowing the concepts from differential geometry one can define MCM as:

$$u_{\xi\xi} = \|\nabla u\| div\left(\frac{\nabla u}{\|\nabla u\|}\right), \tag{3.4}$$

we refer to Marquiana and Osher (2000) for details. In MCM each of the level curves in the image move in the direction normal to it, at a speed proportional to their mean curvature values.

3.2.3 Curvature-driven diffusion

We recall from subsection 1.3.1.1 that, the curvature driven diffusion controls the speed of diffusion process based on the curvature at any point and commonly used curvatures are the curvature of the level curve and mean curvature of the surface. The mean curvature is defined in (1.56). The mean curvature used as a conductance term in diffusion, namely Mean Curvature Driven Diffusion (MCDD) was proposed for image inpainting by Chan et al. (2002). This method is mathematically modeled as:

$$\frac{\partial u}{\partial t} = \nabla.(\chi(M)\nabla u) \tag{3.5}$$

where M is the mean curvature, defined in terms of finite central difference scheme as:

$$M = \frac{u_x^2 u_{yy} - 2u_x u_y u_{xy} + u_y^2 u_{xx}}{1 + u_x^2 + u_y^2}, \tag{3.6}$$

here $u_x = \frac{\partial u}{\partial x}$, $u_y = \frac{\partial u}{\partial y}$, $u_{xx} = \frac{\partial^2 u}{\partial x^2}$, $u_{xy} = \frac{\partial^2 u}{\partial x \partial y}$, $u_{yy} = \frac{\partial^2 u}{\partial y^2}$ and $\chi(.)$ is a monotonically increasing function of mean curvature M. Other symbols are as in (1.28).

One of remarkable features of mean curvature flow is, it eventually results in

smoothing of all the features at a speed proportional to their mean curvatures and further results in shrinking the level-lines to circular points and vanish in a finite time. This property makes this method non-suitable in many practical scenarios, because the images may have structures like curvy edges corners etc., with non-zero mean curvature values. These structures will eventually fade-out at a speed proportional to their mean curvatures.

It was proposed in Lee and Seo (2005) to use Gauss curvature instead of Mean curvature for driving the diffusion process. A notable improvement of Gauss curvature over the mean curvature is, its ability to preserve structures having non zero mean curvature. This is due to the property that: the Gauss curvature is the product of principal curvatures and defined as (1.57). The Gauss curvature driven diffusion formulated by Lee and Seo (2005) is read as:

$$\frac{\partial u}{\partial t} = \nabla.\left(\chi(G)\nabla u\right), \tag{3.7}$$

where G is the Gauss curvature at surface $z = u(x, y)$ and χ is a monotonically increasing function of G. Here G is defined as:

$$G = \frac{u_{xx}u_{yy} - u_{xy}^2}{(1 + u_x^2 + u_y^2)^2}. \tag{3.8}$$

Further, note that $\chi : \mathbb{R} \to \{\mathbb{R}^+\} \cup \{0\}$ is a non-negative real valued function. The test for critical point can be done based on the numerator of the expression in (3.8). Let $D = u_{xx}u_{yy} - u_{xy}^2$, if $D < 0$ then, the image surface has a saddle point. If $D > 0$ and $u_{xx} > 0$ then, it has a local maximum and if $D > 0$ and $u_{xx} < 0$ then, a local minimum exists. The conductance function $\chi(.)$ controls the speed of diffusion process. At the point where Gauss curvature value is zero the function returns a value zero and consequently the diffusion stops, ultimately preserving those structures. This diffusion process is named as Gauss Curvature Driven Diffusion (GCDD). In the case of noise; the Gauss curvature will have non-zero value because none of the principal curvatures will be zero. This results in smoothing-out the noise present in the images.

A fourth-order Gauss curvature driven diffusion method was proposed for image denoising. In this work we proposed a fourth-order diffusion filter, which uses a function of Gauss curvature as the conductance term to control the magnitude of diffusion. As already mentioned in Chapter 1, the fourth-order PDE performs a planar

approximation of the observed image. And this provides a good natural appearance to the filtered output image. The Gauss curvature based conductance term preserves curvy edges, ramps and corners. The formulation of the filter considered is:

$$\frac{\partial u}{\partial t} = -\nabla^2 \left(\chi(G) \nabla^2 u(x,y) \right), \tag{3.9}$$

where G is defined in (3.8). We choose the function $\chi(x) = \|x\|/max(\|x(i,j)\|), \forall_{i,j}$, as the conductance term. This method is a fourth-order generalization of the second-order method described in Lee and Seo (2005). This filter can preserve the curved edges and corners, while denoising images and does not result in a *staircase* effect caused due to the piece-wise approximation of the image. However, this fourth-order filter doesn't enhance the edges. Moreover, in the fourth-order evolution the image features gets slightly blurred [1].

Though, the curvature driven diffusion with Gauss curvature as the conductance term (as discussed above) can remove noise effectively, it lacks the ability to enhance the edges because the curvature driven diffusion in general hardly results in an inverse diffusion. The conductance function (in this case) is an increasing function, therefore, the flux function will be monotonically increasing and this will forbid an inverse diffusion. In many practical applications the images need to be enhanced along with the noise removal. Therefore, a shock coupled Gauss curvature driven diffusion filter is proposed in the next section for enhancing the image features while denoising them effectively.

3.3 GAUSS CURVATURE DRIVEN IMAGE ENHANCEMENT (GCDIE)

Although, the filter in (3.3), denoises the images, while giving a shock to the edges present in the images, it fails to stop the diffusion process on the edges. This causes a smoothing of edges and finer details along with the noise. Note that, the diffusion term in (3.3) is MCM as defined in (1.55). As discussed earlier, in MCM each of the level-lines in the image try to evolve continuously and shrink to a point. Furthermore, the convex level lines remain convex during the evolution process and non-convex lines

[1] As the order of PDE increases the smoothness in the filtered output also increases. Since, the order reflects the extend of continuity which in fact reflects the smoothness in the image.

become convex after finite number of evolutions. Hence, it is quite natural to couple a curvature driven diffusion term along with the shock term to control the magnitude of diffusion based on the underlying image features. Here, we propose to replace the MCM term in (3.3) with a GCDD term in (3.7), which stops the evolution of level curves at the places having zero Gauss curvature values. The shock term in the filter will enhance the edge features making them sharper. The shock coupled diffusion filter given in (3.3) can be reformulated with proposed modification as:

$$u_t = -\frac{2}{\pi} arctan(G_\sigma * u_{\eta\eta} p(t)) \|\nabla u\| + \lambda c \nabla . \left(\chi(G) \nabla u\right). \tag{3.10}$$

The *arctan* function is a smoothly varying "soft *sign* function" which gives a more natural appearance to the enhanced image (cf. Gilboa et al. (2002)), therefore we use this function instead of the *sign* function in (3.3). The *sign* function defined in (3.2) is a discontinuous function whereas the *arctan* function is a continuously varying function in the open interval $(-\pi/2,+\pi/2)$ for the real input values. Therefore, the *arctan* function behaves smoothly for the input quantity $G_\sigma * u_{\eta\eta} p(t)$, which is real. The shock component present in filter (3.10) is the product of *arctan* of the Gaussian smoothed version of $u_{\eta\eta}$ and the magnitude of the gradient image. Therefore, the *arctan* function will return smaller values (close to zero) for the features with small $G_\sigma * u_{\eta\eta} p(t)$ values and a value close to one for the features with high values of $G_\sigma * u_{\eta\eta} p(t)$. Hence, the image regions with low gradient magnitude (homogeneous areas) will have less response to the shock term as compared to the high gradient areas (edges and finer components). This property of the filter results in an enhancement of edges in the image. The magnitude of diffusion purely depends on the Gauss curvature value, thus this filter retains the features even with non-zero mean curvature values. Here c is a scalar constant parameter that controls the magnitude of diffusion. The term G_σ denotes the Gaussian convolved version of the image u as defined in (1.25).

Here $p : \mathbb{R}^+ \to (0, 1]$ is a non-decreasing function of time defined as:

$$p(t) = \begin{cases} n \times \Delta t & \text{if } n \times \Delta t < 0.5 \\ 1 & \text{otherwise.} \end{cases} \tag{3.11}$$

where $n = 1, 2, 3...$, is the iteration number and Δt is the time step. Note that the the function $p(t)$ inside the shock term is to control the extend of shock and diffusion during the early phases of evolution. When $p(t)$ is small then the contribution of shock

will be minimum whereas the diffusion will be prominent. In other words during the early phases of evolution the noise will be dominant hence, the application of shock term helps only to enhance noise inflection points (making the images more noisy). This problem is addressed to an extent by the inclusion of a time dependent function in the shock term, here we use a non-decreasing piece-wise linear function as defined in (3.11). Incorporating this function of time with the shock term can considerably reduce the effect of shock during the initial stages of evolution. The function $p(.)$ returns small values much less than one ($<< 1$) during the initial stages of evolution (iteration), making magnitude of the shock very less. Therefore, the filter acts like a normal anisotropic diffusion filter. After a finite number of iterations the function $p(.)$ always returns a value '1'. Thereafter, the filter behaves like a shock coupled diffusion filter. The parameter λ is a scalar parameter, which is positive and controls the magnitude of diffusion and shock (based on the image features). The parameter λ is evaluated and updated in each iteration with the following expression:

$$\lambda = \frac{\int_\Omega \frac{2}{\pi} arctan(G_\sigma * u_{\eta\eta} p(t)) \|\nabla u\| dxdy}{\int_\Omega c\nabla . (\chi(G)\nabla u)\, dxdy}. \tag{3.12}$$

The above expression is obtained by re-arranging the terms in (3.10) (at the steady state) and integrating over the image domain.

All other terms in (3.10) are as defined in (3.3) and (3.7). The filter in (3.10) does not introduce any local extrema points and the total variation is not increasing, hence over and under-shoots never occurs in these filters. Furthermore, the shock component is hyperbolic hence the solution will be stable (Osher and Rudin 1990). The function $\chi(G)$ (in the diffusion component) is a monotonically increasing function and therefore, the flux function $(\chi(G)\nabla u)$ will be monotonically increasing and therefore an inverse diffusion does not happen.

3.3.1 Numerical implementations

We use the explicit Euler numerical schemes for solving the PDEs given in (3.10). Since the *shock* filters are hyperbolic PDEs, the usual central difference scheme may not help in getting a proper result. This scheme will be highly unstable and may not converge. So we use the *upwind* scheme proposed in Osher and Sethian (1988), see Section 2.3.1 for details. The scale space parameter h is assumed to be 1 and Δt is

the time step. The detailed formulation of hyperbolic term can be found in Chapter 2, Section 2.3.1. With the help of finite central difference schemes discussed in Section 2.3.1 one can discretize (3.10) as follows:

$$u^{n+1} = u^n - \Delta t \times \frac{2}{\pi} arctan\left(G_\sigma * \left(\frac{u^n_{xx}|u^n_x|^2 + 2u^n_{xy}u^n_x u^n_y + u^n_{yy}|u^n_y|^2}{1 + |u^n_x|^2 + |u^n_y|^2}\right) p(t)\right) \times \sqrt{D_x^2 + D_y^2} + \Delta t \times \lambda \nabla . \left(\chi(G)\nabla u^n(x,y)\right). \tag{3.13}$$

The term G_σ is the Gaussian convolved version of the image u, as defined in (1.25). The expression $\nabla . \left(\chi(G)\nabla u(x,y)\right)$ is discretized using backward and forward difference formula as given below:

$$\begin{aligned}\nabla . \left(\chi(G)\nabla u(x,y)\right) = (&\chi\left(G_{i+\frac{1}{2},j}\right) u_{i+1,j} + \chi\left(G_{i-\frac{1}{2},j}\right) u_{i-1,j} \\ &+ \chi\left(G_{i,j+\frac{1}{2}}\right) u_{i,j+1} + \chi\left(G_{i,j-\frac{1}{2}}\right) u_{i,j-1}) \\ &- (\chi\left(G_{i+\frac{1}{2},j}\right) + \chi\left(G_{i-\frac{1}{2},j}\right) \\ &+ \chi\left(G_{i,j+\frac{1}{2}}\right) + \chi\left(G_{i,j-\frac{1}{2}}\right)).\end{aligned} \tag{3.14}$$

3.3.2 Algorithm to implement the method

The algorithm in Algorithm 2 gives a clear understanding of the method proposed in Section 3.3.

Algorithm 2 GCDIE Algorithm.

1: $u_0 \leftarrow$ Image corrupted by noise and blur.
2: Evaluate the scalar regularization parameter λ using (3.12).
3: Evaluate $u_{\eta\eta}$ by (2.27), $\|\nabla u\|$ by (2.24) and $\nabla . \left(\chi(G)\nabla u(x,y)\right)$ by (3.14).
4: Take a very small time step Δt, that satisfy the CFL condition defined in (1.21).
5: $FOM_i \leftarrow 0$
6: Evaluate FOM_{i+1} using (1.59) for the initial noisy image u_0.
7: **while** $FOM_{i+1} - FOM_i < 0$ **do**. ▷ Iterate till the FOM decreases in the consecutive iterations
8: $FOM_i \leftarrow FOM_{i+1}$. ▷ Assign the current FOM value to the previous one.
9: Evaluate for u^{n+1} using the explicit method in (3.13).
10: $FOM_{i+1} \leftarrow$ The FOM calculated for the newly computed image u^{n+1}.
11: Update λ using (3.12).
12: **end while**

3.4 EXPERIMENTAL RESULTS AND DISCUSSIONS

We used the standard test images "Lena", "Woman", "phantom", "hibiscus" and "boat" to test and compare the performance of various methods under consideration and the one proposed in this chapter. These input images are corrupted by additive random Gaussian noise, making the Signal-to-Noise Ratio (SNR) of the noisy images: 12dB and we choose a value of 4 for the standard deviation σ in the Gaussian smoothing function G, given in (3.10). We have generated an out-of focus blur for the image using a Gaussian smoothing function with standard deviation $\sigma = 4$. The input images are normalized for their gray values in the range [0-1]. The scale space parameter $h = 1$ and the time step $\Delta t = 0.1$. The diffusivity function $\chi(.)$ in (3.10) is considered as $\chi(x) = \|x\|/max(\|x(i,j)\|)$, $\forall_{i,j}$, which is real and non-negative. The function $p(t)$ used in (3.10) is a non decreasing function of time which returns a value in the range (0,1] as already defined in (3.11). Though, it is visually obvious from the results that the proposed method outperforms the similar kinds of methods in the recent literature, the reconstruction has to be quantified numerically. Therefore, statistical quality measures are employed for quantifying reconstruction capabilities of various methods. These measures are outlined in the following section.

3.4.1 Quality Measures

We use the statistical quality measures like SNR, FOM and MSSIM to quantify the restoring capacity of the filter. These measures highlight the edge and structure preserving capability of the filter under consideration. The details of SNR, FOM and MSSIM are already given in Sections 1.4.1, 1.4.2 and 1.4.3 of Chapter 1, respectively.

3.4.2 Results and analysis

Figure 3.1 shows the results of the proposed method and existing methods in the literature, when applied on the image "Lena". It is evident from the figure that the proposed method preserves and enhances curvy edges and corners (structures having non-zero mean curvature values) present in the image. Figure 3.2 shows some enlarged portions of the image in Figure 3.1, after applying the proposed method and the method using the mean curvature as the control function. It is quite evident

that the features with non-zero curvature values (curvy edges and corners) are well enhanced by the proposed method. Especially the parts like lips, eyebrows, hair etc, are intact even after many iterations, whereas the MCM based methods smoothen-out these features. Figure 3.3 shows a *row-profile* of the above mentioned image, we have chosen 100^{th} row with 100 columns, the profile clearly shows the denoising and deblurring capability of the proposed method. In Figure 3.3(a) the row-profile of the original and the blurred & noisy signal are shown. In Figure 3.3(b) the performance of Alvarez shock filter (Alvarez and Mazorra 1994) is shown and it is quite obvious from this figure; the method has smoothened out the signal and many sharp edge features have been removed in the evolution process. In Figure 3.3(c) the result of the proposed method is shown. From this figure one can confirm that the proposed method has denoised the signal/image and has preserved and enhanced some of the high frequency features like edges and fine-details. Similar observations are made about another test image "Woman", the results are analogous to the ones that are discussed about the image "Lenna". For this image also the proposed method retains and enhances the edges better, compared to the other methods under consideration. The results of applying different methods for the image "Woman" are shown in Figure 3.4 and some enlarged portions of the degraded and reconstructed images are shown in Figure 3.5

The number of iterations n for each method is selected based on Pratt's FOM (1.59), in each iteration. One can easily observe that the FOM increases with the increase in iteration up to a certain limit and then it decreases gradually. The iteration corresponding to the maximum FOM value is taken as an ideal choice for the number of iterations n. As we have already observed, the measure FOM directly implies the edge preserving capability of a method. So the number of iterations n in each method is based on this Adaptive Selection Principle (ASP). The FOM plotted against the number of iterations for image "Lena" and "Woman" are shown in Figure 3.6(A) and Figure 3.6(B), respectively. All the results shown in Figures 3.1 and 3.4 are captured after the number of iterations evaluated based on this ASP. The number of iterations chosen for Alvarez, GCDD and proposed model are 80, 110 and 90, respectively (for the image Lena).

We measure the performance of the proposed method and the methods already existing in literature with quality measures like Pratt's FOM and MSSIM. The edge preserving capability of the filter is measured by *Pratt's FOM* as defined in (1.59).

The structural similarity is measured in terms of luminance, contrast and the

structure. We use MSSIM in (1.61) for measuring the structural similarity. These measures are tabulated in Table 3.1 for the image "Lena" and in Table 3.2 for the image "woman". From Tables 3.1 and 3.2 one can see that out of all the methods tabulated; the proposed method is having good response in terms of FOM and MSSIM when tested for images "Lena" and "Woman". Hence the structure and edge preserving capabilities of the method is superior to the other tabulated methods.

Table 3.1: Comparison of FOM & MSSIM for the image "Lena": using different methods in the literature.

METHODS	FOM	MSSIM
Alvarez Model	0.87	0.51
GCDD	0.42	0.41
Proposed GCDIE Model	0.91	0.64

Table 3.2: Comparison of FOM & MSSIM for the image "woman": using different methods in the literature.

METHODS	FOM	MSSIM
Alvarez Model	0.89	0.52
GCDD	0.45	0.38
Proposed GCDIE Model	0.93	0.61

Similar experiments were performed for the other test images "phantom", "hibiscus" and "boat" the filtered outputs are displayed in Figures 3.9, 3.10 and 3.11, respectively. However we observed that the statistical quality measures for these test images follow a similar pattern as that of the other test images "Lena" and "woman" (whose results are already demonstrated), therefore these measures are not explicitly provided here.

We repeated the experiments with different noise levels. The results (in graphs) of applying FOM at different SNR values (noise variances) are shown for the image "Lena" and "Woman" in Figure 3.7(A) and Figure 3.7(B), respectively. Similarly the results (in graphs) of applying MSSIM for the two test images at different SNR values are given in Figure 3.8(A) and Figure 3.8(B). The graphs shown in Figure 3.7 and Figure 3.8 are the graphical representation of FOM and MSSIM for various SNR values. From these graphs one can easily confirm that the proposed method has better

FOM and MSSIM values at all different levels of SNR values. Further we show the responses of various filters for different input images (phantom, hibiscus and boat) in Figures 3.9, 3.10 and 3.11, respectively. All these provided results endorse on the capability of the method to retain the edges while denoising the images and also enhancing the luminance and contrast of the images.

So we conclude that the Gauss curvature driven diffusion coupled with the shock filter proposed in this chapter is as efficient method for restoring images from their degraded (blurred and noisy) observations. Furthermore, this proposed model preserves semantic structures even with non-zero curvature values that are present in the images. This fact is quite evident in the results demonstrated.

A B

C D

E

Figure 3.1: Image "Lena":(A) Original image; (B) Blur and noisy image (out of focus blur generated using Gaussian kernel with standard deviation $\sigma = 4$, SNR of noisy image is 12dB); (C) After applying Alvarez model (MCM as diffusion Term); (D) After applying GCDD without shock; (E)After applying the proposed GCDIE Method.

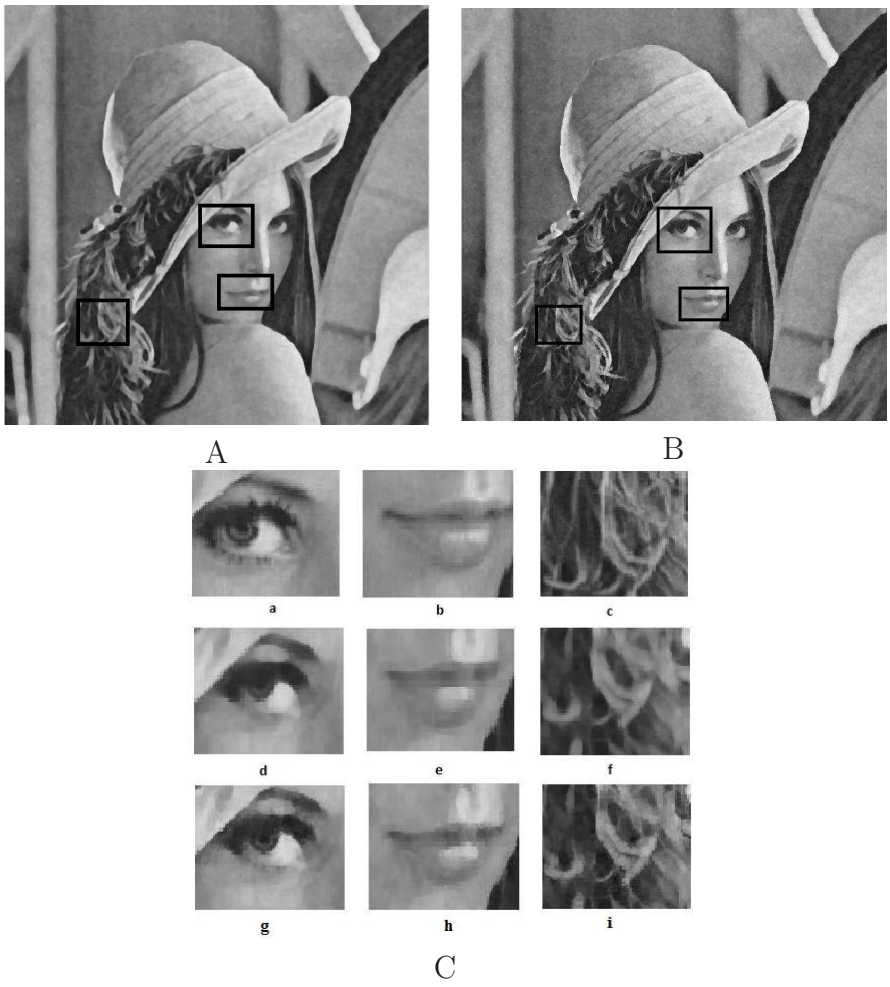

Figure 3.2: Image "Lena":(A) Selected portions of the filtered image using Alvarez method Alvarez and Mazorra (1994); (B) Selected portions of the image after applying the proposed method; (C)The enlarged selected portions : (a), (b) & (c) Portions of the original; (d), (e) & (f) Result of applying MCM based method; (g), (h) & (i) Result of applying the proposed method.

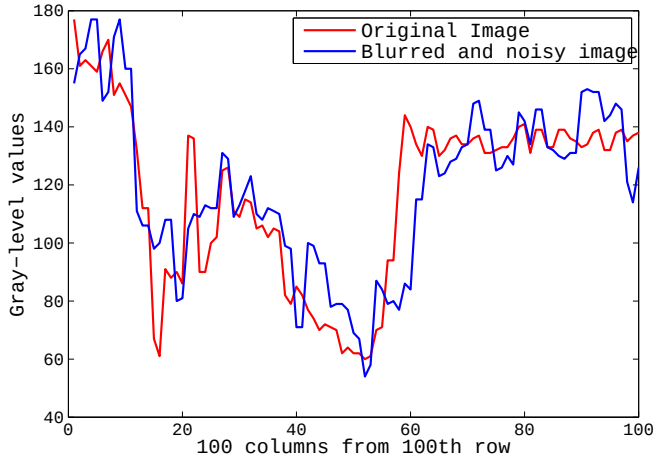

A

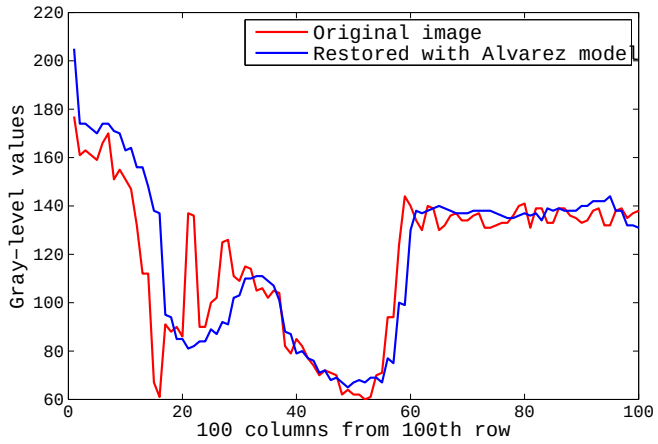

B

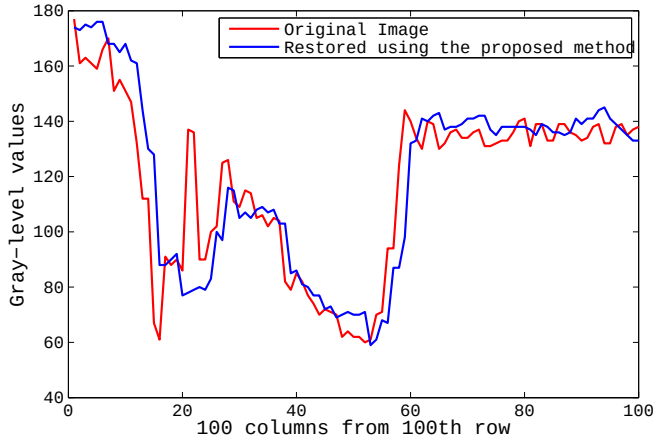

C

Figure 3.3: The row profile of the image "Lena" :(A) Original and Blurred-noisy signals; (B) Original and Reconstructed signals using Alvarez model; (C) Original and Reconstructed signals using Proposed GCDIE Method.

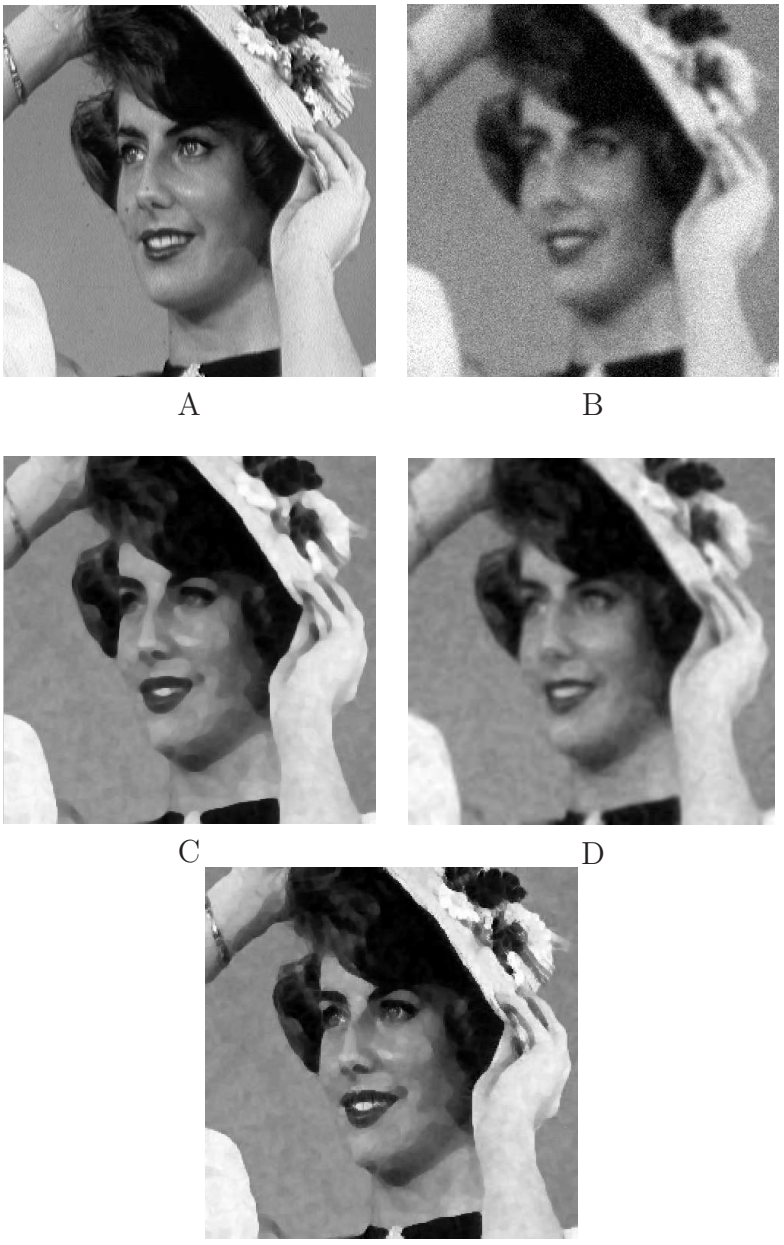

Figure 3.4: Image "woman":(A) Original image; (B) Blur and noisy image (out of focus blur generated using Gaussian kernel with $\sigma = 4$, SNR of noisy image is 12dB); (C) After applying Alvarez model (MCM as diffusion Term); (D) After applying GCDD without shock; (E) After applying the proposed GCDIE method.

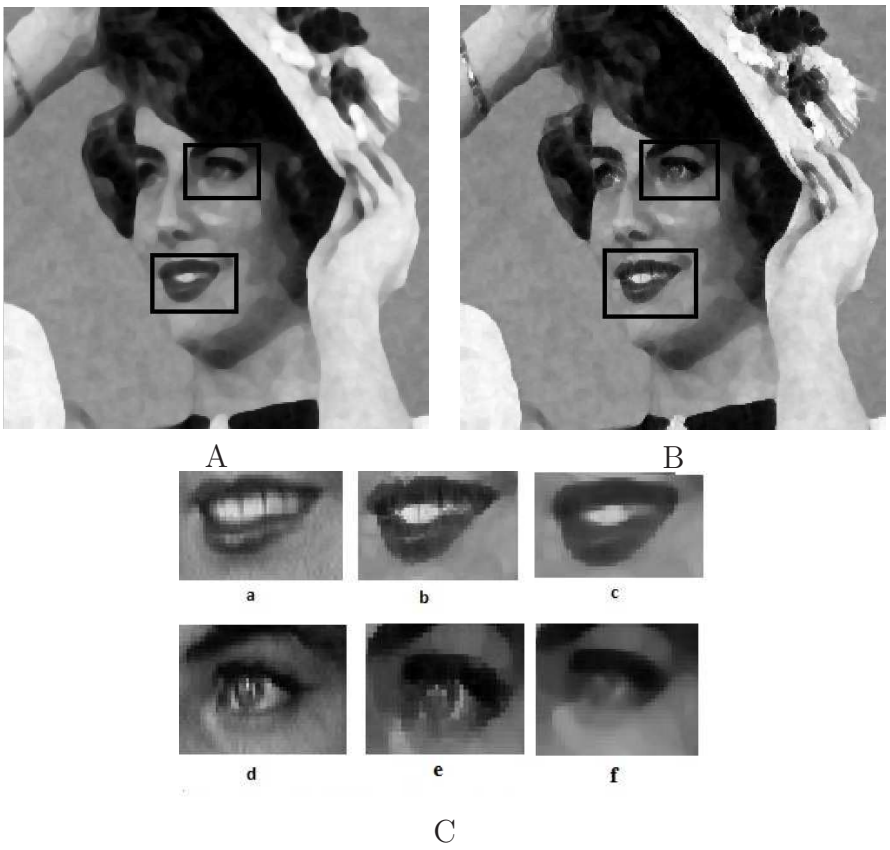

Figure 3.5: Image "woman":(A) Selected portions of the filtered image using Alvarez model Alvarez and Mazorra (1994) method; (B) Selected portions of the image after applying the proposed method; (C)The enlarged selected portions : (a) & (d) Parts of original image; (b) & (e) Result of applying the proposed method; (c) & (f) Result of applying MCM based method.

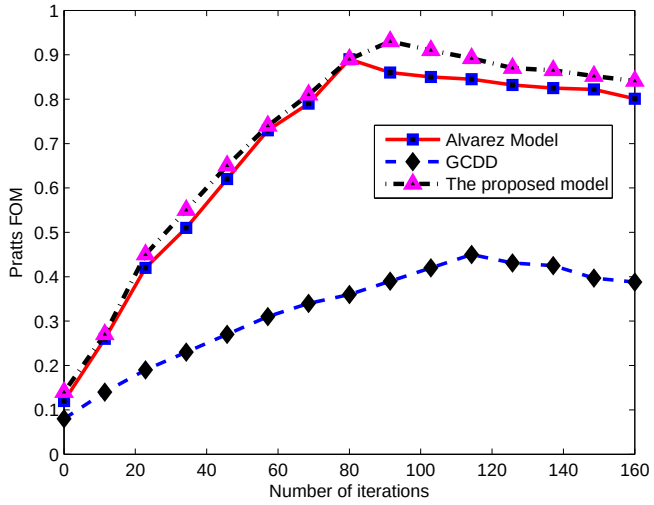

A

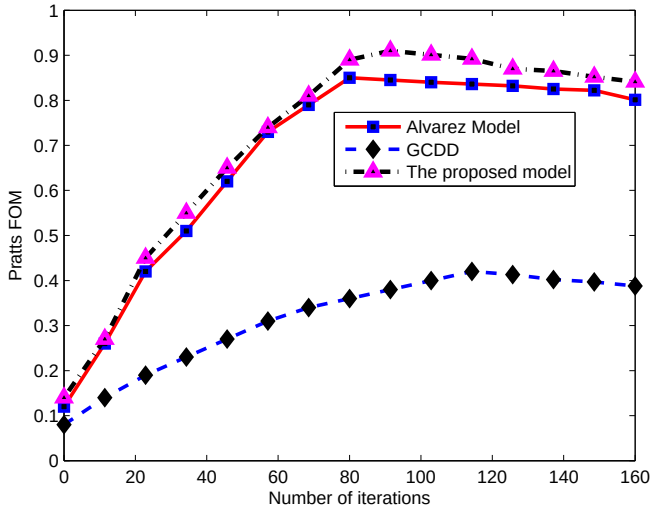

B

Figure 3.6: (A) FOM plotted against the Number of iterations for the image "Lena"; (B)FOM plotted against the Number of iterations for the image "Woman".

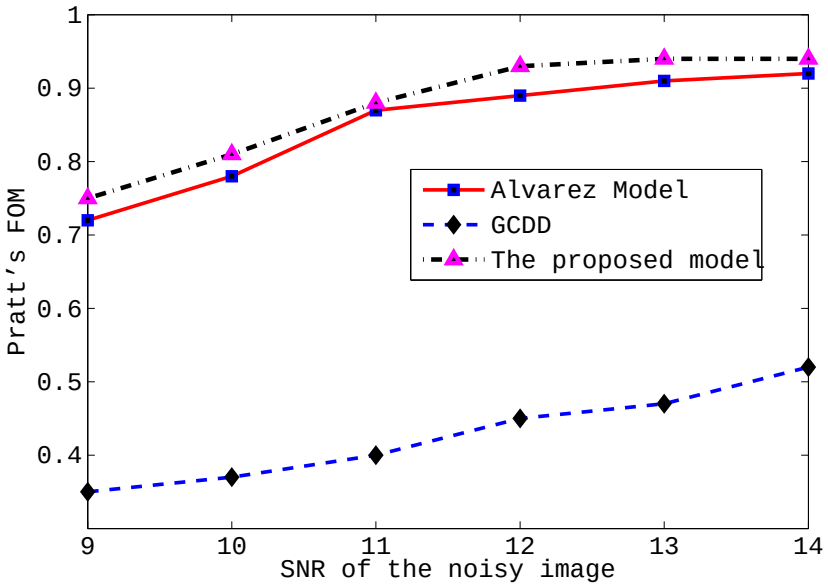

A

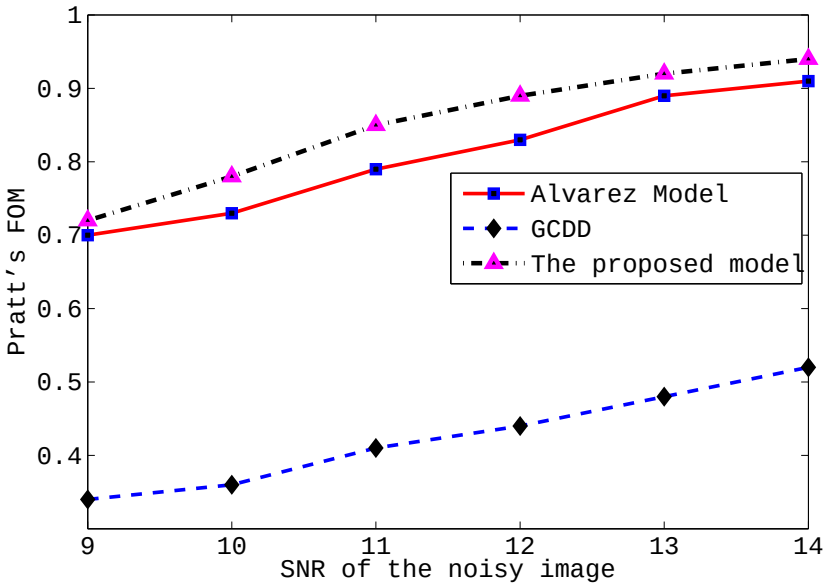

B

Figure 3.7: The plot showing Pratt's FOM measured under various methods (under consideration) for two different images (A) Pratt's-FOM plotted against the SNR for the image "Lena"; (B) Pratt's-FOM plotted against the SNR for the image "Woman".

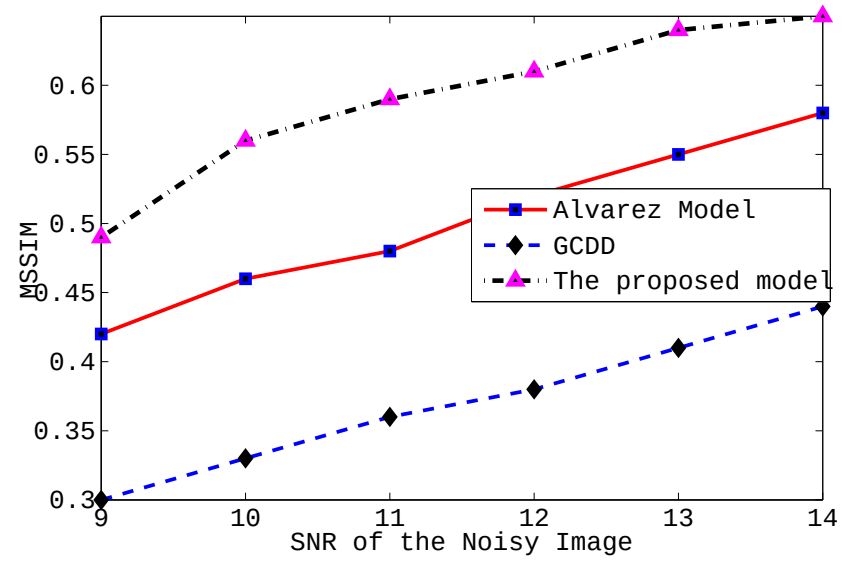

A

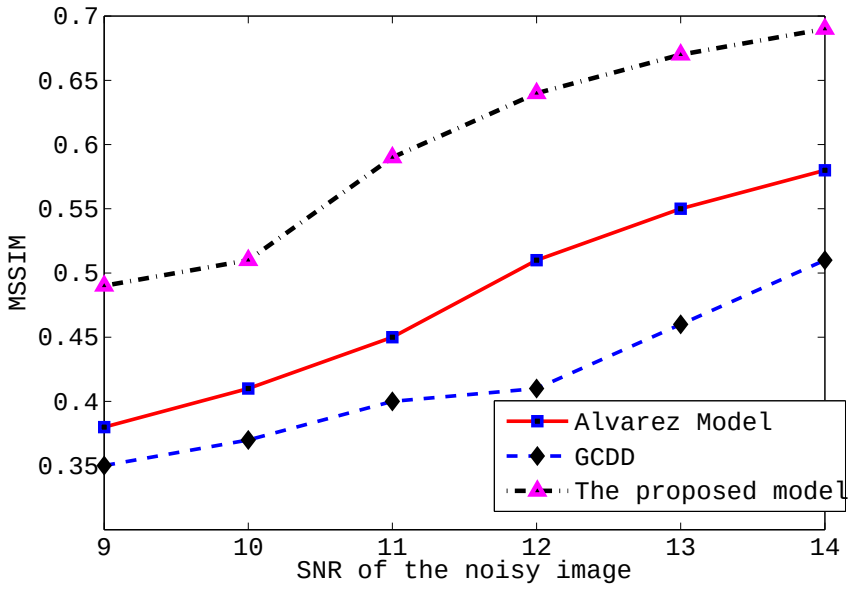

B

Figure 3.8: The plot showing MSSIM measured under various methods (under consideration) for two different images(A) MSSIM plotted against the SNR for the image "Lena"; (B) MSSIM plotted against the SNR for the image "Woman".

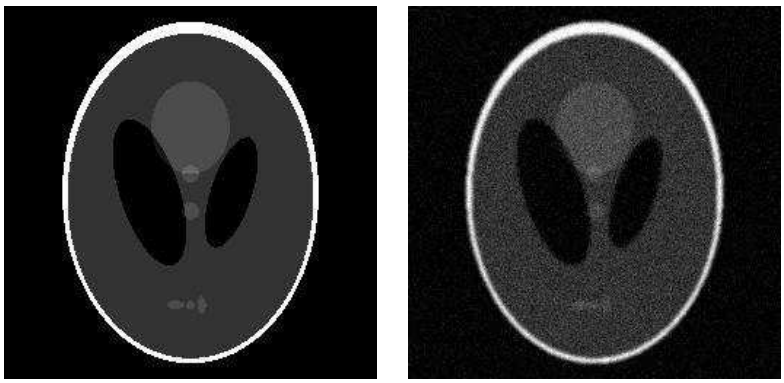

A B

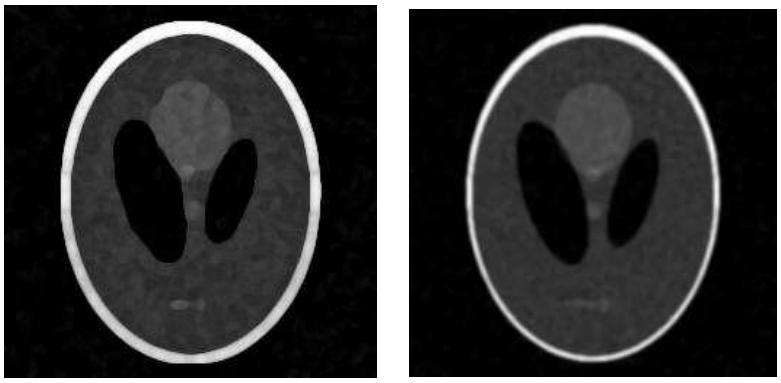

C D

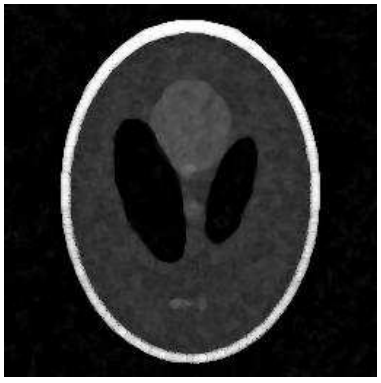

E

Figure 3.9: Image "phantom":(A) Original image; (B) Blur and noisy image (out of focus blur generated using Gaussian kernel with standard deviation $\sigma = 4$, SNR of noisy image is 12dB); (C) After applying Alvarez model (MCM as diffusion Term); (D) After applying GCDD without shock; (E) After applying the proposed GCDIE Method.

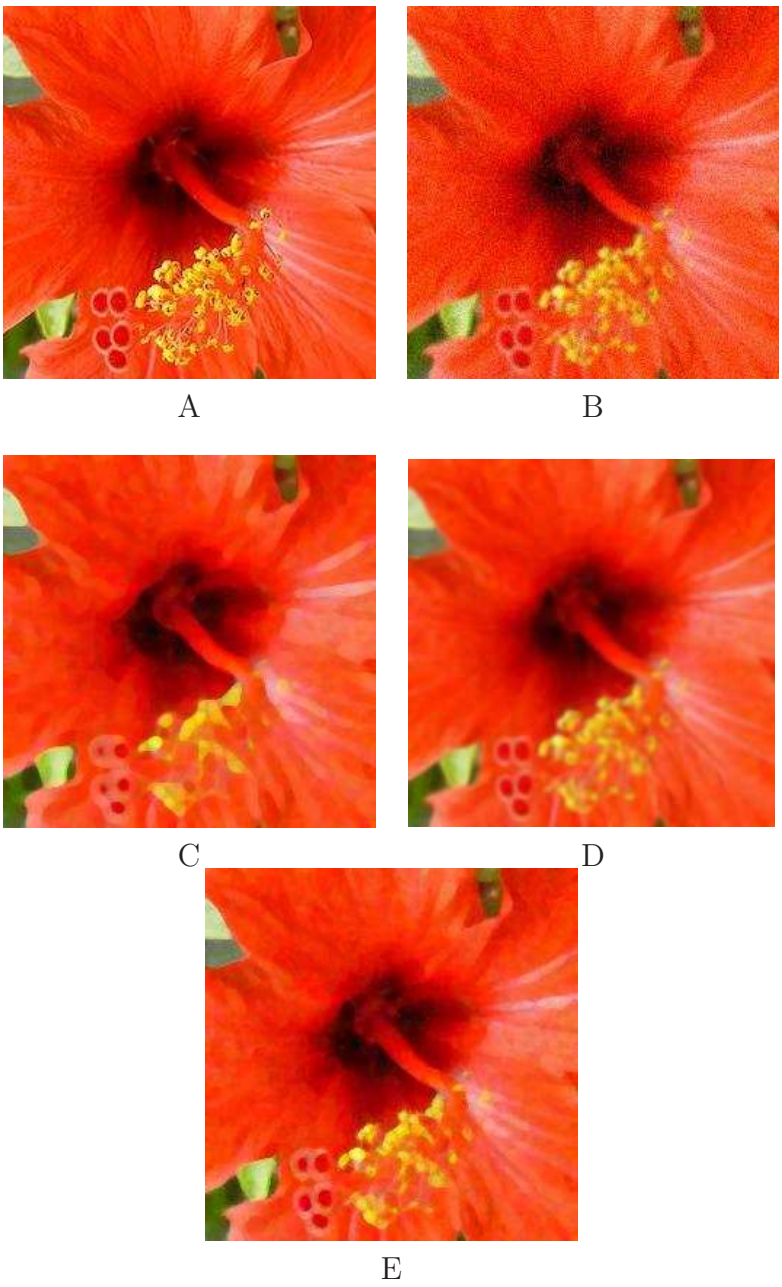

Figure 3.10: Image "hibiscus":(A) Original image; (B) Blur and noisy image (out of focus blur generated using Gaussian kernel with standard deviation $\sigma = 4$, SNR of noisy image is 12dB); (C) After applying Alvarez model (MCM as diffusion Term); (D) After applying GCDD without shock; (E) After applying the proposed GCDIE Method.

A B

C D

E

Figure 3.11: Image "boat":(A) Original image; (B) Blur and noisy image (out of focus blur generated using Gaussian kernel with standard deviation $\sigma = 4$, SNR of noisy image is 12dB); (C) After applying Alvarez model (MCM as diffusion Term); (D) After applying GCDD without shock; (E) After applying the proposed GCDIE Method.

Chapter 4

CURVATURE DRIVEN IMAGE INPAINTING

4.1 INTRODUCTION

Inpainting, a set of techniques for making undetectable modifications to images, is as ancient as art itself. Applications of image inpainting range from the removal of an object from a scene to the retouching of damaged painting or photograph. Inpainting can be done by using information from surrounding areas and merging the inpainted region into the image so seamlessly that a typical viewer is not aware of it. Inpainting can even be used to reverse deterioration or reconstruct damaged portions in images (e.g., cracks in photographs, scratches and dust spots in film), or to add or remove elements (e.g., stamped dates, red-eye, etc.) from photographs. In any case, the goal is to produce a modified image in which the inpainted portions remain un-noticeable to the naked eyes. The reconstructed image quality depends mainly on the underlying image features. If the inpainting domain is small compared to the image domain and the gray-level oscillations are minimal (or the image is less textured) then the inpainted image looks more natural. Since texture is a measure of image coarseness, smoothness and regularity, the images with texture contain regions characterized more by variation in the intensity values than by a single one.

Many digital inpainting algorithms have been proposed lately in the literature (see Chan and Shen (2001a), Bertalmio et al. (2001) and Shen (2003)). A broad classification for inpainting methods would be, statistical based (Shen 2003) and PDE or Variational based. PDE and variational based methods have recently became popular

among the researchers due to the stability in the solution and well defined theoretical background for uniqueness and existence of the solution.

Rest of the chapter is organized in four sections. In Section 4.2 an introduction to the PDE based inpainting methods is provided. In Section 4.3 variational inpainting methods are highlighted. In Section 4.4 a Gauss curvature driven inpainting method is proposed and its numerical implementations are discussed. Experimental results and observations are detailed in Section 4.5.

4.2 PDE BASED INPAINTING METHODS

Second-order diffusion methods can be used for image inpainting. Linear diffusion is the oldest and most widely explored diffusion method which is well-defined in the space of square integrable functions (L^2) and the solution does not allow discontinuities. If differentiability is imposed on the input image, then the solution will be well defined in the Sobolev space. A Sobolev inpainting filter can be formulated as:

$$\begin{array}{ll} \frac{\partial u}{\partial t} = u_{xx} + u_{yy} & \text{if } \mathbf{x} \in \Omega' \\ u = u_0 & \text{if } \mathbf{x} \notin \Omega' \end{array} . \tag{4.1}$$

One can notice that $u_{xx} + u_{yy} = u_{\xi\xi} + u_{\eta\eta}$ (we use these notations interchangeably), where $u_{\eta\eta}$ and $u_{\xi\xi}$ are the second order derivatives in the direction along the gradient and across it (see the expressions (2.27) and (2.28)). The symbol Ω' denotes the inpainting domain and $\mathbf{x} \notin \Omega'$ implies the non-inpainting domain (which is the complement of the inpainting domain). A Sobolev inpainting aims at interpolating the missing information based on the linear diffusion process. The method is isotropic and as mentioned above the solution will be smooth in nature.

Motivated by the anisotropic nature of the non-linear diffusion filter named Perona Malik filter (Perona and Malik 1990), it was used for inpainting images. Unlike linear diffusion filters the Perona-Malik filter doesn't weaken the edge features in the image. The non-linear Perona-Malik inpainting filter is defined as:

$$\begin{array}{ll} \frac{\partial u}{\partial t} = \nabla.\left(c(\|\nabla u\|)\nabla u\right) & \text{if } \mathbf{x} \in \Omega' \\ u = u_0 & \text{if } \mathbf{x} \notin \Omega' \end{array} , \tag{4.2}$$

where $c(.)$ stands for the coefficient of diffusion, which is a function of absolute gradient

of the image, refer Perona and Malik (1990) for more details on this filter. Though, this parabolic PDE retains the edges and finer details in due course of its evolution, it conditionally switches to an unstable enhancement during the inverse diffusion process (this phenomenon was already discussed in Chapter 1).

4.3 VARIATIONAL INPAINTING METHODS

The idea of inpainting is to interpolate the damaged or intended image domain (inpainting domain) Ω' in an image $u \subset \mathbb{R}^2$, based on the information from u on the boundary pixels $\delta\Omega'$ of Ω' and pixels in the surrounding band of Ω'. Figure 4.1 shows a pictorial representation of the inpainting domain. Variational based inpainting methods try to minimize an energy functional which eventually results in a restored version of the observed (damaged/degraded) image.

$$\begin{aligned} &\min_u \textstyle\int_{\Omega'} J(u)dxdy \\ &\text{subject to } \|u - u_0\|^2 = 0. \end{aligned} \tag{4.3}$$

where u and u_0 are the original and reconstructed images, respectively. Here the functional $J(u)$ is to be minimized subject to the constraint. Hence the minimization

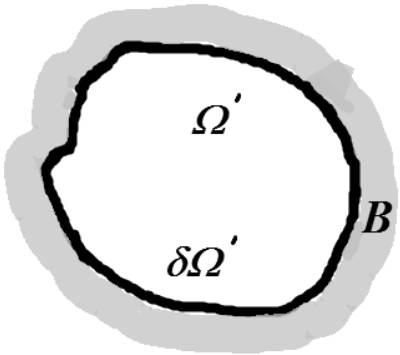

Figure 4.1: Image inpainting domain.

problem can be reformulated using a Lagrange function as:

$$E(u,\lambda) = \int_{\Omega'} J(u)dxdy + \lambda \int_{\Omega} (u-u_0)^2 dxdy, \tag{4.4}$$

where λ denotes a scalar regularization parameter. In fact the second term in (4.4) is a reactive (fidelity) term which is bound to be active only in the non-inpainting domain.

Many functionals have been proposed in the literature based on their reconstruction capabilities. The first kind of functional proposed was based on the Tikhonov regularization method (Tikhonov and Arsenin 1977). Here the functional is the $\mathcal{L}^2$ norm of the gradient: $\|\nabla u\|^2$. Using this functional, (4.4) can be modified as:

$$E(u,\lambda) = \int_{\Omega'} \|\nabla u\|^2 dxdy + \lambda/2 \int_{\Omega} (u-u_0)^2 dxdy. \tag{4.5}$$

Now to solve this Lagrange functional or to find the minimum of the functional E the corresponding Euler-Lagrange (E-L) equation needs to be solved. The local extrema of the functional can be represented by the steady state of the corresponding Euler-Lagrange equation. Since the functional in (4.5) is convex (refer Appendix A-4 for details), the local extrema correspond to the local minimum or the desired solution. The second term in (4.5) refers to the fidelity term, which ensures that, the deviation of the solution image from the original one is minimal. The E-L equation corresponding to (4.5) is:

$$-\nabla^2 u + \lambda(u-u_0) = 0, \tag{4.6}$$

The gradient descent solution is:

$$\frac{\partial u}{\partial t} = \nabla^2 u - \lambda(u-u_0) \tag{4.7}$$

The PDE follows the boundary condition in (1.30) and initial condition (1.31). The solution belongs to L^2 space. Assuming the continuity of the function u, the solution will be well defined in $W^{1,2}$ (Sobolev) space. Using this variational method for image inpainting results in the following equations (we remark that here the reactive term

is not used for inpainting):

$$\begin{array}{ll} \frac{\partial u}{\partial t} = \nabla^2 u & \text{if } \mathbf{x} \in \Omega' \\ u = u_0 & \text{if } \mathbf{x} \notin \Omega' \end{array} . \tag{4.8}$$

Here $\mathbf{x}$ is assumed to be a pixel in the image. Discretization of (4.8) using explicit Euler scheme, with finite central difference results in (the space steps Δx and Δy are taken as 1):

$$u^{t+1} = u^t + \Delta t \times ((u_{xx} + u_{yy})), \tag{4.9}$$

where u^t is the image function at the t^{th} iteration, Δt is the time step. The second-order derivatives along x and y directions are discretized as follows:

$$u_{xx} = u_{x+1,y} - 2u_{x,y} + u_{x-1,y}, \tag{4.10}$$

and

$$u_{yy} = u_{x,y+1} - 2u_{x,y} + u_{x-1,y} \tag{4.11}$$

This method interpolates the images and provides a good approximation to the original image. However, the filter is equipped with a Laplacian operator ∇^2, which is significantly isotropic and results in smoothing-out the image features like edges and finer details.

An anisotropic model based on the Total Variation (TV) norm was proposed for image inpainting in Chan and Shen (2001b). This model is a generalization of the Total Variational model proposed in Rudin et al. (1992) for denoising. The TV based model retains the edges while diffusing the images. The energy functional proposed by Rudin et al. (1992) for denoising the images (with reference to inpainting) is:

$$E(u, \lambda) = \int_{\Omega'} \|\nabla u\| dxdy + \lambda/2 \int_{\Omega} (u - u_0)^2 dxdy, \tag{4.12}$$

where $\int_\Omega \|\nabla u\| dxdy$ is the TV-norm of the functional $\|\nabla u\|$. By minimizing the energy functional E in (4.12) with respect to u will result in the desired solution. The second term in (4.12) refers to the fidelity term as defined above. The solution is defined in the space where the Total Variations are bounded or in a space of bounded variation. Since the functional $\int_\Omega \|\nabla u\| dxdy$ is convex (refer Appendix A-4 for details and derivations), the minimization results in an unique solution. Using this method

for image inpainting yields the following equation (reactive term in the E-L equation is omitted for inpainting):

$$\begin{array}{ll} \frac{\partial u}{\partial t} = \nabla . \left(\frac{\nabla u}{\epsilon + \|\nabla u\|} \right) & \text{if } \mathbf{x} \in \Omega', \\ u = u_0 & \text{if } \mathbf{x} \notin \Omega'. \end{array} . \tag{4.13}$$

The boundary condition (1.30) and the initial condition (1.31) remains applicable for this PDE as well. The parameter ϵ is to avoid division by zero in the constant intensity regions, where $\|\nabla u\|$ tends to zero. The parameter λ is evaluated and updated in each iteration based on the procedure in Rudin et al. (1992). Discretization of (4.13) using explicit Euler scheme, with finite central difference results in (the space steps Δx and Δy are taken as 1):

$$u^{t+1} = u^t + \Delta t \times \frac{(u_{xx} u_y^2 - 2u_{xy} u_x u_y + u_{yy} u_x^2)}{(\epsilon + ux^2 + u_y^2)^{3/2}}, \tag{4.14}$$

where u_{xx} and u_{yy} are defined as in (4.10) and (4.11), respectively. The mixed derivative is defined as

$$u_{xy} = 1/4 \times (u_{x+1,y+1} + u_{x-1,y-1} - u_{x+1,y-1} - u_{x-1,y+1}). \tag{4.15}$$

Even though TV- based methods are stable and provide unique solutions, the textures and finer details are severely affected by the diffusion flow. Despite preserving the edges while diffusing the data, TV-based diffusion flow will eventually result in forming constant patches in the filtered output (causing *staircase* effect).

Second-order variational methods (like TV based models) have drawbacks as in the connection of edges over large distances or the smooth propagation of level lines (sets of image points with constant gray-value) into the damaged domain. In an attempt to solve both the connectivity principle and the so called *staircase* effect resulting from second order image diffusions, a number of third and fourth order diffusions have been suggested for image inpainting.

Variational third order approach is also used in image inpainting, Curvature Driven Diffusion (CDD) method is a good example (Chan and Shen 2001a). The evolution

PDE for CDD is read as:

$$\begin{array}{ll} \frac{\partial u}{\partial t} = \nabla . \left[\frac{g(|\mathcal{K}|)}{\|\nabla u\|} \nabla u \right] & \text{if } \mathbf{x} \in \Omega' \\ u = u_0 & \text{if } \mathbf{x} \notin \Omega' \end{array} . \tag{4.16}$$

Here $g(|\mathcal{K}|)$ is a non increasing function (similar to (1.29)) of the curvature of the level curve: $\mathcal{K}$, defined as:

$$\mathcal{K} = \nabla . \left(\frac{\nabla u}{\|\nabla u\|} \right), \tag{4.17}$$

with the initial condition (1.31) and boundary condition (1.30). While realizing the Connectivity Principle in visual perception, (i.e., level lines are connected also across large inpainting domains) the level lines are still interpolated linearly (which may result in corners in the level lines along the boundary of the inpainting domain) in this model.

A further refinement of the CDD model was done by Chan and Shen (2001) towards restoring blurred and noisy non-textured images. In this model the authors proposed to combine the fidelity term in (4.12) with the CDD term. The fidelity characteristics are bound to be active on the non-inpainting domain and CDD will be driving the inpainting process in the inpainting domain. This model will approach to the TV model by Rudin et al. (1992) in the non-inpainting domain and acts like a CDD in the inpainting domain. This model can be precisely formulated as:

$$\frac{\partial u}{\partial t} = \nabla . \left(\frac{G(x,|\mathcal{K}|) \nabla u}{\|\nabla u\|} \right) - \lambda_\epsilon(\mathbf{x})(u - u_0), \tag{4.18}$$

where

$$G(\mathbf{x}, |\mathcal{K}|) = \begin{cases} 1 & \mathbf{x} \notin \Omega' \\ g(|\mathcal{K}|) & \mathbf{x} \in \Omega' \end{cases} , \tag{4.19}$$

and

$$\lambda_\epsilon(\mathbf{x}) = \begin{cases} \lambda & \mathbf{x} \notin \Omega' \\ 0 & \mathbf{x} \in \Omega' \end{cases} , \tag{4.20}$$

where λ is a regularization parameter described in ROF model (Rudin et al. 1992). The existence of a TV inpainting in Ω', which does an inpainting inside the domain Ω' and noise cleaning outside the domain is proved in the THEOREM 4.5 in Chan and Shen (2001). To be precise this model behaves like a CDD model in the

inpainting domain and a TV denoising model outside the inpainting domain. Though this model can handle inpainting the noisy and damaged images, it suffers from the same issues, as those of the CDD model.

In another work Chan et al. (2002) re-investigated the proposal of Masnou and Morel (1998) on image interpolation based on Euler's elastica energy. For any value of $p > 1$ one can define the *p-elastica* energy as:

$$J_p[u] = \int_\Omega (a + b\mathcal{K}^p)\|\nabla u\| dxdy, \tag{4.21}$$

here a and b are constants and $\mathcal{K}$ is the curvature. It has been proved in Chan et al. (2002) (THEOREM 4.6), that the optimal choice of p is in the open interval (1,3), for any value of $p \geq 3$ the energy functional $J[u]$ becomes unbounded. Choosing $p = 2$ in (4.21), it becomes a *Euler-elastica* model. This elastica model is thoroughly analyzed in Masnou and Morel (1998) for image interpolation and was adopted by Chan et al. (2002) for image inpainting . This model was proposed, to address the issues of curvature driven diffusion considered by Chan and Shen (2001a).

The most natural approach to solve the inpainting problem is to mimic how professional image restorators inpaint manually. As discussed in Bertalmio et al. (2000), authors extend edges from the boundary of Ω', connect these extended edges, and then fill in intra-regions accordingly. This idea has been found to produce satisfactory results (Bertalmio et al. 2000, 2001). To justify this theoretically, we may have to introduce few more notions. First, isophotes are level lines of equal gray-levels. The direction of the isophotes can be interpreted as:

$$\nabla^\perp u,$$

where $\nabla^\perp u = (-\partial_y, \partial_x)$ is the direction of the smallest change and the smoothness is interpreted as

$$\nabla^2 u,$$

where $\nabla^2 u$ is the Laplacian operator. In view of $\nabla^\perp u$ and $\nabla^2 u$, in order to obtain a good restoration one can: propagate $\nabla^2 u$ in the direction of $\nabla^\perp u$ from the boundary of Ω', when all the information is propagated, the level-lines of $\nabla^2 u$ become parallel to $\nabla^\perp u$, which is the desired solution Bertalmio et al. (2000). See Figure 4.2 for a visual representation. Therefore, mathematically the inpainting problem can be expressed

as:

$$\begin{array}{ll} \frac{\partial u}{\partial t} = \nabla\nabla^2 u.\nabla^{\perp} u & \text{if } \mathbf{x} \in \Omega' \\ u = u_0 & \text{if } \mathbf{x} \notin \Omega' \end{array} . \tag{4.22}$$

In Bertalmio et al. (2000), the authors iteratively propagate $\nabla^2 u$ in the direction of $\nabla^{\perp} u$ until the steady state is obtained, i.e, $\frac{\partial u}{\partial t} = 0$ in (4.22).

In Chan et al. (2002), the authors present the fourth order elastica inpainting PDE which combines CDD and the transport process of Bertalmio et al. (2000). The proposed energy functional can be read as:

$$J(u) = \int_{\Omega'} (a + b|\mathcal{K}|^2)\|\nabla u\| + \lambda/2 \int_{\bar{\Omega}} (u - u_0)^2 dxdy. \tag{4.23}$$

Here $\bar{\Omega}$ denotes the non-inpainting domain. Here we remark that, $x \notin \Omega'$ implies $x \in \bar{\Omega}$. The Euler-Lagrange (EL) equation corresponding to the energy functional (4.23) can be solved using the steepest descent method:

$$\frac{\partial u}{\partial t} = \nabla.\vec{V} - \lambda_{\epsilon}(\mathbf{x})(u - u_0), \tag{4.24}$$

where $\vec{V}$ is defined as:

$$\vec{V} = (a + b|\mathcal{K}|^2)\vec{n} - \frac{2b}{\|\nabla u\|}\frac{\partial \mathcal{K}}{\partial \vec{t}}\|\nabla u\|\vec{t}, \tag{4.25}$$

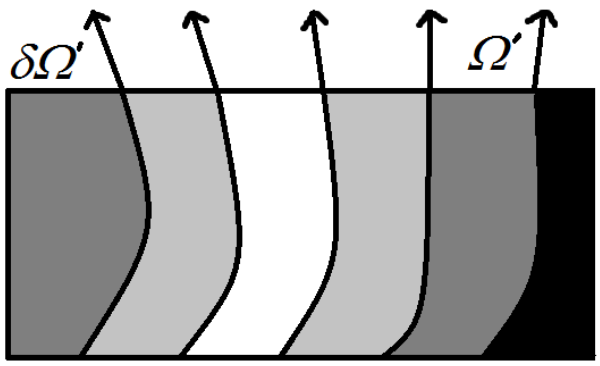

Figure 4.2: The smoothness information propagated in the direction of isophotes.

where $\vec{t}$ and $\vec{n}$ are the vectors tangent and normal to the level lines. In this model the level lines are connected by minimizing the integral over their length and their squared curvature within the inpainting domain. This leads to a smooth connection of level lines also over large distances.

One of the major issues with the curvature based (CDD) (4.18) and mean-curvature based (4.23) diffusion methods is that, they diffuse based on the mean curvature of the level-curve. During this evolution process the features like curved edges and corners tends to become more curvy and vanish after a finite number of evolution.

In this chapter we propose to inpaint a blurred and noisy image without degrading the features with non-zero mean curvature values. Unlike the mean curvature driven diffusion process the proposed method does not affect the curvy edges and corners.

4.4 GAUSS CURVATURE DRIVEN IMAGE INPAINTING

In this model we propose to drive the diffusion process using a Gauss-curvature driven diffusion process as discussed in Section 3.3. The Gauss-curvature driven diffusion process will retain the structures even with non-zero mean curvature values. The proposed filter is also equipped with a deblurring term which deblurs the images with a known blurring kernel. Now the problem is to inpaint blurry and noisy images without affecting the curvy edges and corners present in the images. So, the degraded image to be inpainted can be written as (we recall the image degradation model from Chapter 1):

$$u_0 = k * u + n. \tag{4.26}$$

The symbols are in same sense as in (1.1). The image u_0 is a degraded image that needs to be denoised, deblurred and inpainted. The inpainting domain is assumed to be known prior. The energy functional associated with the reconstruction problem can be defined as:

$$J(u) = \int_{\Omega'} \psi(\|\nabla u\|)dxdy + \lambda/2 \left(\int_{\bar{\Omega}} (k * u - u_0)^2 dxdy - |\Omega|\sigma^2 \right) \tag{4.27}$$

where $|\Omega|$ is the total number of pixels in the image, σ^2 is the noise variance and λ is the regularization parameter, $\psi(.)$ is the potential function and the gradient of which

is the flux function $\phi(.)$ defined as:

$$\nabla(\psi(\|\nabla u\|)) = \phi(\nabla u) = f(G)\nabla u. \tag{4.28}$$

Here G is the Gaussian curvature as given in (3.8). In our experiments we assume $f(G) = |G|$, where $|.|$ denotes the absolute value. Since the flux function is an increasing function of Gauss curvature the associated energy functional becomes convex.

Now the inpainting problem can be observed as an energy minimization problem for the functional $J(u)$ defined in (4.27). The inpainting or reconstruction model can be formulated as the Euler-Lagrange equation for the unconstrained minimization problem defined in (4.27) with the boundary condition (1.30) and initial condition (1.31), at steady-state the solution approaches the original one or the minimum is obtained:

$$\frac{\partial u}{\partial t} = \nabla. \left[\frac{\chi(\mathbf{x},G)\nabla u}{\|\nabla u\|}\right] - \lambda_\epsilon(\mathbf{x})k * (k * u - u_0). \tag{4.29}$$

Here, the function $\chi(.)$ follows the definition:

$$\chi(\mathbf{x}, G) = \begin{cases} 1 & \text{if } \mathbf{x} \notin \Omega' \\ f(G) & \text{if } \mathbf{x} \in \Omega' \end{cases}, \tag{4.30}$$

where $\lambda_\epsilon(.)$ is the regularization parameter as defined in (4.20), k is a Gaussian kernel. Note, $\mathbf{x} \notin \Omega'$ denotes the pixel that belongs to the image domain Ω but not inpainting domain Ω' [1].

4.4.1 Numerical implementations

We use explicit Euler scheme for discretizing the problem in (4.29). Using the central difference scheme, the second derivatives along x and y can be written as in (2.29). The expression $\nabla. (f(G)\nabla u(x, y))$ is discretized using backward and forward difference

[1] Here we remark that, $x \notin \Omega'$ implies $x \in \bar{\Omega}$.

formula as given below:

$$\begin{aligned}\nabla.\left(f(G)\nabla u(x,y)\right) = (&f\left(G_{i+\frac{1}{2},j}\right)u_{i+1,j} f\left(G_{i-\frac{1}{2},j}\right)u_{i-1,j} \\ &+ f\left(G_{i,j+\frac{1}{2}}\right)u_{i,j+1} f\left(G_{i,j-\frac{1}{2}}\right)u_{i,j-1}) \\ &- (f\left(G_{i+\frac{1}{2},j}\right) + f\left(G_{i-\frac{1}{2},j}\right) \\ &+ f\left(G_{i,j+\frac{1}{2}}\right) + f\left(G_{i,j-\frac{1}{2}}\right)),\end{aligned} \tag{4.31}$$

where G is defined as in (3.8). Implementation of other terms using the explicit central differencing scheme is already discussed, therefore, it is skipped here for brevity. The convolution in (4.29) (which is in spatial domain) is implemented as multiplication in Fourier domain.

4.5 EXPERIMENTAL RESULTS AND DISCUSSIONS

4.5.1 Experimental set-up

The standard test images like "hibiscus", "parrot", "woman", "Lena", "boat" and "phantom" are used to test and compare the performance of the method with some of the relevant methods discussed in the literature. The test images are degraded using an out-of-focus blur and a Gaussian additive noise (with variance 0.01). The blurring kernel is chosen to be a Gaussian kernel with standard deviation $\sigma = 4$ The degraded image has a PSNR value 8.5dB. The convolution operation is implemented using FFT multiplication. All the test images (which are gray scale images with intensity values in the range [0-255]) are normalized in the range [0-1] for our experiments. The test images are cropped to the size 256x256 pixels. The test images "hibiscus", "woman","Lena", "boat" and "phantom" are subjected to random data loss of 75% and the images are inpainted to compensate for the data loss of 75%. Image "parrot" is inpainted for removing the cage bars in the input image.

We use the quality measures like PSNR, FOM and SSIM to quantify the quality of reconstruction. The details of these measures can be found in Chapter 1, Section 1.4.

4.5.2 Results and analysis

The resulting images after applying different inpainting methods are given in Figures 4.3, 4.4 and 4.5 for the images hibiscus, parrot, woman, respectively. The test images woman and hibiscus show the reconstruction capacity of various inpainting methods under consideration. These two images are subjected to random data loss (of 75%) and a Gaussian noise is added into these images (with mean zero and variance 0.01). The image parrot is shown to demonstrate the inpainting capacity of the filter; the image is equipped with an inpainting domain which covers the cage-bars in the input image. From these three figures (viz. Figures 4.3, 4.4 and 4.5) the fact that, the proposed method reconstructs and inpaints the images is substantiated, without further doubts.

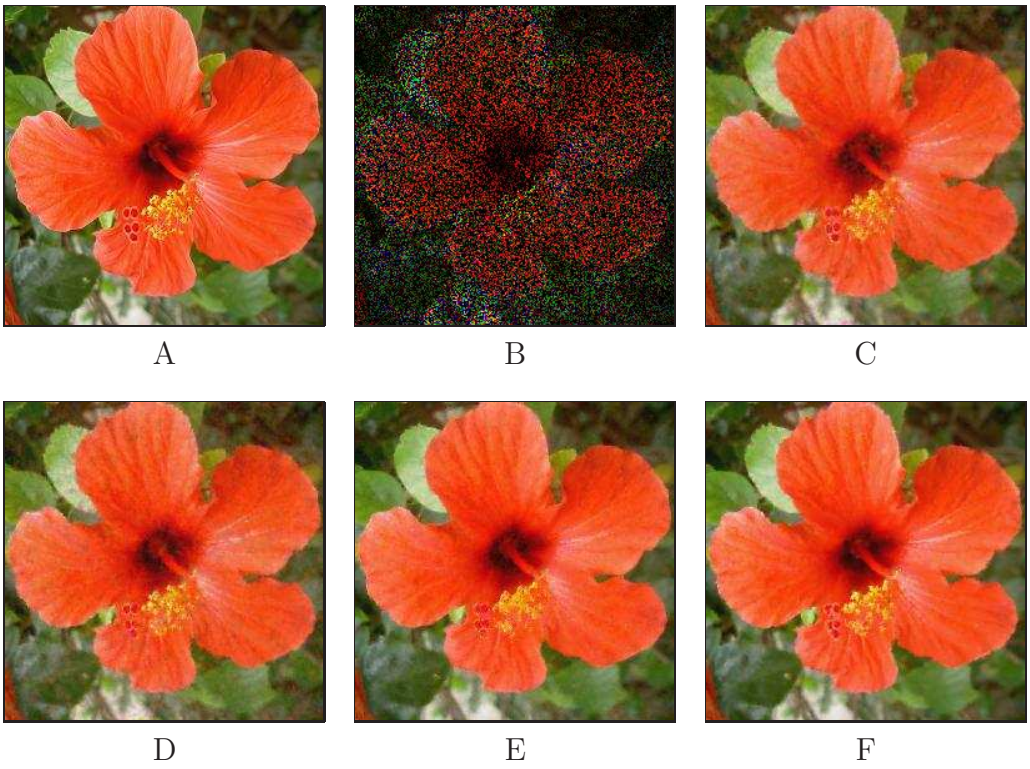

Figure 4.3: Image 'hibiscus' (Original and reconstructed ones): (A) Original Image; (B) Image with data lost from random pixels (75%) and corrupted by a Gaussian noise with mean zero and variance: $\sigma^2 = 0.01$; (and blurred); (C) result of applying Perona-Malik method; (D) result of TV based method; (E) result of CDD method; (F) result of the proposed method.

The selected portions from image "hibiscus" and "woman" are enlarged for bet-

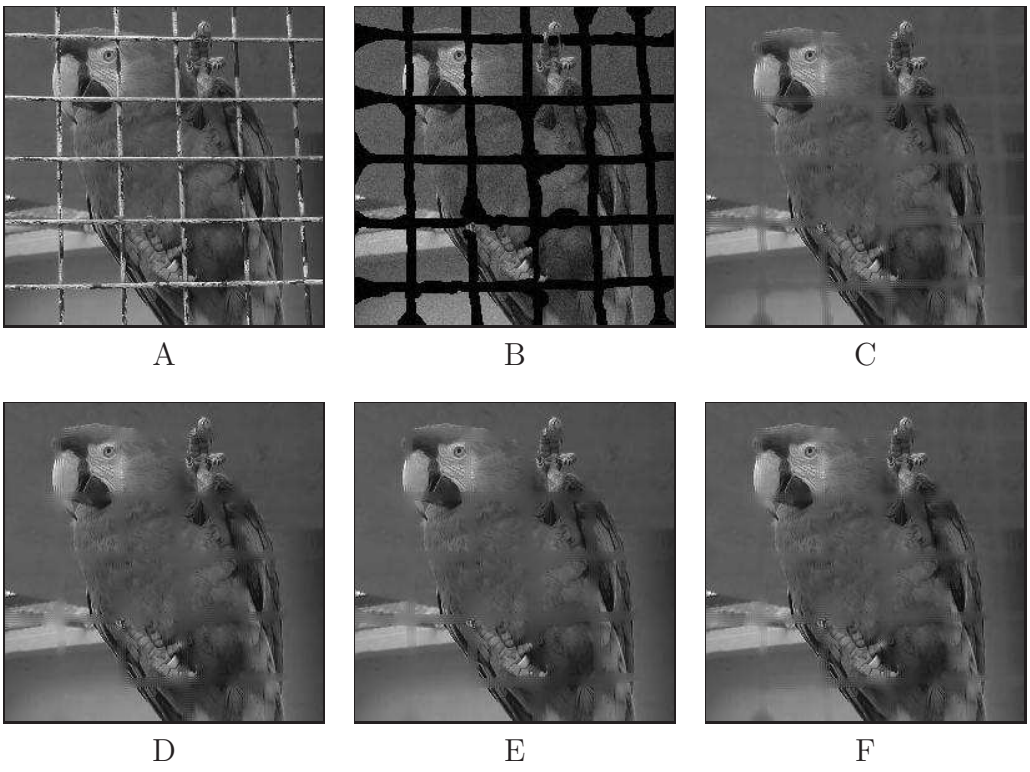

Figure 4.4: Image 'parrot'] (Original and inpainted) ones: (A) Original Image; (B) Image with the mask in the domain to be inpainted, corrupted by a Gaussian noise with mean zero and variance: $\sigma^2 = 0.01$; (and blurred) (C) result of applying Perona-Malik method; (D) result of TV based method; (E) result of CDD method; (F) result of the proposed method.

ter visibility in Figures 4.6 and 4.7, respectively. From these enlarged portions one can analyze that the proposed method has preserved features with non-zero mean curvature values (viz. curvy edges, corners etc.).

Furthermore the figures Figures Lena, boat and phantom were also tested with the methods under consideration and the results are shown in Figures 4.8, 4.9 and 4.10, respectively. The statistical mesures are not provided explicitly for these images for the reason that they follow the patter similar to the other images.

The highest values of PSNR obtained for various test images after applying different methods under consideration are tabulated in Table 4.1. The PSNR values keep on increasing in each iteration as the filtered image approaches the original one The proposed method improves the PSNR value of the degraded image at a better rate compared to its counterparts. PSNR of the noisy input image is 8.5 dB. The results are shown for the various test images at a fixed input PSNR value. The characteris-

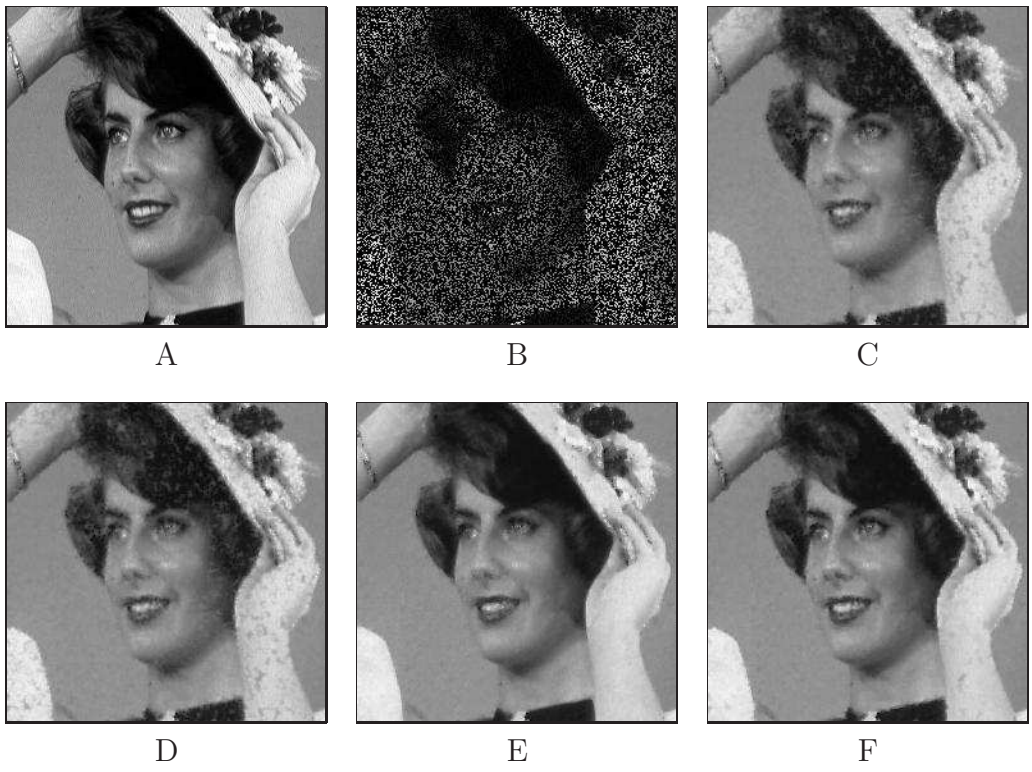

Figure 4.5: Image 'woman' (Original and reconstructed ones): (A) Original Image; (B) Image with data lost from random pixels (75%) and corrupted by a Gaussian noise with mean zero and variance: $\sigma^2 = 0.01$ (and blurred); (C) result of applying Perona-Malik method; (D) result of TV based method; (E) result of CDD method; (F) result of the proposed method.

tics follow the same pattern for any PSNR values of the input images. Therefore, the explicit result is shown only for a single input PSNR value. The MSE values are also determined for various test images with different PSNR values. The result for MSE is the inverse of the result for PSNR. Since, the images are normalized the numerator of expression (1.63) becomes unity and therefore, the MSE and PSNR become inverses of each-other. For the above reason, results are not shown explicitly for MSE, but PSNR. The SNR values of various filtered images (restored using different filters) are tabulated in Table 4.2

Pratt's Figure of Merit (FOM) for various test images under different methods is shown in Table 4.3 . The proposed method is giving good response in terms of FOM as compared to the other methods proposed in the literature. In addition to the above three measures we measure the Mean-SSIM for various test images reconstructed using different methods under consideration, the values are shown in Table 4.4. The values

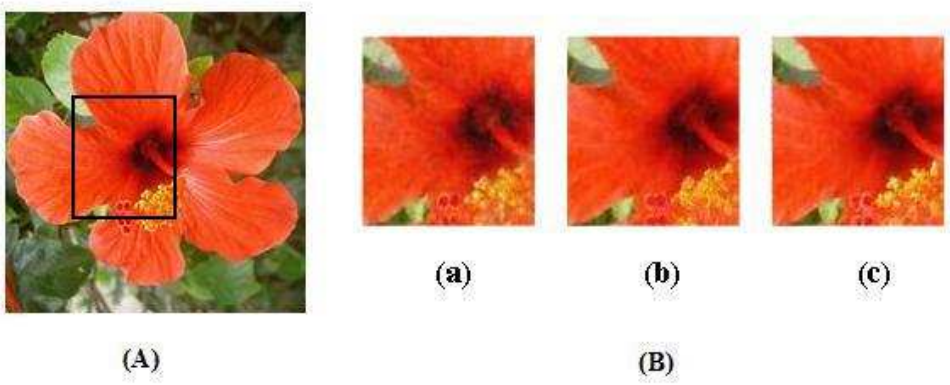

Figure 4.6: Image "hibiscus":(A) Original Image; (B) (a) Selected portions of the image inpainted using TV filter (b) selected portion filtered using CDD based inpainting; (c) & (f) Result of applying proposed method.

Table 4.1: PSNR for the inpainted images (PSNR for the input image is :8.5dB).

Images	SOB	TV	CDD	The proposed method
Hibiscus	29.23	29.88	29.92	32.23
Parrot	28.42	29.22	28.35	31.33
Woman	28.44	29.35	28.45	31.68

are in favor of the proposed method. In other words the proposed method preserves important structures in the course of evolution.

We have tested the performace of our method with various test images for a random data lose (of the input image) up to 90% and we observed that the reconstructed images are of distinguishable quality up to this level of data lose, beyond which the restored image is highly degraded, see Figure 4.11.

In this chapter a third-order Gauss curvature driven inpainting was adopted for inpainting or reconstructing the images from their damaged observations. The method proposed was indented to handle the structures with non-zero mean curvature values with a special care.

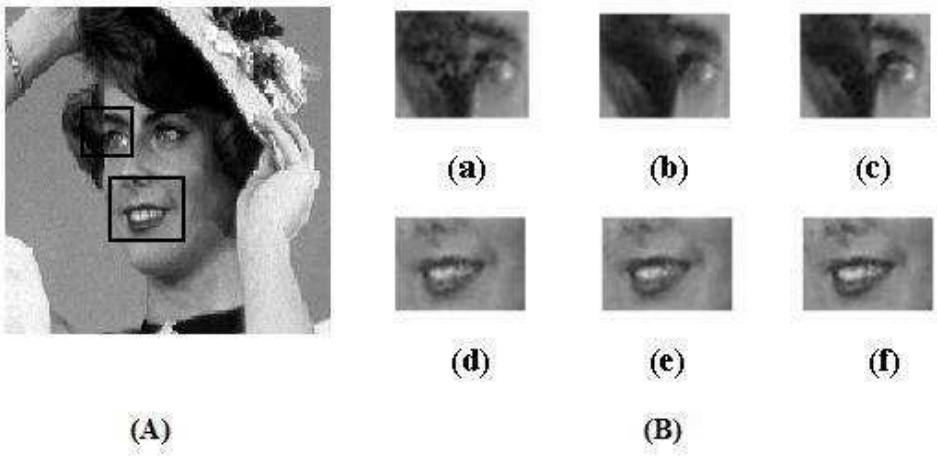

Figure 4.7: Image "Woman":(A) Image woman; (B) (a)& (d) Selected portions of the image inpainted using TV filter (b) selected portion filtered using CDD based inpainting; (c) Result of applying proposed method.

Table 4.2: SNR for the inpainted images (SNR for the input image is :1.52dB).

Images	SOB	TV	CDD	The proposed method
Hibiscus	14.23	15.68	16.72	18.73
parrot	14.42	16.21	17.85	19.13
Woman	13.43	15.45	17.35	18.18

Table 4.3: Pratt's FOM for the inpainted images (PSNR for the input image is :8.5dB).

Image	SOB	TV	CDD	The proposed method
Hibiscus	0.76	0.87	0.85	0.91
Parrot	0.78	0.85	0.81	0.88
Woman	0.77	0.89	0.87	0.90

Table 4.4: MSSIM for the inpainted images (PSNR for the input image is :8.5dB).

Image	SOB	TV	CDD	The proposed method
Hibiscus	0.79	0.77	0.78	0.82
Parrot	0.72	0.74	0.75	0.79
Woman	0.74	0.75	0.74	0.81

A B C

D E F

Figure 4.8: Image 'lena' (Original and reconstructed ones): (A) Original Image; (B) Image with data lost from random pixels (75%) and corrupted by a Gaussian noise with mean zero and variance: $\sigma^2 = 0.01$ (and blurred); (C) result of applying Perona-Malik method; (D) result of TV based method; (E) result of CDD method; (F) result of the proposed method.

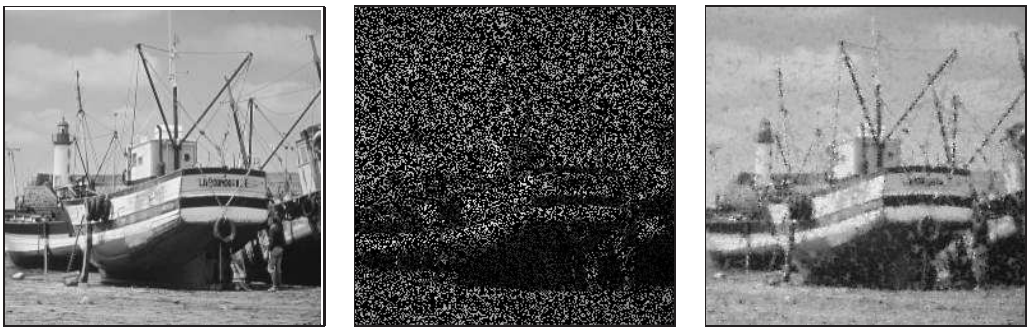

A B C

D E F

Figure 4.9: Image 'boat' (Original and reconstructed ones): (A) Original Image; (B) Image with data lost from random pixels (75%) and corrupted by a Gaussian noise with mean zero and variance: $\sigma^2 = 0.01$ (and blurred); (C) result of applying Perona-Malik method; (D) result of TV based method; (E) result of CDD method; (F) result of the proposed method.

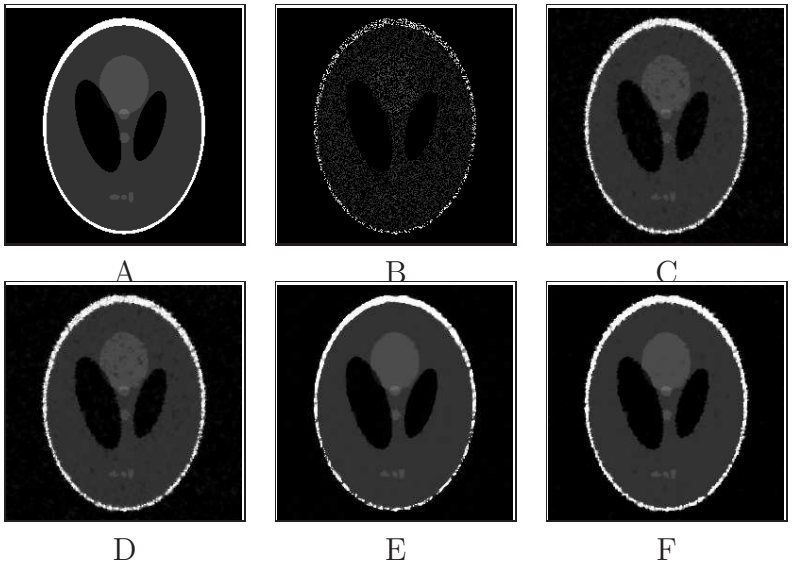

Figure 4.10: Image 'phantom' (Original and reconstructed ones): (A) Original Image; (B) Image with data lost from random pixels (75%) and corrupted by a Gaussian noise with mean zero and variance: $\sigma^2 = 0.01$ (and blurred); (C) result of applying Perona-Malik method; (D) result of TV based method; (E) result of CDD method; (F) result of the proposed method.

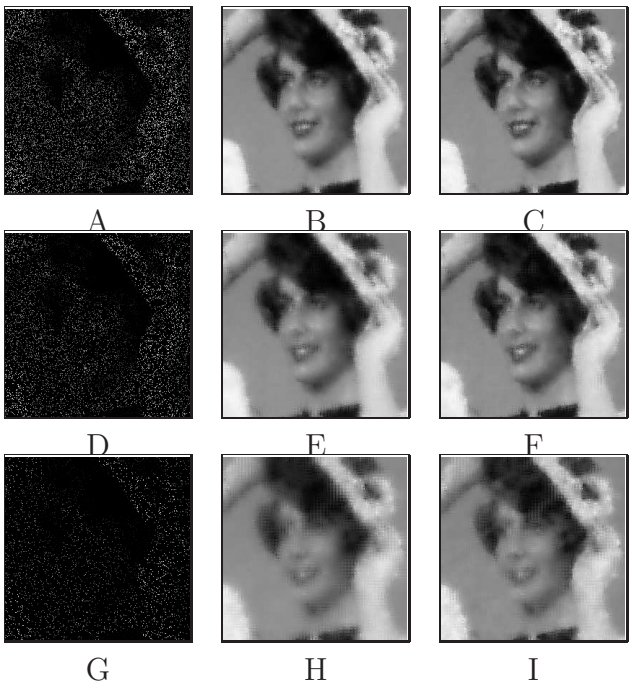

Figure 4.11: Outputs of CDD and the proposed method applied on the image "woman" for various data lose. (A) (D) (G) The images with 87 %, 90% and 92% data loss (B) (E) and (H) Inpainted using CDD method (C)(F)and (I) Inpainted using the proposed method.

Chapter 5

FOURTH-ORDER PDE FOR IMAGE ENHANCEMENT

5.1 INTRODUCTION

The fourth-order diffusion filters were introduced in the literature to handle the *staircase* effect caused due to the piece-wise approximation of the observed image by the second-order diffusion filters. However, the smoothness of the filtered images increases with the order of the filter. Moreover, the fourth order filters alone cannot handle the enhancement requirement, where the images are degraded by the device artifacts (causing blurness in the image). Therefore, coupling the fourth-order diffusion filter along with the stable hyperbolic shock filter can improve the enhancement capacity of the fourth-order filter to a large extent. The detailed description of hyperbolic shock filters were presented in Chapter 3. A controlled application of shock and diffusion can effectively transform the images into a considerable enhanced ones.

Many of the filters that couple a diffusion term and a shock term, use a variation of Mean Curvature Motion(MCM) in place of the diffusion term, (see Alvarez and Mazorra (1994) and Gilboa et al. (2002)). The MCM was introduced to image processing by Marquiana and Osher (2000). As already discussed in Chapter 1, in the MCM model, each of the level curves in the image evolves with the speed proportional to their mean curvature and eventually results in making the curved edges more curvy until it vanishes to a point. In addition to this, all the second-order diffusion methods including MCM approximates the observed image with piece-wise constant images and the evolution eventually results in forming constant patches in the filtered image. As

already explained in the previous chapter this defect is known as *staircase* effect.

In this chapter, we propose a fourth-order diffusion coupled shock filter to denoise and deblur the images. By combining the fourth-order diffusion along with the shock term, we can exploit the characteristics inherent in fourth-order diffusion filters to denoise the image while enhancing the edge features by the shock term. The experimental results are provided for textured and non-textured images and the results of the proposed filter are compared qualitatively and quantitatively with the most relevant image enhancement methods in the literature.

Rest of the chapter is organized in three sections. Section 5.2 gives a mathematical background of fourth-order denoising filters and their properties. Section 5.3 highlights the proposed method and its numerical implementations. Section 5.4 elaborates on the experimental results and their comparison with the existing methods for image enhancement.

5.2 FOURTH-ORDER DENOISING FILTERS

The second-order non-linear diffusion methods are devised in such a way that they diffuse in the homogeneous regions at a faster rate as compared to non-homogeneous ones. All the second-order non-linear diffusion methods approximate the observed image with piece-wise constant images. The PDE evolution eventually results in forming piece-wise patches during the early stages of evolution and finally these patches combine to form a level image. This level image is the only minimum of the energy functional associated with the second-order PDE. Similarly, during the inverse diffusion any piece-wise constant image is a global minimum of the energy functional, therefore the blocks will appear in the early stages of evolution and they remain without any change during the course of evolution.

As discussed in Chapter 1, Section 1.2.3, the fourth-order diffusion filters were introduced to handle the hazards due to the staircase effect (You and Kaveh 2000, Lysaker et al. 2003). Moreover, due to the convex nature of the energy functional the solution is unique (see Appendix A-3).

Even-though the fourth-order PDE equation in (1.36) is capable of removing the noise by penalizing less on the edges and without causing any *staircase* effect, the convergence rate is very slow for this PDE. Besides, the ramp edges are not well preserved in the evolution process, see Hajiaboli (2009) for details. These two issues

of (1.36) were addressed by Hajiaboli (2009). In Hajiaboli (2009), the author replaces the *Laplacian* of the image in the diffusion coefficient function with the gradient magnitude of the image. The diffusion equation considered in Hajiaboli (2009) is:

$$\frac{\partial u}{\partial t} = -\nabla^2 \left(c\left(\|\nabla u\| \right) \nabla^2 u \right), \tag{5.1}$$

where $c(.)$ is a non-increasing function bounded in (0,1]. Here $c(.)$ is defined as:

$$c(\|\nabla u\|) = \frac{1}{1 + (\|\nabla u\|/\kappa)^2}. \tag{5.2}$$

The filter in (5.1) can still support the planar approximation of the image removing the *staircase* effect. The *ramp* preservation capacity of the filter can be explained by considering the fact that: $\frac{\partial u}{\partial t} \to 0$ as $\nabla u \to 0$ (refer Hajiaboli (2009) for details).

The filter given by (5.1) can address the slow convergence rate of (1.36) and also preserves the ramp edges. However, the isotropic nature of this filter makes it a second choice, when it comes to the denoising of images with edges and textures. The edge descriptor ($\nabla^2 u$) in this case is the *Laplacian* operator, which is isotropic in nature and diffuses in all directions equally. Another improved filter was proposed in Hajiaboli (2010), which is a fourth-order generalization of a second-order filter proposed in Carmona and Zhong (1998). The filter proposed in Hajiaboli (2010), uses directional derivatives for smoothing the images in place of the *Laplacian* operator. This results in different diffusion magnitudes in different directions and ensures that the speed of diffusion is more along the edges than across them. The aforementioned property makes it an anisotropic filter which can remove the noise effectively in all the regions including the edges, penalizing less on the edge features. This modified filter can be formulated as:

$$\frac{\partial u}{\partial t} = -\nabla^2 c_1 \left(c_2 u_{\eta\eta} + c_3 u_{\xi\xi} \right), \tag{5.3}$$

where c_1, c_2 and c_3 are the diffusivity functions which control the amount of diffusion in different directions. Here η represents the direction along the gradient, ξ the direction along the isophotes and $u_{\xi\xi}$ denotes the MCM and as defined in (3.4). The diffusivity functions can be appropriately tuned to get different magnitudes of diffusion in different directions. In Hajiaboli (2010), the author has chosen $c_1 = c_2 = c(\|\nabla u\|)$ and

$c_3 = 1$. With these substitutions, (5.3) can be rewritten as:

$$\frac{\partial u}{\partial t} = -\nabla^2 \left(c(\|\nabla u\|)^2 u_{\eta\eta} + c(\|\nabla u\|) u_{\xi\xi} \right), \tag{5.4}$$

where $c(.)$ is a non-increasing function as in (5.2) and $c(\|\nabla u\|) = 1$ when $\|\nabla u\| = 0$ (in the homogeneous areas). Under this condition, the diffusion equation transforms to:

$$\frac{\partial u}{\partial t} = -\nabla^2 (u_{\eta\eta} + I u_{\xi\xi}). \tag{5.5}$$

From the above equation one can find that the filter in (5.4) acts like an isotropic filter in the smooth (homogeneous) areas where $\|\nabla u\| = 0$. When $c(\|\nabla u\|) \neq 1$ the filter will act like an anisotropic filter with varying diffusion magnitudes in different directions. Furthermore, it can be easily observed that $c(\|\nabla u\|)^2 \leq c(\|\nabla u\|)$ because $c(\|\nabla u\|) \leq 1$, hence, the speed of diffusion will be more in the direction of isophotes as compared to the direction of the gradient.

However, none of the filters discussed above does a real enhancement to the image edges or details. Though these filters denoise images preserving the planar approximations, they hardly are capable of enhancing the image features. The enhancement may be unavoidable, in cases where the images are captured with defective sensors causing blurness in the sensed images.

5.3 THE FOURTH-ORDER ENHANCEMENT FILTER (FOEF)

All the facts discussed above motivated us to use a fourth-order diffusion term in (5.4) along with the shock term to enhance images. This shock coupled diffusion filter can denoise the images anisotropically while preserving the edges (including ramp edges), without causing any *staircase* effect and will attain steady state at a faster rate. Hence, we propose to fit this fourth-order diffusion term in (5.4) along with a modified version of the shock term proposed in Alvarez and Mazorra (1994). The proposed filter can be modeled as:

$$\begin{aligned} u_t = &-\frac{2}{\pi}\, arctan(G_\sigma * u_{\eta\eta} \times p(t)) \|\nabla u\| \\ &- \lambda \nabla^2 \left(c(\|\nabla u\|)^2 u_{\eta\eta} + c(\|\nabla u\|) u_{\xi\xi} \right), \end{aligned} \tag{5.6}$$

where $G_\sigma * u_{\eta\eta}$ is the Gaussian convolved (with the spread of the Gaussian kernel σ) version of $u_{\eta\eta}$ and $p(.)$ is as defined in (3.11). We recall from Chapter 3, Section 3.3, the *arctan* function is a "soft *sign* function" which provides a more natural appearance to the enhanced image (Gilboa et al. 2002), therefore, this function is used instead of the *sign* function in (3.3). The parameter λ is a positive scalar value, which controls the magnitude of shock and diffusion. The function $c(.)$ is a non-increasing function as defined in (5.2). The terms $u_{\eta\eta}$ and $u_{\xi\xi}$ are the second-order directional derivatives along the gradient and the isophotes, respectively. The other notations are as in (3.3). The function $p(t)$ inside the *arctan* function controls the effect of shock during the early stages of evolution. During the initial phases of evolution the function $p(.)$ returns a value much smaller than one and after a finite number of iterations the function $p(.)$ always returns '1'. Thereafter, the filter acts like a shock coupled diffusion filter regularized by the control parameter λ. The parameter λ is evaluated and updated in each iteration using the expression:

$$\lambda = \frac{\int_\Omega \frac{2}{\pi}\, arctan(G_\sigma * u_{\eta\eta} \times p(t))\|\nabla u\|}{\int_\Omega \nabla^2 \left(c(\|\nabla u\|)^2 u_{\eta\eta} + c(\|\nabla u\|)u_{\xi\xi}\right)}. \tag{5.7}$$

5.3.1 Numerical implementations

The gradient descent scheme is used for solving the PDE in (5.6), see Section (1.2.1.4) for details on the scheme. Explicit Euler schemes are followed for discretizing the PDE, the details were provided in Section (1.2.1.5). However, the Euler schemes works well with Parabolic PDE's, whereas they tends to react poorly to the Hyperbolic PDE as far as stability is concerned. Therefore, to solve the hyperbolic term (shock term) in the proposed PDE (FOEF) *upwind* scheme is used. The hyperbolic PDE implementation is already discussed in Section (2.3.1) in Chapter 2, therefore we refer to the section for details.

The explicit Euler equation with finite central difference scheme is used for the diffusion term in (5.6).
Let $g(\|\nabla u\|) = c(\|\nabla u\|)^2 u_{\eta\eta} + c(\|\nabla u\|)u_{\xi\xi}$,
then

$$\nabla^2 g^n_{x,y} = g^n_{x+1,y} + g^n_{x-1,y} + g^n_{x,y+1} + g^n_{x,y-1} - 4g^n_{x,y}. \tag{5.8}$$

With the help of above discretization one can write the discretization for the filter in

(5.6).

$$u_t^{n+1} = u^n - \Delta t \times ((2/\pi) arctan\left(G_\sigma * u_{\eta\eta}^n \times p(t)\right) |\nabla u^n| + \lambda \nabla^2 \left(c(\|\nabla u^n\|)^2 u_{\eta\eta}^n + c(\|\nabla u^n\|)) u_{\xi\xi}^n\right), \quad (5.9)$$

we recall that, $u_{\eta\eta}$ is discretized as in (2.27), $u_{\xi\xi}$ is discretized as (2.28) and $\|\nabla u\|$ is defined as (2.24) (hyperbolic shock filters are discretized using *upwind* scheme).

5.3.2 Algorithm to implement the method

The following algorithm (Algorithm 3) gives a clear understanding of the method proposed in Section 5.3.

Algorithm 3 Fourth-order Enhancement Algorithm.

1: $u_0 \leftarrow$ Image corrupted by noise and blur.
2: $\lambda \leftarrow$ Scalar positive value evaluated using (5.7).
3: Evaluate $u_{\eta\eta}$ by (2.27), $|\nabla u|$ by (2.24), $u_{\xi\xi}$ by (2.28) and $\nabla^2(g^n(x,y))$ by (5.8).
4: Evaluate $c(\|\nabla u\|)$ and $c(\|\nabla u\|)^2$ by equation (5.2).
5: Take a very small time step Δt, that satisfy the CFL condition in (1.21).
6: $SNR_i \leftarrow 0$
7: Evaluate SNR_{i+1} using (1.58) for the initial noisy image u_0.
8: **while** $SNR_{i+1} - SNR_i < 0$ **do**. ▷ Iterate till the SNR decreases in the consecutive iterations
9: $SNR_i \leftarrow SNR_{i+1}$. ▷ Assign the current SNR value to the previous one.
10: Evaluate for u^{n+1} using the explicit method in (5.9).
11: $SNR_{i+1} \leftarrow$ The SNR calculated for the newly computed image u^{n+1}.
12: Update λ using (5.7)
13: **end while**

5.4 EXPERIMENTAL RESULTS AND DISCUSSIONS

We used a synthetic image "phantom" (a constant intensity image), a natural image "Lena" (a partially textured image) , two partially textured natural images "Woman", "Boat" and a color image "hibiscus" to test the performance of our algorithm. In all the experiments the intensity values of the images are normalized to the range [0-1].

Though the quality of the filtered output can be visually compared, we provide quantitative measurements for the performance of various methods cited in this work along with the proposed one (FOEF). We use three different image quality metrics Signal-to-Noise Ratio (SNR), Pratt's Figure of Merit (FOM) (Pratt 1977) and Structural Similarity Index Metric (SSIM) (Wang and Bovik 2004) to compare the performance of our method to the other relevant methods in the literature.

5.4.1 Image quality measures

Statistical quality measures are used to quantify the restoring capacity of the filter under consideration. Here, we employ the measures like SNR, FOM and M-SSIM. These measures highlight the edge and structure preserving capability of the filter under consideration. The details of SNR, FOM and SSIM are given in Sections 1.4.1, 1.4.2 and 1.4.3 of Chapter 1, respectively.

5.4.2 Experimental set-up

The test images are corrupted by Gaussian noise making the SNR of the noisy image 8 dB and we have chosen a value 4 for the standard deviation σ in the Gaussian smoothing function G in the expression (5.6). A blurred image (out-of-focus blur) is generated using a Gaussian smoothing function with standard deviation $\sigma = 4$. The scale space parameter $h = 1$. The time step $\Delta t = 0.01$ for all the fourth-order methods except the fourth-order regularization method in Lysaker et al. (2003). For this method the time step is chosen as $\Delta t = 0.002$, because the method is highly sensitive to the time step.

In each experiment, the performance of the proposed method (FOEF) was compared to that of other filters like: fourth-order denoising by You and Kaveh (2000), regularized fourth-order denoising technique by Lysaker et al. (2003), the modified fourth-order method proposed by Hajiaboli (2009) and Hajiaboli (2010) and the shock filter proposed by Alvarez and Mazorra (1994). The performance of each method is quantified in terms of different quality measures defined above and are demonstrated and compared in the subsequent sections.

5.4.3 Results and analysis

The visual results of applying different enhancement techniques on the image "phantom" image is shown in Figure 5.1C-5.1G. This image is a non-textured image with constant intensity regions. The "phantom" image consists of regions with different contrast and geometric shapes. We choose the value 0.006 for the parameter λ in our experiments. The blurred and noisy image (shown in Figure 5.1B) is used as an input to different image enhancement methods in the literature along with the one proposed in this chapter. The output results shown are quite in favor of the claim that, the FOEF method enhances the edges and denoises the image better than the other methods shown in the results.

The results of different methods in the literature along with the FOEF when applied to a partially textured natural image "Lena" is shown in Figure 5.2C-5.2G. The results of various methods including the FOEF applied on the natural images "Woman" and "Boat" are shown in Figures 5.3 and 5.4, respectively. Finally a color image ("hibiscus") is tested and the results are provided in Figure 5.5. This image shows the response of various filters to the color image. One can visualize from the Figures 5.1, 5.2 , 5.3, 5.5, 5.4 and 5.5 that the FOEF performs better (in terms of enhancement) than the other methods.

The experiments are conducted for various noise levels. Figure 5.6 shows the perspective results of various filters applied to the image "phantom" corrupted by three different noise-levels. The filtered results are shown for the input noise level 6dB, 7dB and 9dB, respectively. The noisy image is shown in the first column of Figure 5.6 and consecutive columns show the results of various methods in the literature. The last column (F), (F1) and (F2) shows the result of the FOEF. The FOEF performs better compared to the other methods, in all the different input noise levels.

Figure 5.7 shows enlarged portions (textured and homogeneous regions) of the image "Lena", "Woman" and "Boat" after applying various enhancement methods. Two portions from the image "Lena" and one portion each from image "Woman" and "Boat" are enlarged for a better visibility. The first row shows a highly textured region taken from the image "Lena" and the second one shows a smooth gray level portion from the same image. The third and fourth rows display smooth and partially textured portions of images "Woman" and "Boat", respectively. The first column in Figure 5.7, shows the portions of the original image. The second column shows the distorted input image and subsequent columns show the image (portions) after

applying various filtering methods. The third column in this figure is the result of Alvarez model (Alvarez and Mazorra 1994). In this particular output image; shown in the second column of Figure 5.7, one can notice that even though the edges are enhanced the noise features are still present in the filtered output. The reason is; in Alvarez model the shock component will be active right from the initial stages of the filtering process and this will result in enhancing the noise components along with the edges. The fourth to sixth columns in Figure 5.7 are the results of the methods You-Kaveh (You and Kaveh 2000), Tai (Lysaker et al. 2003) and Hajiaboli (Hajiaboli 2010), respectively. In all these results one fact is evident: the images are denoised at the cost of weakening the edges. In the FOEF (the output is shown in the last column of Figure 5.7) the noise features are considerably removed, because the time dependent function inside the shock term suppresses the effect of shock in the earlier stages of evolution; consequently the noise features gets only diffused during the early stages of evolution process. The edges are enhanced well and noise features are removed considerably in the FOEF.

The optimal number of iterations n [1] for each method at a given noise level (here we have chosen the SNR of initial noisy image as 8dB) is decided based on the SNR values. The iteration number corresponding to the optimal SNR value is taken as the optimal iteration number. The graph in Figure 5.8 shows a plot of SNR against the number of iterations for the image "Phantom", the change in SNR with the number of iterations follow the same characteristics for other input images as well. Hence, we only tabulate the optimal number of iterations corresponding to each SNR value for different input images. The optimal iteration numbers obtained based on the SNR values are shown in Tables 5.1, 5.2, 5.3 and 5.4, for the input test images "Phantom","Lena", "Woman" and "Boat", respectively. All the images shown in Figures 5.1, 5.2, 5.3, 5.4 and 5.5 are taken after the corresponding optimal number of iterations.

Table 5.1: The optimal number of iterations for different methods for various noise levels (SNR in dB) for the image "Phantom".

METHODS	SNR=6dB	SNR=7dB	SNR=8dB	SNR=9dB	SNR=10dB
You Kaveh	150	140	135	130	126
Hajiaboli	120	111	104	96	90
Proposed Method (FOEF)	61	52	43	36	31

[1]The iteration number chosen to get optimal performance.

Table 5.2: The optimal number of iterations for different methods for various noise levels (SNR in dB) for the image :"Lena".

METHODS	SNR=6dB	SNR=7dB	SNR=8dB	SNR=9dB	SNR=10dB
You Kaveh	250	235	208	200	190
Hajiaboli	220	205	190	178	170
Proposed Method (FOEF)	120	110	102	89	80

Table 5.3: The optimal number of iterations for different methods for various noise levels (SNR in dB) for the image :"Woman".

METHODS	SNR=6dB	SNR=7dB	SNR=8dB	SNR=9dB	SNR=10dB
You Kaveh	230	225	200	190	178
Hajiaboli	210	200	191	180	168
Proposed Method (FOEF)	109	100	92	81	70

We recall from Chapter 2, the NRRMSE shows the accuracy of the method to properly reconstruct images. During the diffusion process NRRMSE keeps on decreasing as the solution image approaches the original one. From Figure 5.9 one can notice that, NRRMSE corresponding to the FOEF is decreasing initially and then it is increasing after some iterations, whereas, for Alvarez model NRRMSE first increases and then it decreases, this effect is due to the shock component present in the filter. In the FOEF the shock will not have significant contribution during the initial stages of evolution therefore, only diffusion will happen, this causes the NRRMSE to decrease considerably during the initial stages of evolution whereas, in Alvarez model the shock will be dominant even during the initial stages of evolution. This causes the NRRMSE to increase for first few iterations and then decrease, thereafter.

The Pratt's Figure of Merit (FOM) for the images "Phantom" and "Lena" filtered using different filters (including the FOEF), for various SNR values of the input noisy image are plotted in the graph given in Figures 5.10 and 5.11, respectively. The number of iterations for each method (at various SNR values) for the images "Phantom" and "Lena" are selected based on Table 5.1 and 5.2, respectively. From these graphs one can observe that the edge preserving capacity of the FOEF is better compared to the other methods. The results of applying the Canny edge detector (with $\sigma = 0.1$) on images filtered using various method are shown in Figure 5.12. Figure 5.12 A shows the result of edge detection method applied on the original image. Figure 5.12 B shows the result for blurred and noisy image. Figure 5.12 C-5.12 F shows the results

Table 5.4: The optimal number of iterations for different methods for various noise levels (SNR in dB) for the image :"Boat".

METHODS	SNR=6dB	SNR=7dB	SNR=8dB	SNR=9dB	SNR=10dB
You Kaveh	240	235	220	201	188
Hajiaboli	221	202	185	176	168
Proposed Method (FOEF)	119	107	96	88	79

of the edge detection method applied on the filtered outputs of various methods. The edges detected for the image filtered using the FOEF (shown in Figure 5.12 G) are more robust than that of the other methods (shown in Figure 5.12 C-5.12 F).

Similarly the structural similarity index measured for the images "Phantom" and "Lena" filtered using different methods (including the proposed one), for various SNR values of the input noisy image are plotted in the graph given in Figures 5.13 and 5.14, respectively. The number of iterations for each method (at various SNR values) are selected based on Table 5.1 and 5.2 for images "Phantom" and "Lena", respectively. From these figures it could be easily verified that the FOEF has good contrast, illumination and the structure preserving capabilities as compared to the other methods.

From all the measures described above we have experimentally (both visually and quantitatively) demonstrated that the FOEF enhances the contrast, texture and edge features present in the image, while reducing the noise effectively. Figures shown in favor of the FOEF especially the one that enlarged the constant intensity portion gives a clear understanding that the proposed method does not contaminate the constant intensity regions with small intensity patches (that causes a visual discrepancy).

Please note that, the quality measures are not provided explicitly for the images "Woman", "Boat" and "hibiscus" for the reason that, the measures are similar in characteristic to the image "Lena" (all these images fall into the category of partially textured natural image).

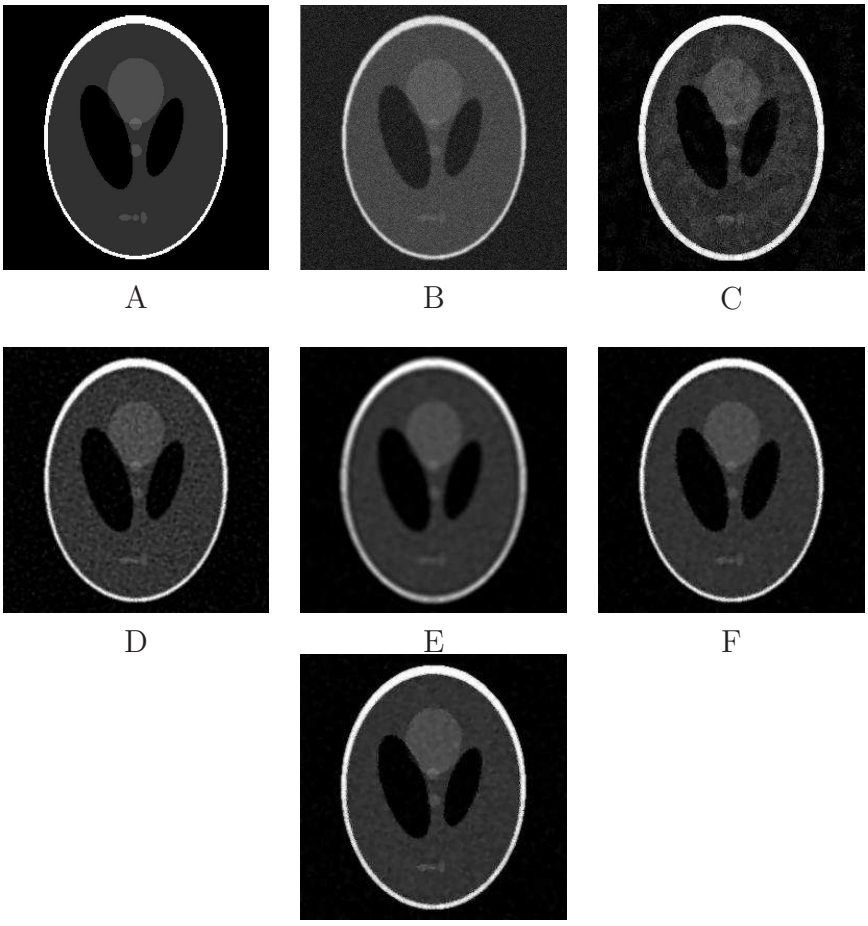

Figure 5.1: Image "Phantom":(A) Original image; (B) Blur and noisy image (out of focus blur: SNR 8dB); (C) After Applying Second-order shock proposed by Alvarez and Mazorra (1994); (D) After applying Fourth-order method proposed by You and Kaveh (2000); (E) After applying Fourth-order method proposed by Lysaker et al. (2003); (F) After applying method by Hajiaboli (2010); (G) After applying the FOEF Method.

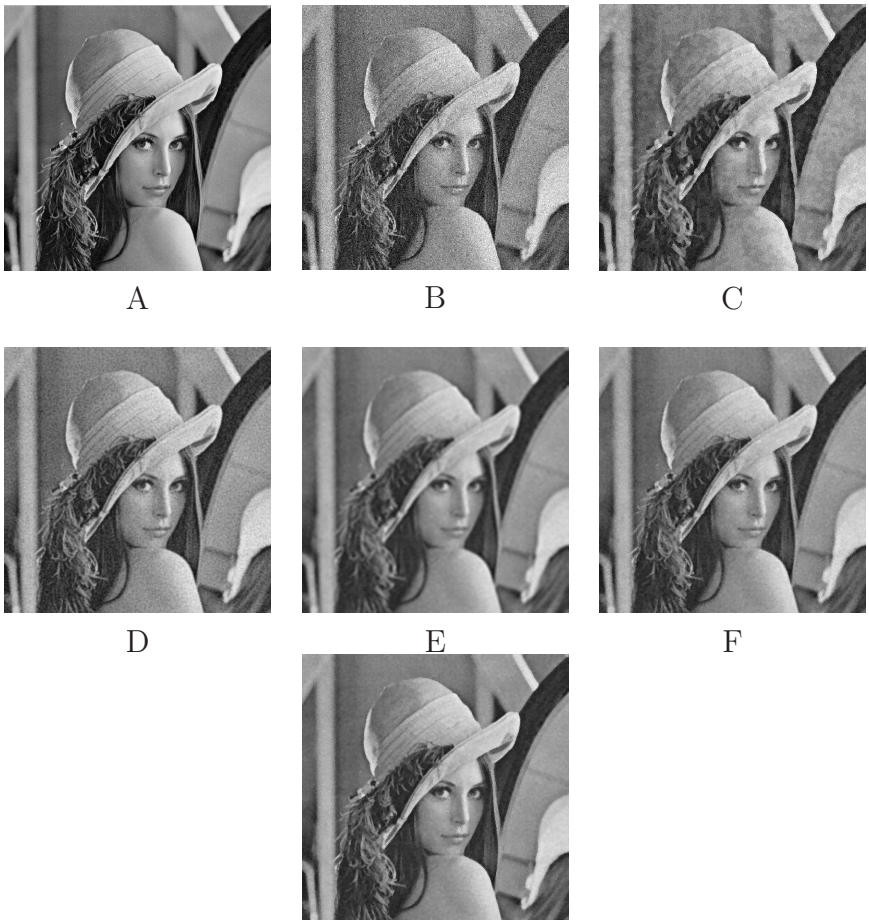

Figure 5.2: Image "Lena":(A) Original image; (B) Blur and noisy image (out of focus blur: SNR 8dB); (C) After Applying Second-order shock proposed by Alvarez and Mazorra (1994); (D) After applying Fourth-order method proposed by You and Kaveh (2000); (E) After applying Fourth-order method proposed by Lysaker et al. (2003); (F)After applying method by Hajiaboli (2010); (G) After applying the FOEF Method.

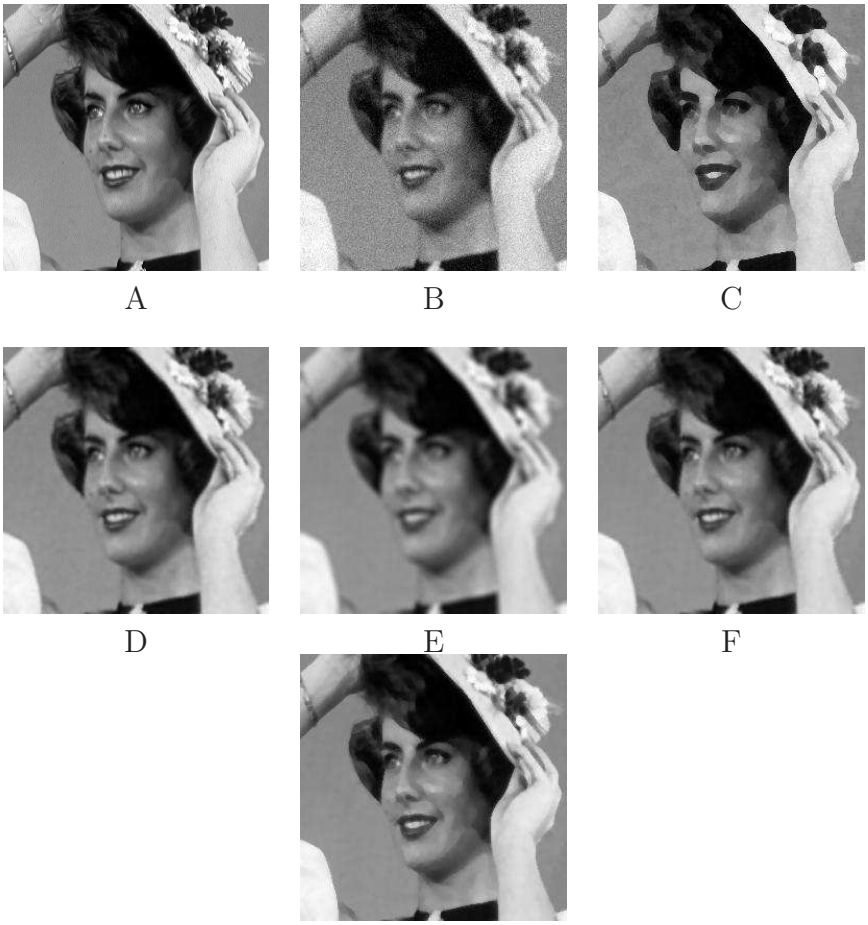

Figure 5.3: Image "Woman":(A) Original image; (B) Blur and noisy image (out of focus blur: SNR 8dB) (C) After Applying Second-order shock proposed by Alvarez and Mazorra (1994); (D) After applying Fourth-order method proposed by You and Kaveh (2000); (E) After applying Fourth-order method proposed by Lysaker et al. (2003); (F)After applying method by Hajiaboli (2010); (G) After applying the FOEF Method.

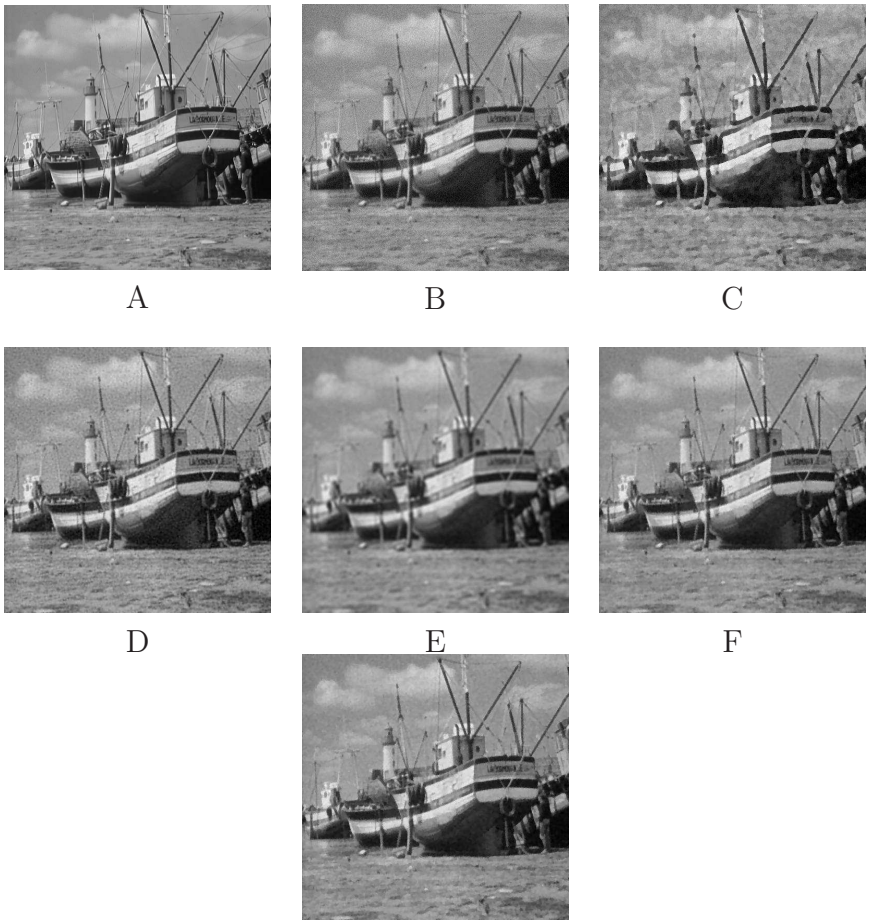

Figure 5.4: Image "Boat":(A) Original image; (B) Blur and noisy image (out of focus blur: SNR 8dB) (C) After Applying Second-order shock proposed by Alvarez and Mazorra (1994); (D) After applying Fourth-order method proposed by You and Kaveh (2000); (E) After applying Fourth-order method proposed by Lysaker et al. (2003); (F)After applying method by Hajiaboli (2010); (G) After applying the FOEF.

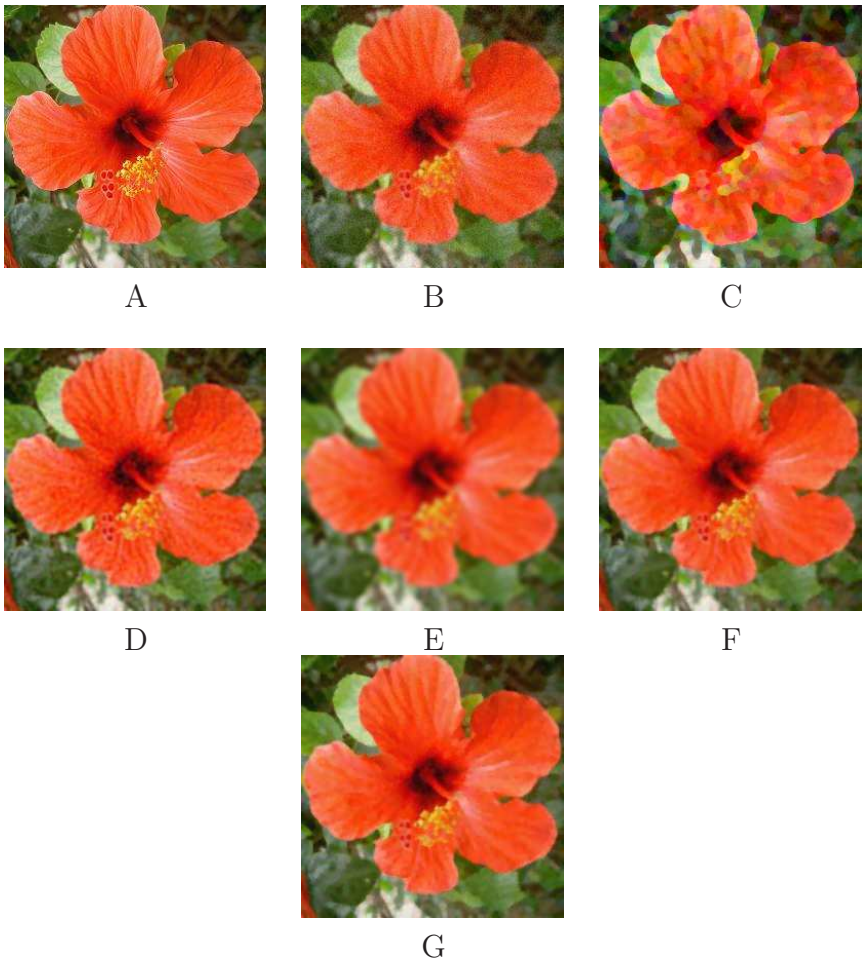

Figure 5.5: Image "hibiscus":(A) Original image; (B) Blur and noisy image (out of focus blur: SNR 8dB); (C) After Applying Second-order shock proposed by Alvarez and Mazorra (1994); (D) After applying Fourth-order method proposed by You and Kaveh (2000); (E) After applying Fourth-order method proposed by Lysaker et al. (2003); (F) After applying method by Hajiaboli (2010); (G) After applying the FOEF Method.

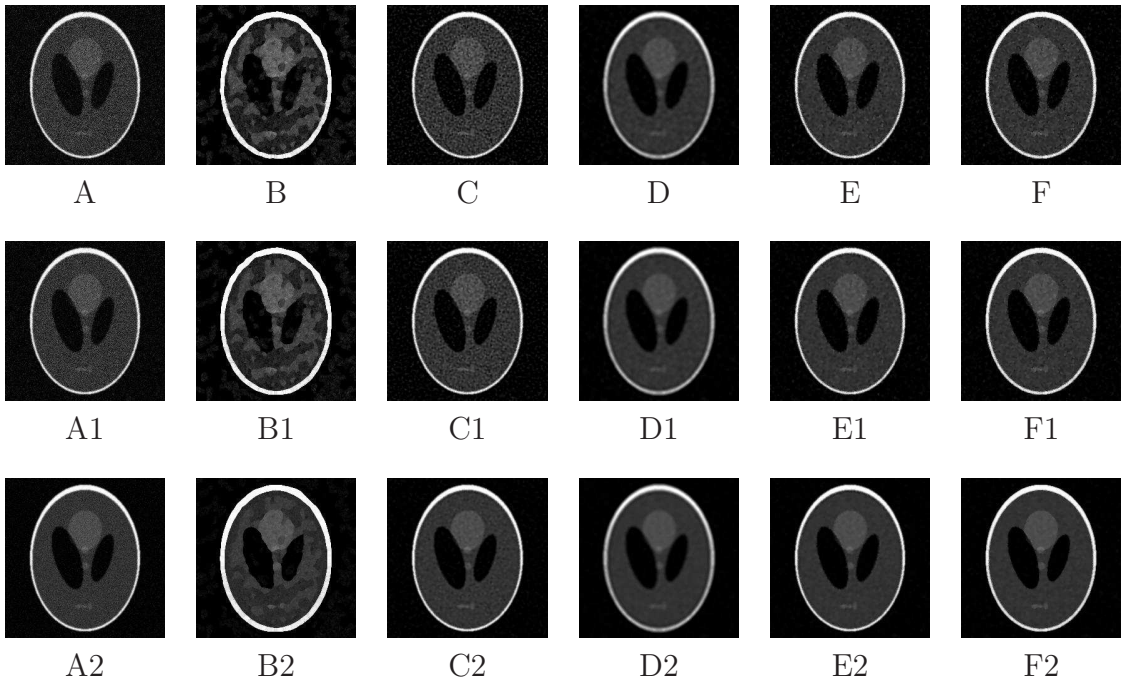

Figure 5.6: Filtered results at different noise levels:(A), (A1) & (A2) The blur-noisy image with SNR 6dB, 7dB and 9dB, respectively; (B), (B1) & (B2) After Applying Second-order shock proposed by Alvarez and Mazorra (1994); (C), (C1) & (C2) After applying Fourth-order method proposed by You and Kaveh (2000); (D), (D1) & (D2) After applying Fourth-order method proposed by Lysaker et al. (2003); (E), (E1) & (E2) After applying method by Hajiaboli (2010); (F), (F1) & F(2) After applying the FOEF.

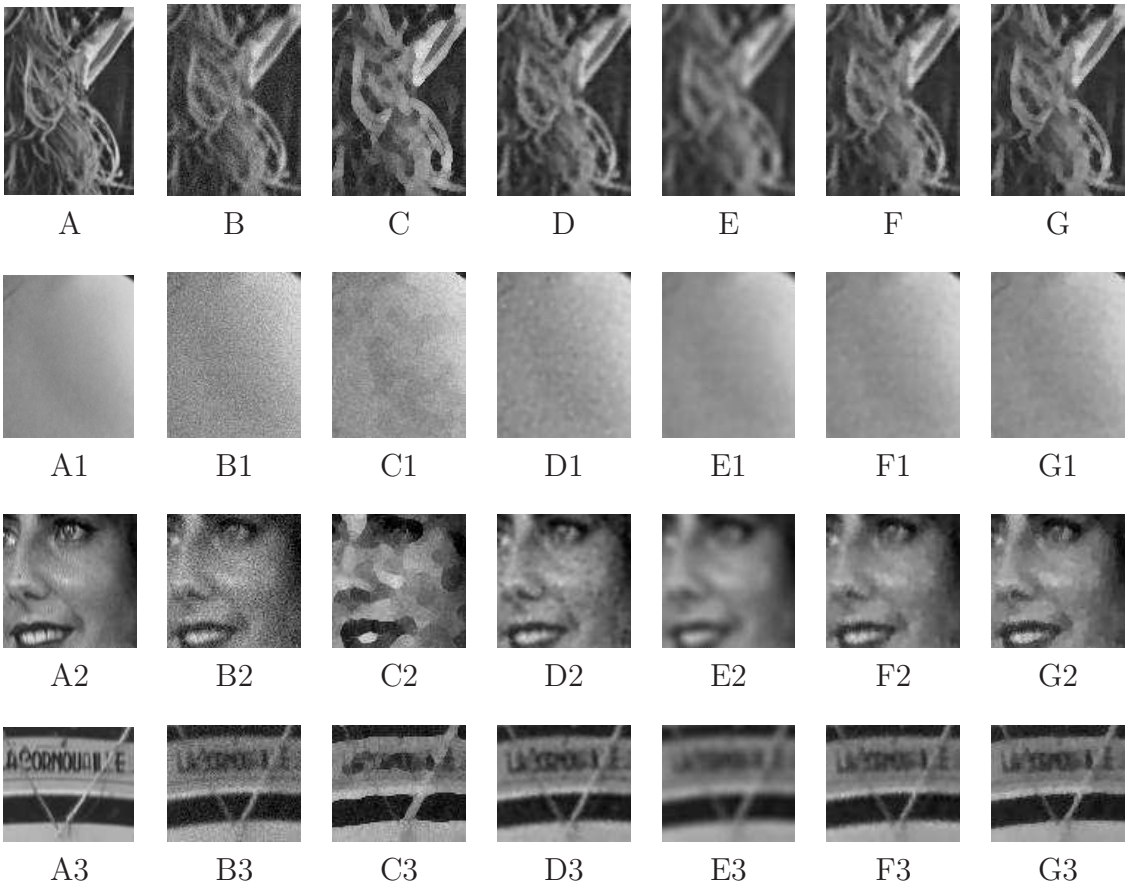

Figure 5.7: The enlarged portions of the images "Lena", "Woman" and "Boat", filtered with different methods: A, A1, A2 & A3 Original images; B, B1, B2 & B3 Noisy Image; C, C1, C2 & C3 Alvarez model; D, D1, D2 & D3 Method in You and Kaveh (2000); E, E1, E2 & E3 Method in Lysaker et al. (2003); F, F1, F2 & F3 Method in Hajiaboli (2010);G, G1, G2 & G3 The FOEF.

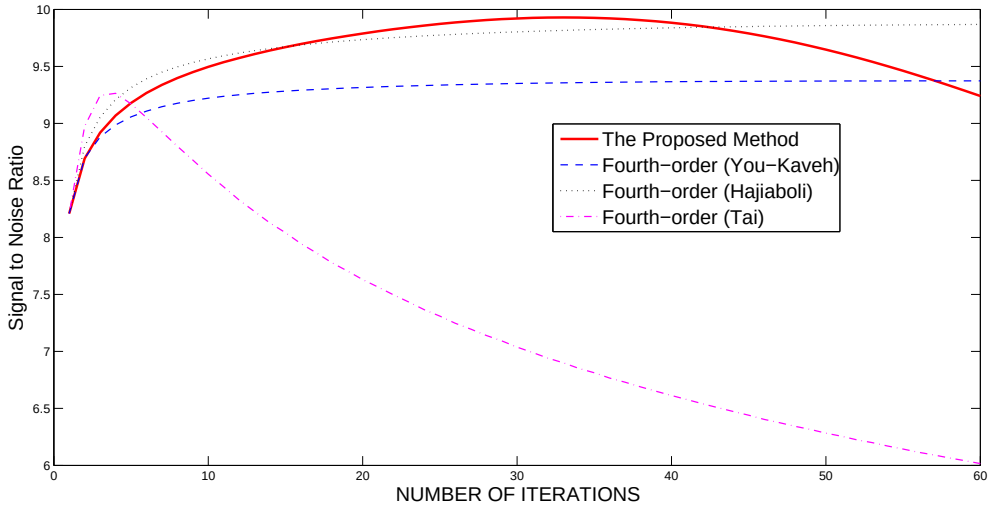

Figure 5.8: The Signal-to-Noise Ratio (SNR) plotted in each iterations for the image "Phantom": SNR of the initial noisy image 8dB.

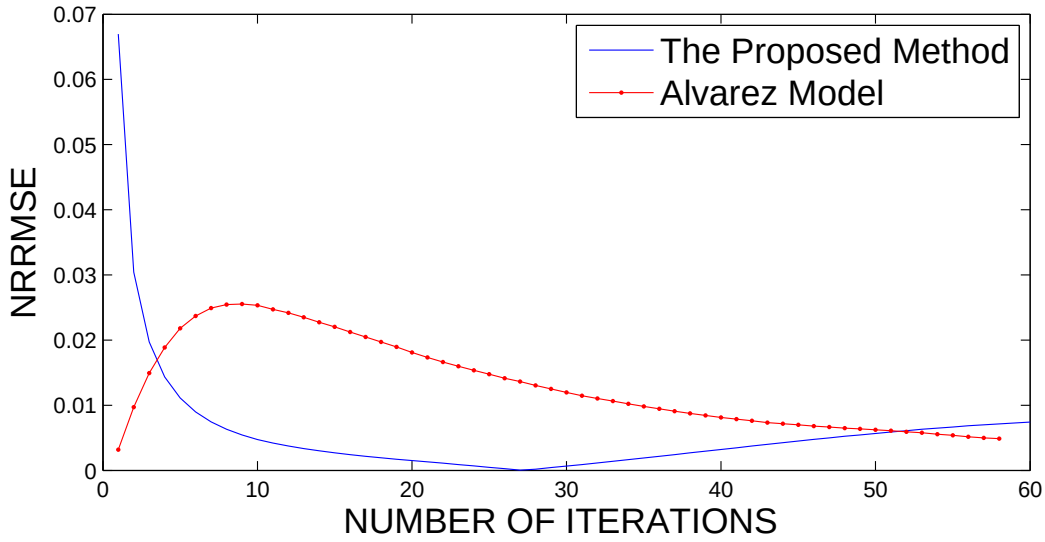

Figure 5.9: Normalized Root Mean Square Error plotted against the number of iterations for various methods including the proposed (FOEF) one for the image "phantom" (SNR of the noisy image is 10dB).

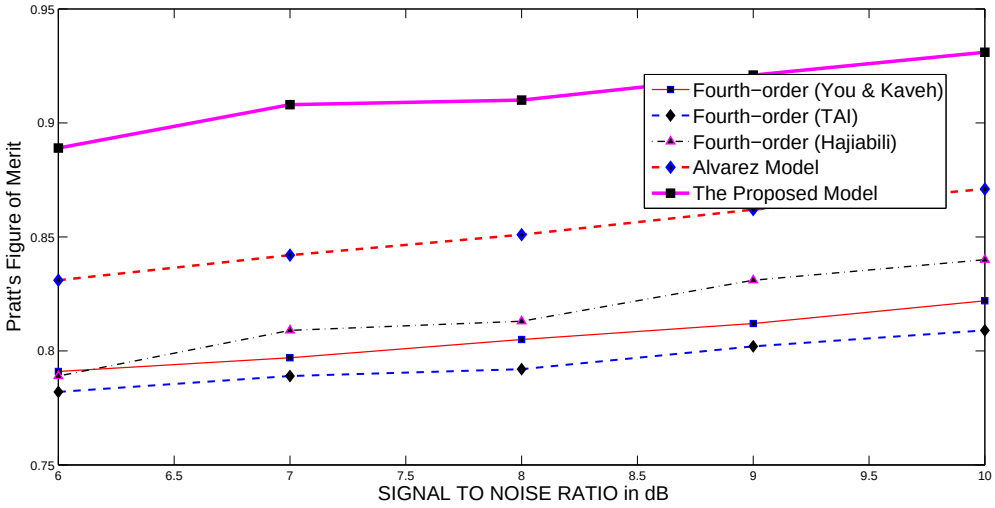

Figure 5.10: Pratt's Figure of Merit (FOM) plotted for different SNR values (in dB) of the noisy image (Image: "Phantom").

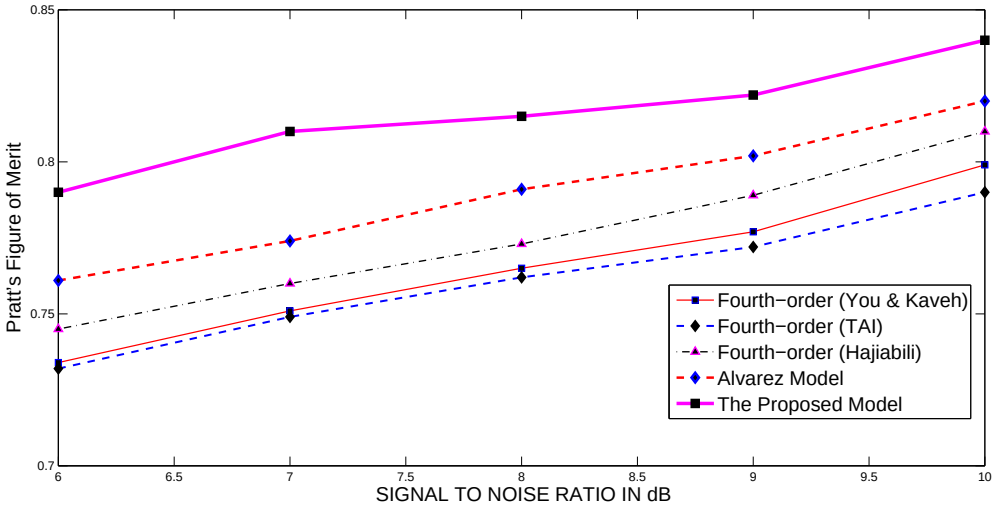

Figure 5.11: Pratt's Figure of Merit (FOM) plotted for different SNR values (in dB) of the noisy image (Image: "Lena").

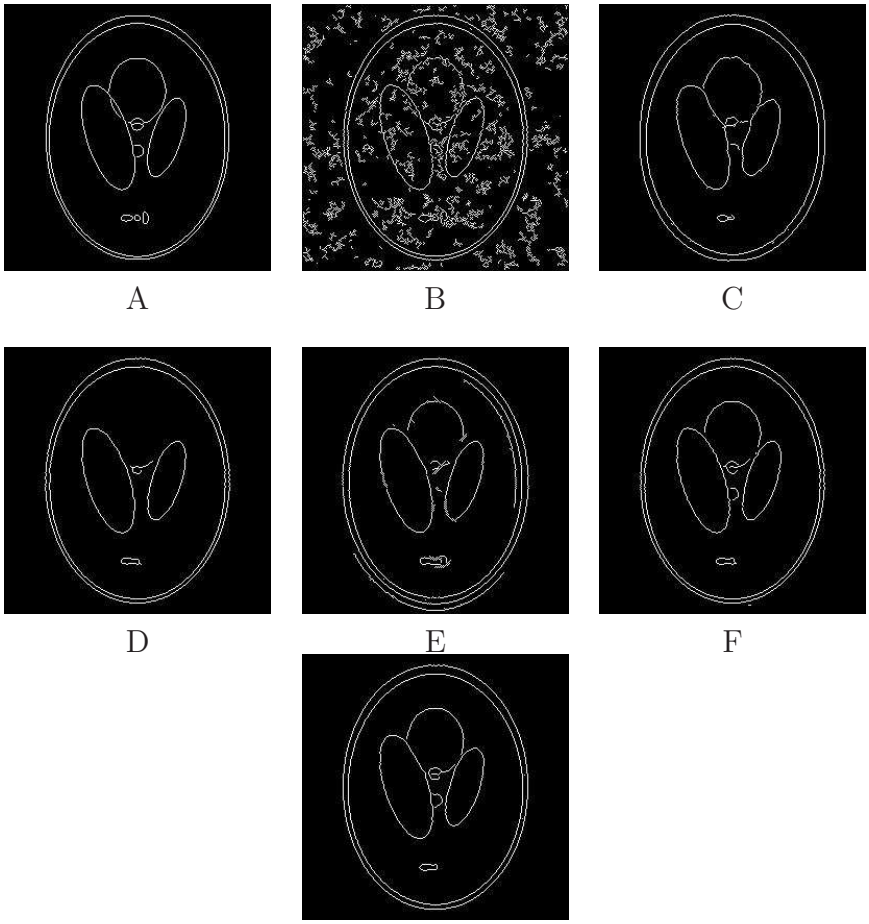

Figure 5.12: Result of canny edge detector applied on "Phantom" after filtering with various methods :(A) Original image; (B) Blur and noisy image (out of focus blur: SNR 8dB); (C) Alvarez Model; (D) You and Kaveh (2000) Method; (E) Model in Lysaker et al. (2003); (F) Hajiaboli (2010) Model; (G) FOEF Model.

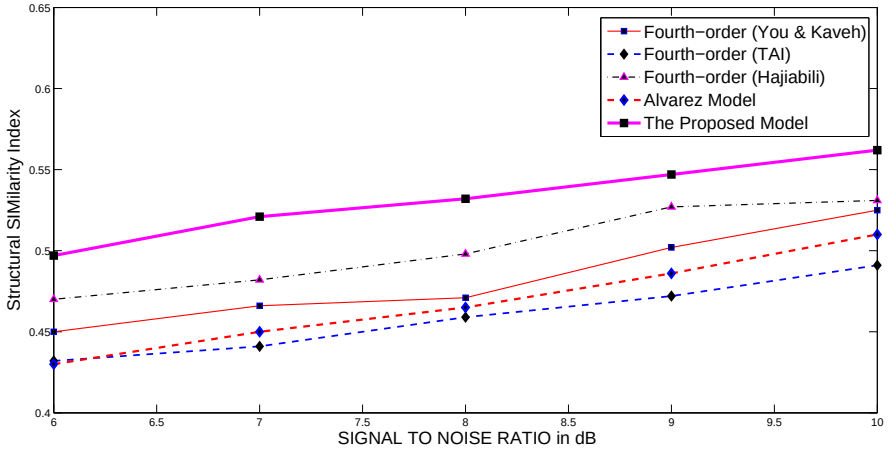

Figure 5.13: Structural Similarity Index (SSIM) plotted for different SNR values (in dB) of the noisy image (Image: "Phantom").

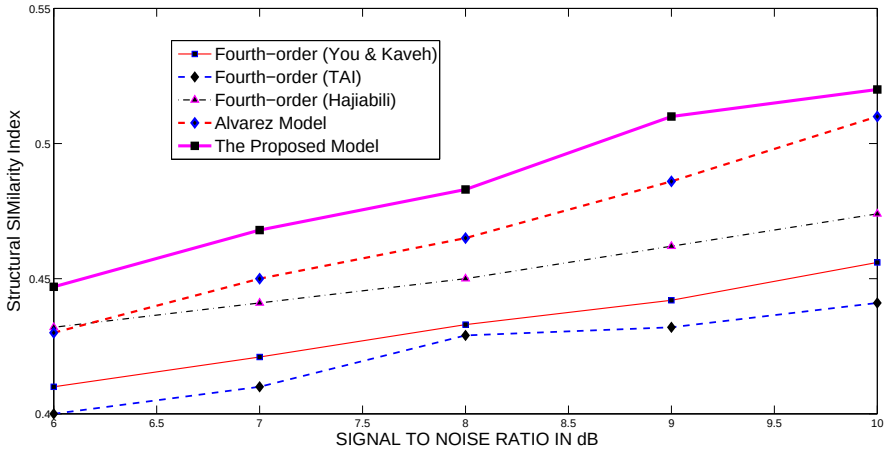

Figure 5.14: Structural Similarity Index (SSIM) plotted for different SNR (in dB) values of the noisy image (Image: "Lena").

Chapter 6

CONCLUDING REMARKS AND FUTURE WORKS

In this thesis we have proposed three image enhancement methods and one image inpainting method based on variational/PDE approaches. These methods are generalized PDE solutions to both images and signals. Though we have presented the results in terms of natural images these filters can very well be applied for special kinds of images used for medical or satellite applications. These PDE's are generalized frameworks for image enhancement and they can be modified for specialized purpose based on the application under consideration.

6.1 FEATURES OF THE FILTERS PROPOSED IN THE THESIS

In Chapter 2 we have introduced a time-dependent anisotropic diffusion model for image restoration. The model attains a stable state at a faster rate as compared to other models in the literature for image enhancement. This model diffuses isotropically in the constant-intensity areas and anisotropically in the areas dominated by edges and finer details. The response of the filter is analyzed using different kinds of images having different magnitudes of high oscillatory features. And the filter is found capable of preserving and enhancing edges and other high frequency information present in the input images. Furthermore, the filter is applied on vector-valued (color) images as well. The results shown in the the result section of this chapter clearly demonstrate

the capacity of the filter to properly enhance textured, partially textured, constant-intensity and color images with utmost attention to the edge and finer details (while denoising them). The behavior of the method is analyzed for different parameters used for fine-tuning the performance of the filter. Under the various conditions mentioned above, the filter is found to behave robustly in reconstructing the images. Finally, the quantitative and qualitative results are in favor of the claim that the proposed method deblurs and denoises the images very well, as compared to the other enhancement methods considered in this chapter.

In Chapter3 we proposed a modification to the existing diffusion coupled shock filter in Alvarez and Mazorra (1994). This proposed filter results in enhancing some of the important edges present in images when a denoising is performed. The method makes use of Gauss curvature for driving the diffusion process. This will result in preserving the features with non-zero mean curvature values and the shock term present in the filter enhances the edge features and finer details present in the images. A time dependent function is introduced in the shock term of the filter to appropriately control the extend of shock and diffusion during various stages of evolution. The comparative results in terms of quantitative and qualitative measurements are provided in the result section of this chapter. The proposed filter is found effective in preserving curvy edges and corners present in the input images as evident from the provided results.

In Chapter 4 a third-order Gauss curvature driven diffusion method is introduced for image inpainting/reconstruction. This method inpaints the desired image domain preserving the curvy edges and corners present in the images. In the non-inpainting domain this filter acts like a normal TV based diffusion filter. This method would be useful when the inpainting domain consist of many curvy edges and corners. The method is devised for handling blurred and noisy images. Therefore, this method can restore the images from their blurred and noisy observation along with inpainting the desired domain. The results shown in favour of the proposed method substantially highlights the capability of the filter to preserve curvy structures present in the images.

In Chapter 5 a fourth-order anisotropic diffusion cum shock filter is proposed. The proposed method can enhance the semantic features like edges, finer details and textures, while denoising the images. The filter proposed here employs a planar approximation instead of piece-wise approximation resulting is a natural outlook to the filtered image. The denoising and enhancing capacity of the filter is controlled using a

positive scalar regularization parameter. The anisotropic nature of the filter is managed by a diffusion coefficient function, defined using an absolute value of the gradient image. The diffusion coefficient function controlled by the absolute gradient image, catalyzes the diffusion process, helping in attaining the solution state at a faster rate, when compared to many other prominent fourth-order methods in the literature. The proposed filter preserves the planar approximation, thereby reducing the chance of a *staircase* effect as in the second order methods that uses a piece-wise constant approximation. The iteration process is controlled using the SNR values in each iteration. The evolution proceeds as long as the SNR increases monotonically and stops at point when it decreases. Since, the iteration process is controlled dynamically the optimal results are obtained. The method proposed in this chapter is compared with all the relevant image enhancement methods in the literature using the visual results and widely used statistical qualitative measures like SNR, Pratt's FOM and MSSIM. The pictorial and tabulated measures are highly in favor of the proposed method. The proposed method is tested for both textured and non-textured images (including artificial and natural images) at various noise variances and the experimental results provided substantially proves the efficiency and effectiveness of the proposed method.

All the proposed filters (detailed in chapters 2, 3, 4 and 5) are implemented using MATLAB 7.9.0.529 (R2009b) (for 32-bit glinx86), tested and compared with the relevant state-of-the art techniques for image enhancement. The pros and cons of each filter is analyzed and the applicability of the concerned filter is demonstrated with different input images with various kinds of image features. A detailed analysis and experimentation on the filters were provided in the respective chapters.

6.2 SCOPES FOR FUTURE WORK

Image restoration, enhancement, inpainting etc. are inverse problems. Their solutions always demand a scope for further improvement. The main idea of the regularization methods is to reduce the approximation error [1]. In fact it is hard to devise an approximation method which nullifies this error. Therefore, there is always a scope for doing a further refinement on the existing methods in terms of accuracy and performance.

[1]The absolute difference between observed and actual data.

6.2.1 Improvements to the methods proposed in the thesis

In Chapter 2 we had introduced a switching model which switches the norm from L^2 to TV and vice-versa based on the image features like textures and constant intensity regions. It was further proposed in Blomgren et al. (1997) to incorporate an adaptive p norm which gets adapted based on the image features. In this way the one can make the norm adapting to each pixel value instead of a scalar value for the whole image. This could improve the visual results. However, the time complexity is more for this approach. We need to calculate the *p-norm* value for each pixel in each iteration of the diffusion process. A possible modification is to frame the regions into different non-overlapping tiles and calculate a *p-norm* for each tiled region. This could improve the performance by restricting the number of computations to the number of windows (instead of number of pixels) for calculating the p norm. Moreover, the frame based method is more logical than pixel based method, because the semantic features lie over more than a few number of pixels so associating a single norm for the whole frame/tile will give better justification. This work is under progress. Furthermore, it is quite natural to improve the algorithm in terms of computation complexity by adopting more sophisticated iterative schemes. We have adopted explicit time marching scheme instead of this one can adopt implicit schemes as well.

Curvature driven diffusion/inpainting model

One of the trivial improvements would be adoption of sophisticated computation schemes to speed-up the computation process. Another substantial improvement is incorporating the transport process described in Bertalmio et al. (2000) into the Gauss curvature driven inpainting method this could improve the performance of inpainting process in terms of accuracy and visual impressiveness. We have analyzed the mathematical aspects of this new filter and the work is in the final stage. Though we have mainly focused on curvature driven methods for image inpainting, there are quite a few avenues still to be explored in digital image inpaiting.

Higher-order diffusion schemes

Finally, it is widely known that as the order of diffusion process increases the accuracy of approximation fades out. So the higher-order diffusion processes may not give better results as compared to the second-order diffusion process. However, we have reformulated the ordinary fourth-order diffusion methods to address this issue by incorporating the shock component. Further improvements can be done for the fourth-order methods in terms of computational speedup and visual accuracy.

Appendix I
DERIVATIONS, PROOFS AND MATLAB IMPLEMENTATION

A-1 THE EULER-LAGRANGE EQUATIONS

The general problem (assuming a single independent variable) is to find the function $y(x)$, that makes the following integral stationary (i.e., derivative vanishes):

$$I = \int_{x_1}^{x_2} F(x, y, y')dx. \tag{A.1}$$

Here F is a definite functional defined over the range x_1 and x_2. The starting point is to represent the infinite set of curves passing through the given endpoints that differ from the extremal curve by "small" amounts. These curves, $Y(x)$, are represented by perturbing the extremal curve, $y(x)$, by a function $\eta(x)$ that is zero at x_1 and x_2 and is arbitrary between the endpoints.

$$Y(x) = y(x) + \epsilon\eta(x), \tag{A.2}$$

where ϵ is a small positive scalar value. Differentiating (A.2) with respect to x yields:

$$Y'(x) = y'(x) + \epsilon\eta'(x). \tag{A.3}$$

It is assumed that $Y(x)$ is C^2 continuous ($y''(x)$ is continuous). Now the problem is to make $I(\epsilon)$ stationary when $\epsilon = 0$, formally:

$$\frac{dI(\epsilon)}{d\epsilon} = 0, \ when \ \epsilon = 0, \tag{A.4}$$

where

$$I(\epsilon) = \int_{x_1}^{x_2} F(x, Y, Y')dx. \tag{A.5}$$

Differentiating (A.5) with respect to ϵ yields,

$$\frac{dI(\epsilon)}{d\epsilon} = \int_{x_1}^{x_2} \left(\frac{\partial F}{\partial Y}\frac{dY}{d\epsilon} + \frac{\partial F}{\partial Y'}\frac{dY'}{d\epsilon} \right) dx. \tag{A.6}$$

Substituting the derivatives of (A.1) and (A.2) wrt ϵ and setting the result to zero at $\epsilon = 0$ yields:

$$\left(\frac{dI(\epsilon)}{d\epsilon} \right)_{\epsilon=0} = \int_{x_1}^{x_2} \left(\frac{\partial F}{\partial Y}\eta(x) + \frac{\partial F}{\partial Y'}\eta'(x) \right) dx = 0. \tag{A.7}$$

Since we consider $\epsilon = 0$, thus $Y = y$

$$\left(\frac{dI(\epsilon)}{d\epsilon} \right)_{\epsilon=0} = \int_{x_1}^{x_2} \left(\frac{\partial F}{\partial y}\eta(x) + \frac{\partial F}{\partial y'}\eta'(x) \right) dx = 0. \tag{A.8}$$

Given the assumption that $y(x)$ is C^2 continuous, the second term of the integrand of (A.8) can be integrated using integration by parts:

$$\begin{aligned}
\left(\frac{dI(\epsilon)}{d\epsilon} \right)_{\epsilon=0} &= \int_{x_1}^{x_2} \frac{\partial F}{\partial y}\eta(x)dx + \left(\frac{\partial F}{\partial y'}\eta(x)|_{x_1}^{x_2} - \int_{x_1}^{x_2} \frac{d}{dx}\frac{\partial F}{\partial y'}\eta(x)dx \right) \\
&= \int_{x_1}^{x_2} \frac{\partial F}{\partial y}\eta(x)dx + \left(0 - \int_{x_1}^{x_2} \frac{d}{dx}\frac{\partial F}{\partial y'}\eta(x)dx \right) \\
&= \int_{x_1}^{x_2} \left(\frac{\partial F}{\partial y}\eta(x) - \frac{d}{dx}\frac{\partial F}{\partial y'}\eta(x) \right) dx \\
&= \int_{x_1}^{x_2} \left(\frac{\partial F}{\partial y} - \frac{d}{dx}\frac{\partial F}{\partial y'} \right) \eta(x)dx.
\end{aligned} \tag{A.9}$$

Since $\eta(x)$ is an arbitrary function, this forces the integrand within the brackets to equal zero, i.e:

$$\frac{\partial F}{\partial y} - \frac{d}{dx}\frac{\partial F}{\partial y'} = 0. \tag{A.10}$$

Figure A.1: The direction of vectors

The equation in (A.10) is known as the **Euler Lagrange** equation. In general for a functional

$$E(u) = \int_{\Omega} \phi(|\nabla u|) dx dy, \tag{A.11}$$

the minimum of the functional exists at a point u, if it satisfies the Euler-Lagrange Equation:

$$div\left(\frac{\phi'(|\nabla u|)}{|\nabla u|}\nabla u\right) = 0, \tag{A.12}$$

where $\phi'(.)$ stands for the first order derivative of the function $\phi(.)$. The derivation of above Euler-Lagrange equation is skipped for brevity.

The decomposition of the expression in (A.12) in terms of tangent and normal vectors can be written as:

$$\frac{\phi'(|\nabla u|)}{|\nabla u|} U_{TT} + \phi''(|\nabla u|) U_{NN} = 0, \tag{A.13}$$

where U_{TT} and U_{NN} are the vectors in tangent and normal directions, respectively. Precisely for any point $x \in \mathbb{R}^2$, where $|\nabla u| = 0$, we can define the vectors $N(x)$ and $T(x)$, which are normal and tangent to the level-curve as: $T(x) = \frac{\nabla u(x)}{|\nabla u(x)|} = \frac{1}{|\nabla u|} \times (u_x, u_y)$, where u_x and u_y are the first order derivatives of u in the direction x and y respectively and $N(x)$ is the tangent vector perpendicular to $T(x)$ i.e. $N(x) = \frac{1}{|\nabla u|} \times (-u_y, u_x)$. See Figure A.1 for details.

E-L equations for the functionals used in this thesis:

TV functional:

$$E(u) = \int_{\Omega} |\nabla u|_{TV} dx dy. \tag{A.14}$$

Here the functional can be written as $\phi(|\nabla u|) = |\nabla u|$, or in general $\phi(x) = x$ where $x = |\nabla u|$. Therefore, $\phi'(x) = 1$ or $\phi'(|\nabla u|) = 1$ and $\phi''(x) = 0$. With the help of (A.12), we can write (A.14) as:

$$0 = div\left(\frac{1}{|\nabla u|}\nabla u\right)$$

or

$$0 = \frac{1}{|\nabla u|}U_{TT} + 0 \times U_{NN}.$$

Tikhnov Functional:

$$E(u) = \int_{\Omega} |\nabla u|^2_{\mathcal{L}^2} dxdy. \tag{A.15}$$

Here the functional can be written as $\phi(|\nabla u|) = |\nabla u|^2$, or in general $\phi(x) = x^2$ where $x = |\nabla u|$. Therefore, $\phi'(x) = 2x$ or $\phi'(|\nabla u|) = 2|\nabla u|$ and $\phi''(x) = 2$. With the help of (A.12), we can write (A.15) as:

$$\begin{aligned} 0 &= div\left(\frac{|\nabla u|}{|\nabla u|}\nabla u\right) \\ \implies 0 &= \nabla u.(\nabla u) \\ \implies 0 &= \nabla^2 u \end{aligned}$$

or

$$0 = U_{TT} + U_{NN}$$

A-2 MATLAB IMPLEMENTATION FOR PERONA-MALIK FILTER

```
==========================================================
function [Oimg]=SecNLFilter(Iimg)

%%%%%%%%%%%%%%%%%%%%%%%%%%%%%%%%%%%%%%%%%%%%%%%%%%%%
%% Parameters Iimg: Input image
%% Oimg: Output image
%% The function inputs the filterd image
%%Perona-Malik Equation du/dt=div(c(|del u| del u)
%%Neumann boundary is assumed
%%%%%%%%%%%%%%%%%%%%%%%%%%%%%%%%%%%%%%%%%%%%%%%%%%%%
  u0=im2double(Iimg);
  dt=0.2; %time step
  K=0.03; %contrast parameter
  std_n=0.04;
  randn('seed',1296);
  noise=randn(size(u0))*std_n;
  u=u0+noise;
  n_iter=10;
  for i=1:n_iter
    gU=grad(u);
    mod_gU=sqrt(gU(:,:,1).^2+gU(:,:,2).^2);
    c_delu=1./(1+(mod_gU.^2./K^2));
    u=u+dt*div(repmat(c_delu,[1 1 2]).*gU);
  end
  Oimg=u;
end

function [dfx]=div(Px)

%%%%%%%%%%%%%%%%%%%%%%%%%%%%%%%%%%%%%%%%%%%%%%%%%%%%%%%%%%%%%%%%%
%% Function to find the divergance of a vector field
```

```
%% Px: vector component along x and Py vector component along y
%% dfx divergance of the vector field
%%%%%%%%%%%%%%%%%%%%%%%%%%%%%%%%%%%%%%%%%%%%%%%%%%%%%%%%%%%%%%%%%%%%%%%

  Py = Px(:,:,2);
  Px = Px(:,:,1);
  fx = Px-Px([1 1:end-1],:,:);
  fy = Py-Py(:,[1 1:end-1],:);
  fy(:,1,:)   = Py(:,1,:);    % boundary
  fy(:,end,:) = -Py(:,end-1,:);
  fx(1,:,:)   = Px(1,:,:);        % boundary
  fx(end,:,:) = -Px(end-1,:,:);
  dfx=fx+fy;
end
%-----------------------------

function [fx]=grad(M)

%%%%%%%%%%%%%%%%%%%%%%%%%%%%%%%%%%%%%%%%%%%%%%%%%%%%%%%%%%%%%%%%%%%%%%%
%% Function to find the gradient
%% fx(:,:,1) Gradient along x and fx(:,:,2) Gradient along y
%%%%%%%%%%%%%%%%%%%%%%%%%%%%%%%%%%%%%%%%%%%%%%%%%%%%%%%%%%%%%%%%%%%%%%%

  fx = ( M([2:end end],:,:)-M([1 1:end-1],:,:) )/2; % boundary
  fx(1,:,:) = M(2,:,:)-M(1,:,:);
  fx(end,:,:) = M(end,:,:)-M(end-1,:,:);
  fy = ( M(:,[2:end end],:)-M(:,[1 1:end-1],:) )/2;  % boundary
  fy(:,1,:) = M(:,2,:)-M(:,1,:);
  fy(:,end,:) = M(:,end,:)-M(:,end-1,:);
  fx = cat(3,fx,fy);
end
%=============================================================
```

A-3 DERIVATION OF THE FIDELITY TERM

The energy functional to be minimized takes the form:

$$min \int_{\Omega} \phi(|\nabla u|)\, dxdy \tag{A.16}$$
$$\text{subject to: } \int_{\Omega} \left(\frac{1}{2}(k * u - u_0)^2 dxdy - |\Omega|\sigma^2 \right) = 0.$$

An image degradation problem can be abstractly formulated as:

$$\begin{aligned} k * u + n &= u_0 \\ \implies k * u - u_0 &= -n \\ \implies (k * u - u_0)^2 &= n^2. \end{aligned}$$

Taking expectation on both sides;

$$E(k * u - u_0)^2 = E(n - 0)^2,$$

here $E(x)$ denotes the expectation of x, then (refer Rudin et al. (1992) for explanations):

$$\frac{1}{|\Omega|} \int_{\Omega} \frac{1}{2}(k * u - u_0)^2 dxdy = \sigma^2,$$

where σ^2 is the noise variance; the noise is assumed to have zero mean and $|\Omega|$ is the total number of pixels in Ω, therefore,

$$\int_{\Omega} (k * u - u_0)^2 dxdy = |\Omega|\sigma^2 \tag{A.17}$$
$$\implies \int_{\Omega} (k * u - u_0)^2 dxdy - |\Omega|\sigma^2 = 0.$$

Here $\int_{\Omega}(k*u-u_0)^2 dxdy$ is the $\mathcal{L}^2$-norm of the functional $(k*u-u_0)^2$. This is generally written as: $\|k * u - u_0\|^2_{\mathcal{L}^2}$. Since $|\Omega|\sigma^2$ is a constant we can neglect this term while taking the Euler-Lagrange (EL) equation of (A.16). Therefore, using (A.12) one can easily derive the EL equation for (A.16) as:

$$div \left(\frac{\phi'(|\nabla u|)}{|\nabla u|} \nabla u \right) - \lambda k * (k * u - u_0) = 0. \tag{A.18}$$

Minimization in Fourier domain

We recall the degradation problem:

$$u_0 = k * u + n, \tag{A.19}$$

here $*$ is a convolution operation and k is kernel[2].

FFT regularization

The classical minimization problem can be modeled as:

$$\begin{aligned} &\min_u \int_\Omega \|u\|^2 dxdy \\ &\text{subject to } \int_\Omega (u_0 - k * u)^2 dxdy = 0. \end{aligned} \tag{A.20}$$

Taking the minimization problem in Fourier domain yields:

$$\begin{aligned} &\min_{\hat{u}} \int_\Omega \|\hat{u(\omega)}\|^2 d\omega \\ &\text{subject to } \int_\Omega (\hat{u_0(\omega)} - \hat{k(\omega)} * \hat{u(\omega)})^2 d\omega = 0, \end{aligned} \tag{A.21}$$

where $\hat{x}$ represents the Fourier domain representation of x. The unconstrained minimization problem can be formulated as:

$$\lambda \int_\Omega \|\hat{u(\omega)}\|^2 d\omega + \int_\Omega (\hat{u_0(\omega)} - \hat{k(\omega)}\hat{u(\omega)})^2 d\omega = J(u), \tag{A.22}$$

where λ is a scalar regularization parameter as described previously. The E-L equation at steady state can be derived as:

$$\hat{u(\omega)}\lambda + (-\hat{u_0(\omega)} + \hat{k(\omega)}\hat{u(\omega)})\hat{k(\omega)} = 0 \tag{A.23}$$

therefore,

$$\hat{u(\omega)} = \frac{\hat{u_0(\omega)}\hat{k(\omega)}}{\|\hat{k(\omega)}\|^2 + \lambda}. \tag{A.24}$$

[2]The shift invariance is assumed.

Sobolev regularization

The functional to be minimized can be written as:

$$\min_u \int_\Omega \|\nabla u\|^2 dxdy \quad \text{subject to} \int_\Omega (u_0 - k * u)^2 dxdy = 0. \tag{A.25}$$

Taking the Fourier transform of $\|\nabla u\|^2$ yields (Gonzalez and Woods 2001):

$$\|\omega\|^2 \|\hat{u}(\omega)\|^2. \tag{A.26}$$

Therefore, the unconstrained minimization problem in Fourier domain can be denoted as:

$$J(u) = \lambda\|\omega\|^2 \int_\Omega \|\hat{u(\omega)}\|^2 d\omega + \int_\Omega (\hat{u_0(\omega)} - \hat{k(\omega)}\hat{u(\omega)})^2 d\omega. \tag{A.27}$$

The E-L equation can be written as:

$$\hat{u(\omega)}\lambda\|\omega\|^2 + (-\hat{u_0(\omega)} + \hat{k(\omega)}\hat{u(\omega)})\hat{k(\omega)} = 0. \tag{A.28}$$

Rearranging the terms in above equation results in:

$$\hat{u(\omega)} = \frac{\hat{u_0(\omega)}\hat{k(\omega)}}{\|\hat{k(\omega)}\|^2 + \lambda\|\omega\|^2}. \tag{A.29}$$

Taking $\|\omega\|^2 = S(\omega)$ we can modify the above expression as:

$$\hat{u(\omega)} = \frac{\hat{u_0(\omega)}\hat{k(\omega)}}{\|\hat{k(\omega)}\|^2 + \lambda S(\omega)}. \tag{A.30}$$

Weiner /Least mean square error filter

The Fourier representation of the degradation problem in (1.1) can be written as:

$$\hat{u_0} = \hat{k}\hat{u} + \hat{n}, \tag{A.31}$$

taking $1/\hat{k} = \hat{w}$, we can write:

$$|\hat{u} - \hat{u_0}|^2 = |\hat{u}(1 - \hat{w}\hat{k}) - \hat{w}\hat{n}|^2. \tag{A.32}$$

The least square error minimization problem can be stated as:

$$\int_{\Omega} E_r dxdy = \int_{\Omega} \min |\hat{u} - \hat{u_0}|^2 dxdy, \tag{A.33}$$

where E_r is the squared error. Therefore (A.32) can be stated as:

$$\int_{\Omega} |\hat{u} - \hat{u_0}|^2 dxdy = \int_{\Omega} |\hat{u}(1 - \hat{w}\hat{k}) - \hat{w}\hat{n}|^2 dxdy. \tag{A.34}$$

Now the sufficient condition for w to be the minimizer of E_r is $\partial E_r / \partial w = 0$. The least square estimate of (A.34) (taking the derivative with respect to w and rearranging the terms) yields:

$$\hat{w} = \frac{\hat{k}^* |\hat{u}|^2}{|\hat{u}|^2 |\hat{k}|^2 + |\hat{n}|^2}. \tag{A.35}$$

Taking $S_{uu} = |\hat{u}|^2$, $S_{nn} = |\hat{n}|^2$, $K^* = \hat{k}^*$ and $\hat{w} = W$, the above equation can be written as:

$$W(\omega) = \frac{K(\omega)^* S_{uu}}{|K(\omega)|^2 S_{uu} + S_{nn}}. \tag{A.36}$$

A-4 CONVEXITY OF FUNCTIONALS

Convexity for the functionals

Here we try to prove the convexity of the functional used in this thesis:

Perona-Malik Functional

The energy functional can be stated as:

$$\phi(|\nabla u|) = \int_{\Omega} \frac{\kappa^2}{2} ln(k^2 + \|\nabla u\|^2) dxdy, \tag{A.37}$$

Theorem 3. *The functional in* (A.37) *is convex if* $|\nabla u| \leq \kappa$.

Proof. To prove the convexity of the functional it is sufficient to prove that the second order derivative of the functional is positive. One can easily note that:

$$\phi'(|\nabla u|) = \frac{|\nabla u|}{1 + \frac{|\nabla u|}{\kappa^2}} \tag{A.38}$$

and

$$\phi''(|\nabla u|) = \frac{1 - \frac{|\nabla u|^2}{\kappa^2}}{\left(1 + \frac{|\nabla u|^2}{\kappa^2}\right)^2}. \tag{A.39}$$

For convexity $\phi''(.) \geq 0$, for this condition to be valid (since denominator of the expression is already positive):

$$\begin{aligned} 1 - \frac{|\nabla u|^2}{\kappa^2} &\geq 0 \\ \implies \frac{|\nabla u|^2}{\kappa^2} &\leq 1 \\ \implies |\nabla u| &\leq \kappa. \end{aligned}$$

Hence the proof. □

TV-functional

The energy functional used in TV minimization problem in Rudin et al. (1992) is:

$$\phi(|\nabla u|) = |\nabla u|. \tag{A.40}$$

This functional is convex (not in the strict sense) since $\phi''(|\nabla u|) \geq 0$. Recall that the sufficient condition for any function $f(x)$ to be convex is its second derivative should be greater than or equal to zero. However, the derivative does not exist at places where $|\nabla u| = 0$, because

$$\lim_{x \to 0^+} ((\phi(|\nabla u|) - \phi(0))/|\nabla u|) = 1 \neq \lim_{x \to 0^-} ((\phi(|\nabla u|) - \phi(0))/|\nabla u|) = -1. \quad \text{(A.41)}$$

Therefore, it is always a good practice to perturb the absolute gradient ∇u with a small positive constant β.

Tikhonov functional

The functional used in Tikhonov regularization (Tikhonov and Arsenin 1977) is:

$$\phi(|\nabla u|) = |\nabla u|^2. \quad \text{(A.42)}$$

This functional is strictly convex since $\phi''(|\nabla u|) = 2 > 0$ and the derivative exists at all the points.

In general for any functional $\phi(|\nabla u|) = |\nabla u|^p$ when $p > 1$, the functional will be convex and derivative exists at all the points. This functional is in general called the *p-Laplacian* functional.

Fourth-order equations

The energy functional associated with the fourth-order PDE considered in You and Kaveh (2000) is:

$$E(u) = \int_\Omega \phi(\|\nabla^2 u\|) dx dy, \quad \text{(A.43)}$$

where

$$\phi(\|\nabla^2 u\|) = \|\nabla^2 u\|. \quad \text{(A.44)}$$

Theorem 4. *The above functional $E(u)$ is convex when $\phi(.)$ is an increasing function (extracted from You and Kaveh (2000) and provided for completeness).*

Proof. Let u_1 and u_2 be two images, then using Minkowski's inequality (Naylor and Sell 1982) we can write:

$$|\nabla^2[\lambda u_1 + (1-\lambda)u_2] \leq \lambda|\nabla^2 u_1| + (1-\lambda)|\nabla^2 u_2|. \tag{A.45}$$

Since we have assumed the strictly increasing nature of $\phi(.)$ we can write:

$$f(|\nabla^2[\lambda u_1 + (1-\lambda)u_2]) \leq f(\lambda|\nabla^2 u_1| + (1-\lambda)|\nabla^2 u_2|). \tag{A.46}$$

From the convexity of $f(.)$ one can derive:

$$f(\lambda|\nabla^2 u_1| + (1-\lambda)|\nabla^2 u_2|) \leq \lambda f(|\nabla^2 u_1|) + (1-\lambda)f(|\nabla^2 u_2|). \tag{A.47}$$

By combining A.47 and A.47 one can write:

$$f(|\nabla^2[\lambda u_1 + (1-\lambda)u_2]) \leq \lambda f(|\nabla^2 u_1|) + (1-\lambda)f(|\nabla^2 u_2|). \tag{A.48}$$

Integrating A.48 over the image domain will give:

$$\int_\Omega f(|\nabla^2[\lambda u_1 + (1-\lambda)u_2])dxdy \leq \lambda \int_\Omega f(|\nabla^2 u_1|) + (1-\lambda)\int_\Omega f(|\nabla^2 u_2|)dxdy, \tag{A.49}$$

which is :

$$E(\lambda u_1 + (1-\lambda)u_2) \leq \lambda E(u_1) + (1-\lambda)E(u_2). \tag{A.50}$$

Therefore, $E(u)$ is convex and hence the proof. □

A-5 Differential schemes

The differential scheme used for the diffusion term of the TV filter is discribed below, the differenctial schemes for other filters are also derived in the same manner. The TV filter is defined as:

$$u_t = \nabla . \frac{\nabla u}{|\nabla u|}, \tag{A.51}$$

where ∇ denotes the gradient operator and . denotes the inner product. The differential for of above equation is (here we are deriving the RHS of the above equation):

$$\left[\frac{\partial}{\partial x}\frac{\partial}{\partial y}\right] . \left[\frac{u_x}{(u_x^2+u_y^2)^{(1/2)}} \; \frac{u_y}{(u_x^2+u_y^2)^{(1/2)}}\right]^T, \tag{A.52}$$

where u_x and u_y corresponds to the derivatives in x and y directions, respectively and $[.]^T$ denotes the transpose of the vector field. The above equation can be writte as:

$$\frac{\partial}{\partial x}\frac{u_x}{(u_x^2+u_y^2)^{(1/2)}} + \frac{\partial}{\partial y}\frac{u_y}{(u_x^2+u_y^2)^{(1/2)}}. \tag{A.53}$$

Now we denote the numerator of the expression as Num and denominator as Den. Now performing the differentiation and further simplification of the above equation yields:

$$Num = \frac{1}{(u_x^2+u_y^2)^{(1/2)}}\left[u_y^2 u_{xx} - 2u_x u_y u_{xy} + u_x^2 u_{yy}\right], \tag{A.54}$$

$$Den = (u_x^2 + u_y^2), \tag{A.55}$$

Therefore, the TV model (curvature of the level curve) can be written using the differential scheme as (Num/Den):

$$\frac{u_y^2 u_{xx} - 2u_x u_y u_{xy} + u_x^2 u_{yy}}{(u_x^2+u_y^2)^{(3/2)}} \tag{A.56}$$

Similaly the mean curvature $\left(|\nabla u|\nabla . \frac{\nabla u}{|\nabla u|}\right)$ can be written in differetial form as:

$$\frac{u_y^2 u_{xx} - 2u_x u_y u_{xy} + u_x^2 u_{yy}}{(u_x^2+u_y^2)}. \tag{A.57}$$

Bibliography

Adams, R.A. and Fournier, J.F. (2003). *Sobolev Spaces*, Academic Press, New York.

Alvarez, L., Lions, P.L. and Morel, J.M. (1992). "Image selective smoothing and edge detection by nonlinear diffusion II." *SIAM Journal of numerical analysis*, 29 (3), 845–866.

Alvarez, L. and Mazorra, L. (1994). "Signal and image restoration using shock filters and anisotropic diffusion." *SIAM Journal of numerical analysis*, 31 (2), 590–605.

Ambrosio, L., Fusco, N. and Pallara, D. (2000). *Functions of bounded variation and free discontinuity problems*, Oxford Mathematical Monographs, Oxford University Press, New York.

Aubert, G. and Kornprobst, P. (2006). *Mathematical problems in image processing: partial differential equitations and calculus of variations*, Springer, New York.

Aubert, G. and Vese, L. (1997). "A variational method in image recovery." *SIAM Journal of numerical analysis*, 34(5), 1948–1979.

Bertalmio, M., Bertozzi, A. L. and Sapiro, G. (2001). "Navier-stokes, fluid dynamics, and image and video inpainting." *In: Proceedings of IEEE Computer Vision and Pattern Recognition (CVPR)*,Houston, TX., USA, 436–449.

Bertalmio, M., Caselles, V., Rouge, B. and Sole, A. (2003). "TV based image restoration withlocal constraints." *Journal of scientific computing*, 19(1), 95–122.

Bertero, M. and Boccacci, P. (1998). *Introduction to inverse problems in Imaging*, IoP publications, London.

Blomgren, P., Chan, T.F. and Mulet, P. (1997). "Extension to total variation denoising." *In: Proceedings of SPIE97*, San Diego, USA, 1964–1977.

Brockett, R. and Maragos, P. (1992). "Evolution equations for continuous scale morphology." *In: Proceedings of IEEE International conference on Acoustic, speech and signal processing*, Cambridge, MA, USA, 125–128.

Buades, A., Coll, B. and Morel, J.M. (2005). "A review of image denoising algorithm with a new one." *SIAM Journal on applied mathematics*, 4(2), 490–530.

Canny, J. (1986). "A computational approach to edge detection." *IEEE Transaction on pattern analysis and machine intelligence*, 8(6), 679–698.

Carmona, R. A. and Zhong, S. (1998). "Adaptive smoothing respecting feature directions." *IEEE Transactions on image processing*, 3(7), 353–358.

Caselles, V., Bertalmio, M., Sapiro, G. and Ballester, C. (2000). "Image inpainting." *In: Proceedings of 27th international conference computer graphics and interactive techniques (SIGGRAPH-2000)*, New Orleans, LA, USA, 759–762.

Catte, F., Lions, P.L., Morel, J.M. and Coll, T. (1992). "Image selective smoothing and edge detection by nonlinear diffusion." *SIAM Journal of numerical analysis*, 29(1), 182–193.

Chan, T.F. and Chiu-Kwong Wong (1998). "Total variation blind deconvolution." *IEEE Transactions on Image Processing*, 3(7), 370–375.

Chan, T.F, Golub, G. H. and Mulet, P. (1999). "A non-linear primal-dual method for total variation-bases image restoration." *SIAM Journal on scientific computing*, 20(6), 1964–1977.

Chan, T.F., Kang, S. and Shen, J. (2002). "Eulers elastica and curvature-based image inpainting." *SIAM Journal on applied mathematics*, 63(7), 564–592.

Chan, T.F and Mullet, P. (1996). "On convergence of the lagged diffusivity fixed points in image restoration." *SIAM Journal on scientific computing*, 17(2), 227–238.

Chan, T.F., Osher, S. and Shen, J. (2001). "The digital tv filter and nonlinear denoising." *IEEE Transactions on image processing*, 10(2), 231–241.

Chan, T.F., Selim, E. and Frederick, P. (2010). "A fourth-order dual method for stair-case reduction in texture extraction and image restoration problems." *In: Proceedings of 2010 IEEE 17th International Conference on Image Processing*, Braunschweig, Germany, 4137–4140.

Chan, T.F. and Shen, J. (2001). "Mathematical models of local non-texture inpaintings." *SIAM Journal on applied mathematics*, 62(3), 1019–1043.

Chan, T.F. and Shen, J. (2001a). "Non-texture inpainting by curvature driven diffusions (cdd)." *Journal of visual communication and image representation*, 12(4), 436–449.

Chan T.F. and Shen, J. (2001b). "Local inpainting models and tv inpainting." *SIAM Journal of applied mathematics*, 62(3), 1019–1043.

Chan, T.F. and Shen, J. (2005). *Image processing and analysis, variational, PDE, wavelet and stochastic methods*, SIAM, Philadelphia.

Coulon, O. and Arridge, S. (2000). "Dual echo mr image processing using multispectral probabilistic diffusion coupled with shock filters." *In: Proceedings of British conference on medical image understanding and analysis*, London, UK, 458–461. Contrast-to-noise ratio (CNR) as a quality parameter in fMRI. . 2007 Jun;25(6):1263-70.

Geissler, A., Gartus, A., Foki, T., Tahamtan, AR., Beisteiner, R. and Barth, M. (2007). "Contrast-to-noise ratio (CNR) as a quality parameter in fMRI" *J. Magn. Reson. Imaging*, 25(6), 1263–1270.

Gelfand, I. M and Fomin, S. V. (1963). *Calculus of variations*, Prentice-Hall, New Jersey.

Giaquinta, M. and Hildebrandt, S. (1996). *Calculus of variations I-The Lagrangian formalism*, Springer, Berlin.

Gilboa, G., Sochen, N. A. and Zeevi, Y. V. (2002). "Regularized shock filters and complex diffusion." *In: Proceedings of the 7th European conference on computer vision*, London, UK, 399–413.

Gilboa, G., Sochen, N. A. and Zeevi, Y. V. (2008). "Image denoising and decomposition with total variation minimization and oscillatory functions." *Journal of mathematical imaging and vision*, 20(8), 7–18.

Gonzalez, R. C. and Woods, R. E. (2001). *Digital image processing*, Prentice Hall, New York.

Hadamard, J. (1953). *Lectures on cauchy's problem in linear partial differential equations*, Dover publication, New york.

Hajiaboli, M. R. (2009). "A self-governing hybrid model for noise removal." *In: Proceedings of the 3rd Pacific Rim symposium on advances in image and video technology*, Berlin, Germany, 295–305.

Hajiaboli, M. R. (2010). "An anisotropic fourth-order diffusion filter for image noise removal." *International journal of computer vision*, 20(1), 182–197.

Hansen, P.C, Nagy, J.G, and O'Leary, D.P (1991). *Deblurring images matrices, spectra and filtering*, SIAM publishing, Philadelphia.

Hillery, A. D. and Chin, R. T. (1991). "Iterative Weiner filter for image enhancement." *IEEE Transactions on signal processing*, 39 (8), 1892–1899.

Hollig, K. (1983). "Existence of infinitely many solutions for forward-backward heat equation." *Transactions of American mathematical society*, 278(2), 299–316.

Iijima, T. (1962). "Basic theory on normalization of pattern (in case of typical one-dimensional pattern." *Bulletin of the Electrotechnical Laboratory*, 26(1), 368–388 (In Japanese).

Joshi, N., Lawrence, C., Zitnick, R., Szeliski, D. and Kriegman, J. (2009). "Image deblurring and denoising using color priors." *In: Proceedings of IEEE Conference on computer vision and pattern recognition*, Redmond, USA, 1510–1557.

Kornprobst, P., Deriche, R. and Aubert, G. (1997). "Image coupling, restoration and enhancement via PDEs." *In: Proceedings of the 4th International conference on image processing*, Santa Barbara, CA, USA, 458–461.

Lee, J.S. (1980). "Digital image enhancement and noise filtering by use of local statistics." *IEEE Transaction on pattern analysis and machine intelligence*, 2(2), 165–168.

Lee, S H. and Seo, J K. (2005). "Noise removal with gauss curvature-driven diffusion." *IEEE Transactions on Image Processing*, 14(7), 904–909.

Lysaker, M., Lundervold, A. and Tai, X. C. (2003). "Noise removal using fourth-order partial differential equation with applications to medical magnetic resonance images in space and time." *IEEE Transactions on image processing*, 12(12), 1579–1589.

Malladi, R., Sethian, J. A. (1996). "Image processing: Flows under min/max curvature and mean curvature." *Graphical Models and Image Processing*, 58(2), 127–141.

Malladi, R., Sethian, J. A. and Vemuri, B. C. (1995). "Shape modeling with front propagation: A level set approach." *IEEE Transaction on pattern analysis and machine intelligence*, 17(2), 158–175.

Marquiana, A. and Osher, S. (2000). "Explicit algorithms for a new time-dependent model based on level set motion for non linear deblurring and noise removal." *SIAM Journal on scientific computing*, 22(2), 387–405.

Masnou, S. and Morel, J.M. (1998). "Level-lines based disocclusion." *In: Proceedings of 5th IEEE Intl Conference on image processing*, Chicago, IL, USA, 759–762.

Naylor, A. W. and Sell, G. R. (1982). 'Linear operator theory in engineering and science." *Springer-Verlag*, Germany.

Osher, S. and Rudin, L. I. (1990). "Feature-oriented image enhancement using shock filters." *SIAM Journal of numerical analysis*, 27(4), 919–940.

Osher, S. and Sethian, J. A. (1988). "Fronts propagating with curvature-dependent speed: Algorithms based on Hamilton-Jacobi formulation." *Journal of computational physics*, 79(1), 12–49.

Perona, P. and Malik, J. (1990). "Scale-space and edge detection using anisotropic diffusion." *IEEE Transactions on pattern analysis and machine intelligence*, 12(7), 629–639.

Peter, V.B., Yang, J., Yamamoto, S. and Ueda, Y. (2010). "Image deblurring and denoising with non-local regularization constraint." *In: Proceedings of international conference on visual information processing and communication*, San Jose, California, 1–11.

Pratt, W. K. (1977). *Digital Image Processing*, Wiley, New York.

Romeny, H. and Bart, M. (1994). *Geometry driven diffusion in computer vision*, Kluver Acadamic Publisher, USA.

Rudin, L. I., Osher, S. and Fatemi, E. (1992). "Nonlinear total variation based noise removal algorithms." *Physica D.*, 60(1), 259–268.

Russ, J.C. (2007). *The image processing handbook*, CRC Press, Fin Land.

Shen, J. (2003). "Inpainting and the fundamental problem of image processing." *SIAM News*, 36(5), 1–4.

Song, B. (2003). "Topics in Variational PDE Image Segmentation, Inpainting and Denoising", Ph.D. Thesis, University of California,LA.

Thomas, J. W. (1995). *Numerical partial differential equations: Finite difference methods*, Springer-Verlag, Germany.

Tikhonov, A. and Arsenin, V. (1977). *Solution of ill-posed problems*, Wiston and Sons, London.

Vincente, V., Candella, F., Marquina, A. and Susana, S. (2003). "A local spectral inversion of a linearized tv model for denoising and deblurring." *IEEE Transactions on image processing*, 12(7), 808–816.

Vogel, C. and Oman, M. (1996). "Iterative methods for total variation denoising." *SIAM Journal on scientific and statistical computing*, 17(4), 227–238.

Wang, Z. and Bovik, A. C. (2004). "Image quality assessment: From error visibility to structural similarity." *IEEE Transactions on image processing*, 13(4), 1–14.

Wei, S. and Xu, H. (2009). "Staircasing reduction model applied to total variation based image reconstruction." *In: Proceedings of 17th European signal processing conference (EUSIPCO 2009)*, Glasgow, Scotland, 2579–2583.

Weickert, J. (1997). "A review of nonlinear diffusion filtering." *Scale-Space*, 3–28.

Weickert, J. (1999). "Coherence-enhancing diffusion filtering." *International Journal of Computer Vision*, 31(3), 111–127.

Wiener Norbert (1949). *Extrapolation, interpolation and smoothing of stationary time series*, Wiley, New York.

Witkin, A.P. (1983). "Scale-space filtering." *In: Proceedings of eighth international joint conference on artificial intelligence*, San Francisco, CA, 1019–1022.

You, Y.L. and Kaveh, M. (2000). "Fourth-order partial differential equations for noise removal." *IEEE Transactions on Image Processing*, 9(10), 1723–1730.

Yuan, L. Sun, J., Quan, L. and Shum H-Y. (2007). "Image deblurring with blurred/noisy image pairs." *In: Proceedings of ACM SIGGRAPH Conference*, New York, USA, 1–10.

Publications based on the thesis

Refereed International Journals

1. P. Jidesh and Santhosh George (2012), "Shock Coupled Fourth-order Diffusion for Image Enhancement", *Computers & Electrical Engineering an International Journal*, Vol. 38, No. 5, pp. 1262-1277.
   (Elsevier)

2. P. Jidesh and Santhosh George (2012), "A time-dependent switching anisotropic diffusion model for denoising and deblurring images", *Journal of Modern Optics*, Vol. 59, No.2, pp. 140-156.
   (Taylor & Francis)

3. P. Jidesh and George S. ,"Gauss Curvature Driven Image Inpainting for Image reconstruction", *Journal of Chinese Institute of Engineers (JCIE)*, Scheduled to appear in Vol 37 (2014).
   (Taylor & Francis)

4. P. Jidesh and Santhosh George (2011), "Curvature Driven Diffusion Coupled with Shock for Image Enhancement/Reconstruction", *International Journal of Signal and Imaging Systems Engineering*, Vol. 4, No. 4, pp. 238-247. *(Inderscience)*

Bio-data

Name	: Jidesh P.
Address	: Assistant Professor,
	Department of Mathematical and Computational Sciences,
	National Institute of Technology, Karnataka, Surathkal,
	Srinivasanagar PO, Mangalore, India-575025.
	Ph:(Office) 0824-2474000 (Extn: 3253).
Email	: jidesh@nitk.ac.in, ppjidesh@gmail.com.

Qualifications	1. M.Tech (Computer Science). (2003-2005)
	2. MCA (REC/NIT Calicut). (1998-2001)
	3. B.Sc. (Maths & Physics). (1995-1998)
Work experience:	1. Assistant Professor, (2009- Till Date)
	Department of Mathematical and Computational Sciences,
	National Institute of Technology, Karnataka, India
	2. Expert (Sr. Developer) (2007-2009)
	AMDOCS-DVCI, Pune, India
	3. Systems Engineer (2005-2007),
	Tata Consultancy Services, Chennai, India.
Publications	International Journals :10 (7 SCI indexed)
	International Conferences : 6